UNIVERSITY OF CALIFORNIA,
IRVINE

Nanobubble Generation with an Alternating Magnetic Field and Interaction with Nanoparticles

DISSERTATION

submitted in partial satisfaction of the requirements
for the degree of

DOCTOR OF PHILOSOPHY

in Materials Science and Engineering

by

Ao Li

Dissertation Committee:
Professor James C. Earthman, Chair
Professor Lorenzo Valdevit
Professor Ruqian Wu

2022

DEDICATION

To

My dear family,

for their endless support and encouragement.

In memory of

Baikai Fu,
(1937-2021)

my dear grandfather.

"You build on failure. You use it as a stepping stone." - Johnny Cash

TABLE OF CONTENTS

LIST OF FIGURES

LIST OF TABLES

ACKNOWLEDGMENTS

I want to convey my heartfelt appreciation and gratitude to my adviser Professor James Calvin Earthman, who provided me the chance to start the journey and guided me all the way through it. I would like to thank him for encouraging my research and letting me grow.

I wish to thank the four committee members from my Ph.D candidate qualifying exam: Prof. Lorenzo Valdevit, Prof. Ruqian Wu, Prof. Allon Hochbaum and Prof. Diran Apelian for their assistance in developing my dissertation work.

I want to acknowledge the contribution from William Dang, Nhi Quach and Michael Schutt for their preliminary research, and Prof. Zhongping Chen and Dr. Yan Li for providing the technical support with IVOCT to allow the followup study towards this research. I want to thank Prof. Diego Rosso with his help in building the water test system for my research and Prof. Joe Patterson with his insights of TEM. I would also like to thank the undergraduate students from Earthman Lab who helped with this project, especially Keith Tran. I want to thank the faculties and staffs in the UCI Materials Science and Engineering Department and machine shop in the school of Engineering. And I would like to thank Medtronic for the funding and the donors for the human tissue samples.

I would like to thank my peer graduate student researchers: Anne Sun, Xin Fu, Huaixun Huyan, Yingjie Yang, Anthony Tsai, Xinyi Wang, Jie Shen and Vivek Tyagi. And I would like to thank my dearest friends who supported me along the way: Cissy Chen, Junjue Li, Fengyuan Jia, Jayo Zhang, Kyle Bao, Rocky Xi, Yuanzhong Pan and Zoey Wang. I am grateful to have their support and encouragements.

Lastly, I appreciate and acknowledge my loving parents for their everlasting support. Without your love, I can never walk this far, from a small town boy to a materials scientist.

VITA

Ao Li

EDUCATION

Doctor of Philosophy in Materials Science and Engineering **2022**
Univeristy of California, Irvine *Irvine, CA, US*

Master of Science in Materials Science **2017**
Univeristy of Southern California *Los Angeles, CA, US*

Bachelor of Engineering in Polymer Materials and Engineering **2015**
East China Univeristy of Science and Technology *Shanghai, China*

RESEARCH EXPERIENCE

Graduate Research Assistant **2017–2022**
University of California, Irvine *Irvine, California*

TEACHING EXPERIENCE

Teaching Assistant **2018–2022**
University of California, Irvine *Irvine, California*

REFEREED JOURNAL PUBLICATION

Li, Ao, Yan Li, Saijun Qiu, Pranav Patel, Zhongping Chen and James C. Earthman. "Dissolution Effect of Nanobubbles in Ringer's Solution on Calcified Plaque in Ex Vivo Pericardial Tissue." **2022**
Colloids and Surfaces B: Biointerfaces (Submitted)

Quach, Nhi Vu-Y., Ao Li, and James C. Earthman. "Interaction of calcium carbonate with nanobubbles produced in an alternating magnetic field." **2020**
ACS Applied Materials & Interfaces 12.39 (2020): 43714-43719

REFEREED PREPRINT

Xu, Jiang, Xiao Lei, Ao Li, Jun Li, Shuxing Li, and Lin Chen. "Scalable production of recombinant three-finger proteins: from inclusion bodies to high quality molecular probes." **2022**
bioRxiv

REFEREED CONFERENCE PRESENTATIONS

Binding Interaction Study Between Nanobubbles and Nanoparticles **2022**
TMS 22. Anaheim, CA

Dissolution of Atherosclerosis Plaque in Human Coronary Artery Induced by Nanobubble **2021**
MS&T 21. Remote

SOFTWARE

Microsoft Office, ImageJ, MATLAB, AutoCAD, and Simpleware ScanIP.

ABSTRACT OF THE DISSERTATION

Nanobubble Generation with an Alternating Magnetic Field and Interaction with Nanoparticles

By

Ao Li

Doctor of Philosophy in Materials Science and Engineering

University of California, Irvine, 2022

Professor James C. Earthman, Chair

Nanobubbles (NBs) have been studied for more than 20 years. One of the two types of NB, the bulk NB, with its extraordinary physical, chemical and biological properties, drew a lot of attention among researchers. However, the fundamental mechanisms of NB generation, stability, longevity and ability to bind nanoparticles are far behind the development of its applications in the industry.

We started from studying the generation of NBs with an alternating magnetic field, and studied NB clustering effects with different kinds of nanoparticles that include $CaCO_3$ and nanoscale Polystyrene beads. Furthermore, we tested NB's effects on the *ex vivo* dissolution of human atherosclerosis plaque. More recently, the NB-nanoparticle clustering mechanism was studied based on established DLVO theories and experimental data.

The technologies employed for characterizing NBs, nanoparticles and clusters include Nanoparticle Tracking Analysis (NTA), Dynamic Light Scattering (DLS) with ζ potential measurement and Transmission Electron Microscopy (TEM). Intravascular Optical Coherence Tomography (IVOCT) and Micro Computed Tomography (Micro-CT) were used to characterize the volume of plaque in coronary/periphery arteries and aortic valve tissue, respectively.

It turns out that Bulk NBs are able to attract not only cations or nanoparticles with dipoles, but also hydrophobic nanoparticles that are nearly electroneutral considering hydrophobic attraction. It provided more insight in the interaction between nano-objects at the nanoscale. The research on the *ex vivo* dissolution of human plaque based on NB clustering also promotes the idea of developing NB treatment methods for atherosclerosis, the most lethal chronic disease.

Chapter 1

Introduction and Background

1.1 Early Research

Research project of using an alternating magnetic field (AMF) to treat service water to investigate the effect of NBs on the pitting induced by sulfate reducing bacteria in the steel pipe samples. The pipe samples have served for 30 years at a secondary cooling water system at Three Mile Island Nuclear Power Station [1].

The original samples were covered by mineral deposits and had pitting that was caused by sulfate reducing bacteria (SRB) in Fig.1.1. The mineralized nodule's mechanism of formation is illustrated in Fig.1.2. The major mineral compound, calcium carbonate, held the substances in the nodule together and increased its adhesion to the inside wall. To remove the existing nodules and prohibit the formation of new nodules, the key is to develop a technology that can promote the dissolution of the mineral deposit (mineralized nodule) in the water system.

Figure 1.1: Photograph of a sectioned mild steel pipe that failed in service at Three Mile Island Nuclear Power Station.

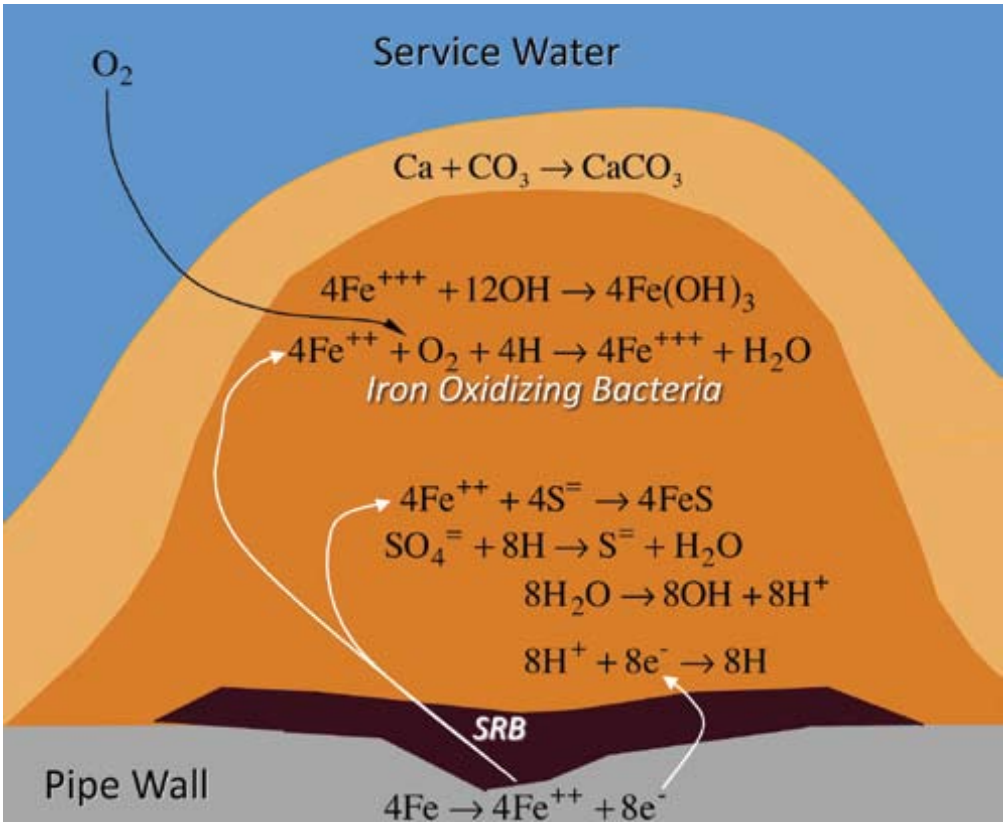

Figure 1.2: Mineralized nodule form by iron oxidizing bacteria provisioning a protective anaerobic environment for corrosion inducing SRB. [1]

Aqua-Phyd, Inc. (Newport Beach, CA) developed a water conditioning treatment that was designed to dissipate mineral compounds in the irrigation systems, to increase the efficiency of the water distribution for root absorption. The treatment was based on flowing water through an alternating magnetic field (AMF) as in Fig.1.3. Surprisingly, users of this treatment occasionally reported an unusually large amount of mineral and organic matter that appears to be from the inside wall of the irrigation line. This observation revealed the AMF-treated water may have the potential to remove mineral deposits in service water pipe.

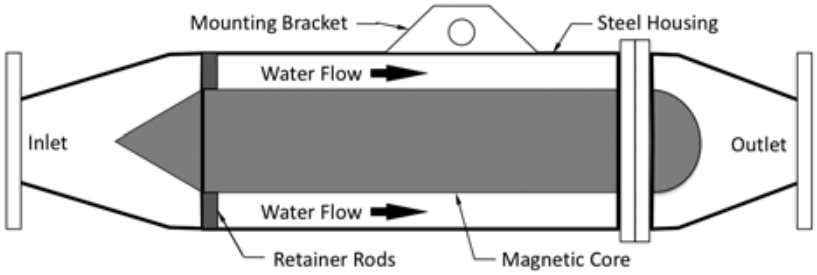

Figure 1.3: Schematic cross section of the AMF treatment system produced by Aqua-Phyd, Inc.

The two received pipe section samples were mounted in two closed-loop test systems as shown in Fig.1.4. One of these systems contained the AMF treatment and the other control system didn't but was otherwise identical. After 48 hours of cycling water in the systems, the water turned significantly cleaner in the system with the AMF treatment, as the inset photo in Fig.1.4. After eight months of testing, the pipe samples were sectioned and polished. A quantitative image analysis was performed to measure the depths of over 100 pits on the optical microscopic images on the sectioned surface for each sample. The result has been plotted as in Fig.1.5. This probability plot showed that the pit depth in the pipe sample without AMF treatment was about 50% greater than the one with AMF. As the two samples have been in service for 30 years, this pit depth difference is significant and indicated that the AMF treated water is able to dissolve or promote the dissolution of the insoluble mineral

deposit on a steel pipe.

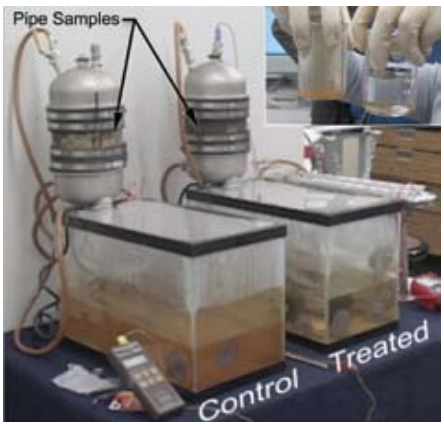

Figure 1.4: Photograph of the test systems with the mild steel pipe samples from Three Mile Island Nuclear Power Station.

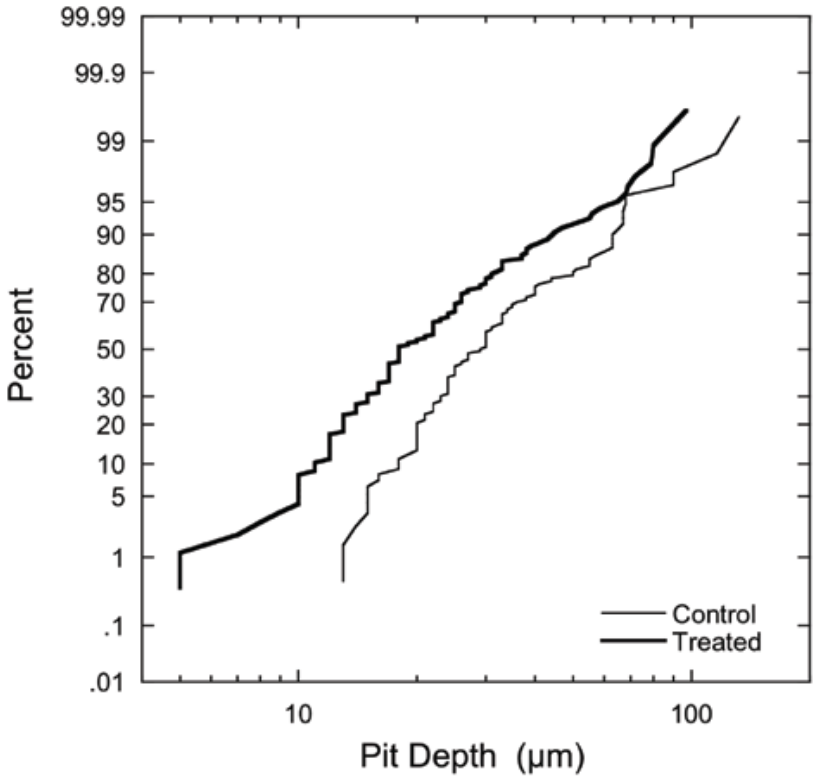

Figure 1.5: Probability plot of pit depth versus cumulative frequency for pits measured on cross sections of pipe samples tested in control and AMF treated service water.
($N_{control} = 105, N_{treated} = 132$)

1.2 The Question Remains

Even though the AMF treated service water was shown to be able to alleviate the pitting corrosion in the mild steel pipe sample (1.5), the mechanism behind was not elucidated. In fact, the effect of magnetic field on water and aqueous solution have been reported for at least half of century [2]. More specifically, researchers were trying to figure out why the magnetic field treated water can dissolve more insoluble substances than the untreated water. In 1995, Lungader Madsen claimed the reduced size of the calcium carbonate precipitates in the magnetic field treated water was due to a larger number of the formed nuclei [3]. The authors confirmed that the magnetic field had an effect on both calcium ions and bicarbonate ions, which led to the reduced size of calcium carbonate particles. The other theory claimed that the magnetic field's effect on the particle surface charge can increase the nucleation rate [4]. Or both the two mentioned mechanisms occur simultaneously. However the answer to this question is still unclear.

Interestingly, when studying the effect of magnetic field on water and aqueous solution, experimental results showed that the magnetic field enhanced the water evaporation rate [5, 6, 7]. For example, in 2012, Yun-Zhu Guo et al. compared the water evaporation in a homogeneous magnetic field with different magnetic field gradients and in the absence of the magnetic field in 24 hours [7]. The experimental results indicated that the magnetic field did enhance the water evaporation. Furthermore, the authors proposed that the Lorentz force from the gradient magnetic field may affect both the hydrogen bonding and van der Waals forces in the water, as the cause of the enhanced water evaporation by a magnetic field.

With these observations and deductions, it comes to the idea that the magnetic field may not only enhance water evaporation but also precipitate gas that was dissolved in the water, as the dissolution of gas also depends on the hydrogen bonding and van der Waals forces between gas and water molecules.

1.3 Hypothesis and Research Plan

The first research on nanobubbles (NBs) was conducted nearly 50 years after the first reported study on magnetic field's effect on water. The definition of a NB is a gas domain in aqueous solution in the nanoscale. It drew a lot of attention by its unusual stability that can last for days and weeks [8, 9]. Surprisingly, some other studies showed its ability to bind nanoparticles [10, 11, 12, 13, 14].

By relating the AMF's disruption of molecular interaction in the water and NBs binding interaction with nanoparticles, it is reasonable to hypothesize that, AMF can generate NBs in the water, and the existence of NBs promotes the dissolution of the insoluble substances, by binding suspended nanoparticles, as in fig.1.6. With the decrease in the local concentration of free nanoparticles, the dissolution of the insoluble substances is then accelerated.

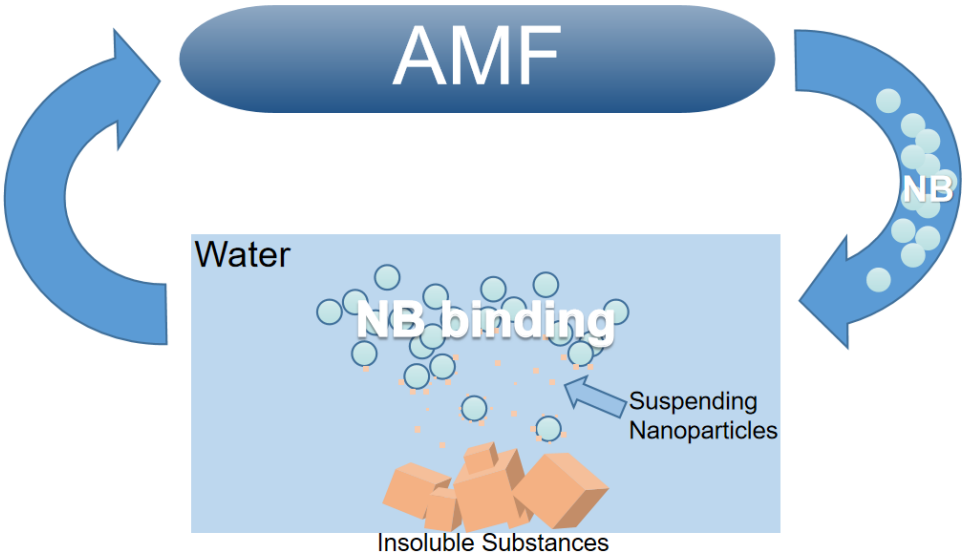

Figure 1.6: Schematic of the binding interaction between AMF generated NBs and suspending nanoparticles

In order to investigate this hypothesis, several test systems were developed and multiple characterization methods were used to test the results. In the following chapters, we first discuss previous studies about NB generation, stability and binding with nanoparticles in

Chapter 2. Following that is the study of AMF generated NBs' effect on the dissolution of $CaCO_3$, atherosclerosis plaque and aortic valve tissue plaque in Chapter 3, 4 and 5, respectively. In Chapter 6, the contribution of hydrophobic force in the NB-nanoparticle interaction was discussed to supplement the traditional DLVO theory. and in Chapter 7, further study on the AMF NB generation is discussed. Finally, we conclude this dissertation in Chapter 8 by summarizing the results and proposing the future work in Chapter 9.

Chapter 2

Literature Reviews on Nanobubble Generation, Stability and Binding with Nanoparticles

2.1 Existence of Bulk Nanobubbles

Nanobubbles (NBs) are sub-micron gas-containing cavities in aqueous solution and were first reported in 2001[15]. For a bubble, Young-Laplace equation can be written as:

$$P_{int} - P_{ext} = P_{st} = 2\gamma/R \tag{2.1}$$

P_{int} and P_{ext} are the pressure from the inside and outside of a bubble, P_{st} is the pressure caused by surface tension, also called Laplace pressure, γ is the surface tension on the gas-liquid interface, and R is the radius or curvature of the bubble. However, for a spherical nanobubble of radius R=100 nm, the surface tension of the interface γ=72 mN/m, and P_{ext}=1 atm, Eqn 2.1 gives a P_{int} at around 15 atm. The abnormally high internal pressure

must lead to a dissolution of the gas due to larger chemical potential. It contradicts the experimental observation on nanobubble's longevity and stability [16]. The following observations revealed that there are two kinds of NBs [17]: those on a surface and those in bulk liquid as in Fig.2.1. Surface NBs have longer observed longevity and were better studied to rationalize theoretically [17, 18, 19, 20, 21, 22, 23, 24]. In this dissertation, if not specified, the abbreviation of NB only refers to bulk nanobubbles.

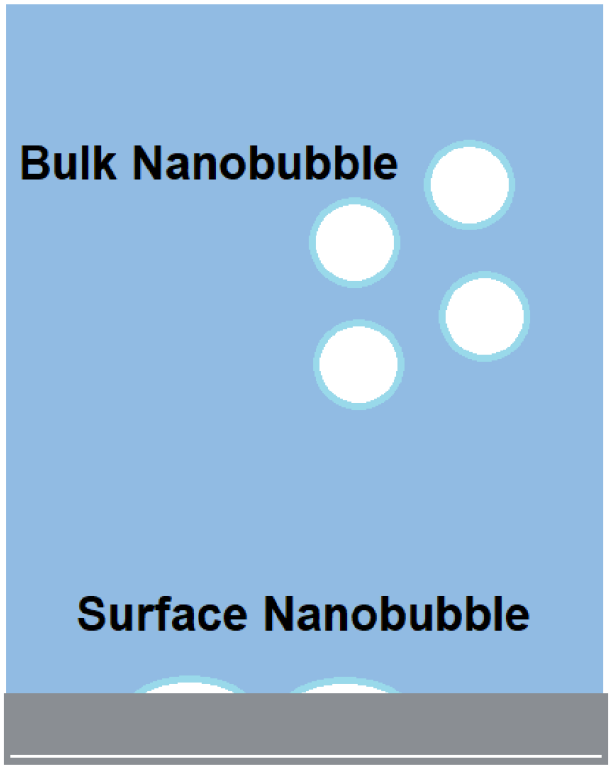

Figure 2.1: Schematic of surface NBs and bulk NBs.

Though the existence of stable surface NBs has been extensively studied [21, 25] to take the advantages of its immobility, bulk NB was still a controversial subject in the first decade when it came out. Even with the use of Dynamic Light Scattering (DLS) and Nanoparticle Tracking Analysis (NTA) that showed the existence of nano-sized objects in aqueous solution, it was still difficult to prove that they are bulk NBs rather than nanoparticles or nanodroplets [26]. Because it is inevitable that the solution has to contact other materials in a NB generation system, and turns into the first big challenge in generating bulk NBs without

contaminants, that allows the study on the fundamental mechanism of NB stabilization.

Over the years, there are more and more publications supporting the stable existence of bulk NBs. Some researchers used TEM to visualize the NBs in a freeze-fractured replica (Fig.2.2). In 2020, Jadhav, Ananda J et al. applied several experimental approaches to confirm the existence and stability of NBs [9]. First, they used cyro-SEM on a frozen solution containing NBs as shown in Fig.2.3. Moreover, they compared the bubbles' number density difference of generated NBs in the water under atmospheric pressure and partially vacuum with NTA. There was about an order of magnitude reduction in nano-sized objects under a partial vacuum, which indicates that such nano-entities must be gas-filled.

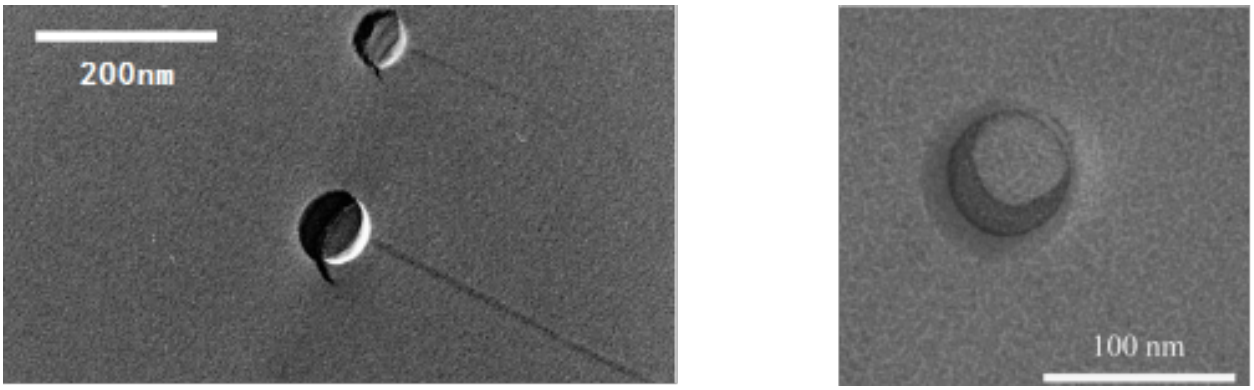

Figure 2.2: TEM image of freeze-fractured replicas of NB solution.
(left) Oxygen NBs [10] and (Right) nitrogen NBs [9] in pure water

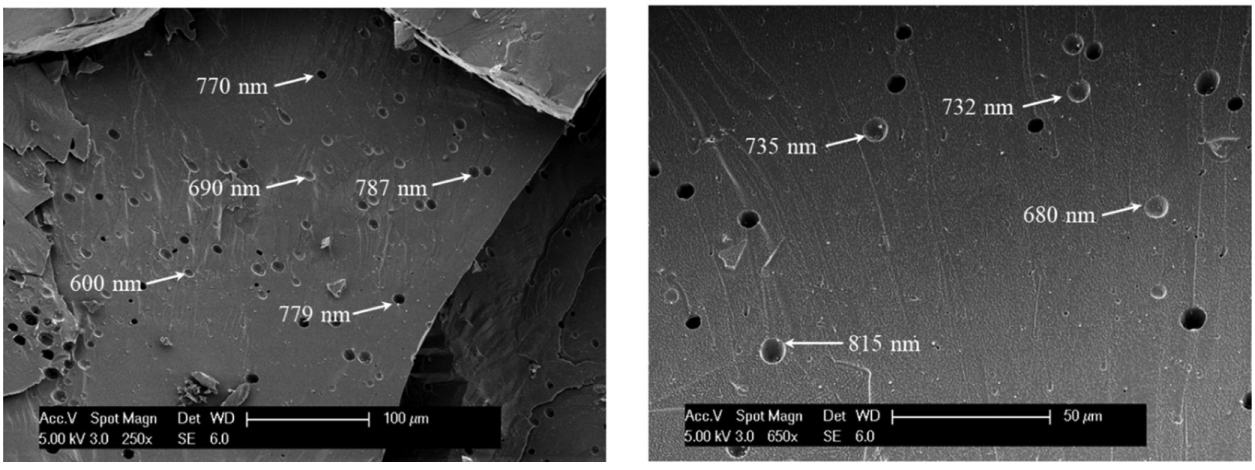

Figure 2.3: Cyro-SEM image of frozen air NBs in pure water at different magnifications.
(left) ×250 and (Right) ×650 [9]

2.2 Stability of Nanobubbles

In the theory of electrical double layer, ζ potential is the electrical potential at the slipping plane, which separates mobile fluid that remains attached to the surface, as in Fig 2.4[27]. ζ potential is always used to estimate the surface charge of nanosuspension [28]. Experimental observations revealed that NBs in water have an electrically charged liquid–gas interface, indicated by the observed high negative ζ potential [29, 30, 31].

Several publications reported hydroxide ions' affinity to the gas-liquid interface [32, 33]. In addition, The measured negative ζ potential (the electric potential on the slipping plan as in Fig. 2.4) of the NBs in nanopure water also indicated the accumulation of the hydroxide ions on the surface of a NB. It follows that, with a negatively charged interface, a NB may stabilize itself in the liquid phase by repelling other NBs.

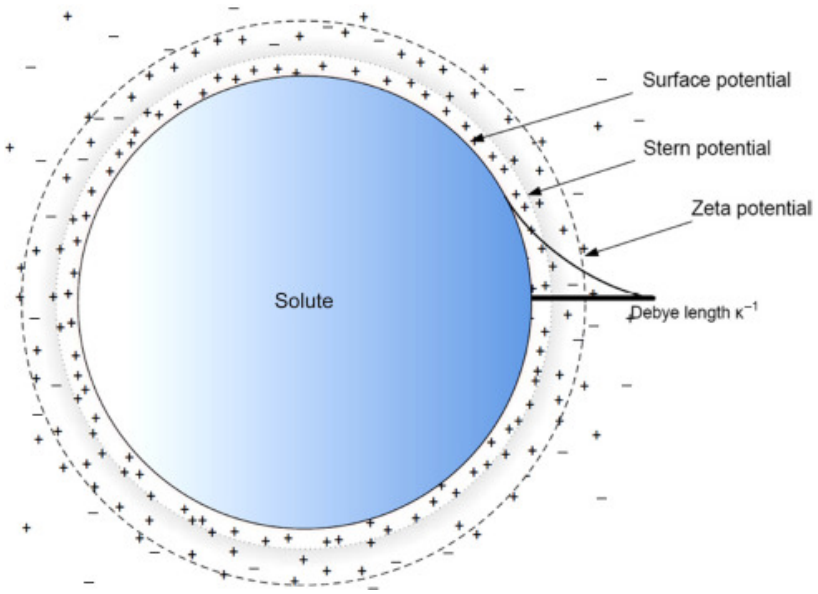

Figure 2.4: Schematic of the electrical double layer in a liquid in contact with a particle. [27]

A molecular simulation on 'ideal' bulk NBs (no matter absorption on the liquid-gas interface) also indicated that the liquid surrounding the bubble is in a highly stretched state and has large negative pressure [34]. It indicted an abnormal interface property of a NB compared

to a macroscopic bubble and a revision is needed when applying macroscopic estimation methods.

Even though the Young-Laplace equation may need some modifications when applying in the nano-scale, especially in the case of a NB, the extremely high internal pressure derived from the theory raised the question that, based on the experimental observations, why the NBs can be stable for days, even weeks?

A lot of theories and hypotheses have been made to explain the stabilization mechanism of NBs. Fundamentally, NBs can be generated either by the shrinkage of larger bubbles (macrobubbles and microbubbles) or the gas nucleation in the bulk liquid. The mechanism of the former corresponds to lowering the system's free energy to a stable or metastable state, as the NBs has extraordinary observed stability; The latter also makes sense when taking the supersaturation of gas and high flow rate's effect, as described by Bernoulli's equation, into consideration. Then a subsequent question followed: why is a NB stable from the gas dissolving back to the liquid and the coagulation between each other?

In some hypotheses, the stability of a NB is from the diffusive blocking effect on the gas-liquid interface, as a result of the accumulation of hydroxide ions. This effect was also called ionic shielding [35]. Kazunari Ohgaki et al. also reported that the rattenuated total reflectance infrared spectroscopy result showed that the a NB has hard hydrogen bonds on its surface[33]. The highly constructed hydrogen-bonding network can also block the diffusion of the gas molecules.

Furthermore, to explain the stability of NBs, the Young-Laplace equation can be modified as follows: Pratik Satpute et al. built a model for a NB stabilized by the hydroxide ions adsorbed onto its surface [36]. In this model, the electrostatic force (Coulomb repulsion) between hydroxide can compensate for the high internal pressure and the Young-Laplace

equation can be modified and rearranged as:

$$P_{int} + P_{rep} = P_{ext} + P_{st} = P_{ext} + 2\gamma/R \tag{2.2}$$

and

$$P_{rep} = \frac{\sqrt{3}k_e\sigma^2}{2} \tag{2.3}$$

Where P_{rep} is the pressure contributed from the surface ion's repulsion, k_e is the Coulombic constant for the fluid and σ is the surface charge density on the NB. However with an estimation in a water sample with neutral pH in the solution, the available hydroxide ions from water ionization are not enough to compensate the tension from the extremely curved gas-liquid interface. As a result, the authors concluded that a NB can only become stable after a microbubble shrinkage, due to the limitation from the hydroxide ion concentration in the water.

On another hand, the repulsion between NBs improved their stability by increasing the distance of Ostwald ripening or coalescence. Similar to the DLVO theory that quantitatively describes the colloidal dispersion stability, the combination of van der Waals force (attractive) and electric double layer force (repulsive) on the NBs results in a balance and prevent the coalescence. The reported concentrations of generated NB can barely go beyond 10^9 mL^{-1}, and at this maximum concentration, the distance between two NBs is as far as 10^4 nm. This distance was considered long enough to prevent Ostwald ripening or coalescence. Jay N. Meegoda, et al. studied the electrical double layer's character of NB and concluded that the low concentration of the ions increased the double layer repulsion and prevented the NB from coalescence [37]. In addition, Joost H. Weijs et al. found that NB in a cluster of bulk NBs protects each other from diffusion by a shielding effect, with a thermal dynamic simulation [38].

2.3 Nanobubble Generation Methods

NB generation methods have been intensively studied In the past decade, and most of the methods are based on hydrodynamic cavitation in the liquid phase, rather than the direct shrinkage from macroscopic bubbles. The mechanism was concluded as that the inputted external energy to the bulk liquid can lead to the cavitation/nucleation of the gas phase, then resulted in the formation of NBs. Specifically, the generation methods includes gas-liquid mixing [9, 39, 40, 41], ultrasonication [42], electrochemical method [43], temperature gradients [44], pressure changes [45] etc.

In our lab, there is a gas-liquid mixing NB generator. A Nikuni NB Generator KTM MBG20N07CE (NNBG) was kindly provided by Dr.Micheal Klopfer at UC Irvine (as Fig. 2.5). The pump was designed to compress and shear the fluid with gas, to conduct cavitation and generate microbubbles and NBs. The detailed information can be found in [46].

Figure 2.5: Schematic of the Nikuni Micro-Nano bubble generator

Unique to our lab, we have proposed the Alternating Magnetic Field (AMF) method of NB generation [47]. The AMF system as in Fig.2.6 comprises a pipe with a core mounted within the pipe, and the core extends along a length of the pipe while allowing a liquid to flow

through the pipe, wherein a plurality of magnets is housed in the core oriented north-end-to-north-end and south-end-to-south-end. The magnets expose the liquid to an alternating magnetic field up to 0.5 T. The proposed mechanism is that When water flows through the AMF unit, the magnetic field disturbs the molecular interaction between the dissolved gas and water molecules. The weakened interaction leads to the precipitation of gas out of the liquid phase, and the nucleated gas phase turns into stable NBs.

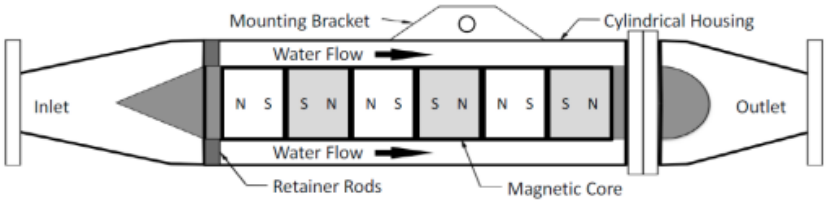

Figure 2.6: Schematic of the current AMF system

2.4 Developments in the Applications with Nanobubbles

Since the first report of the existence of NB, it has drawn more attention in developing the applications than the study in the fundamental mechanism. Because of the unestablished NB stabilization theory and limited observation technology, almost all the NB-related studies in the first decade(2001-2011), still call it Micro-Nano-bubble (MNB) or just Microbubble (MB) as in Fig.2.7. Unsurprisingly, with the advancement of the optical/electrical microscopes and a better understanding in the nano-science, NBs were intensely studied in the last decade and more insights were revealed in the fundamental mechanisms and development of related applications. The increase in the ratio of NB studies to the MB & MNB ones also indicated an improved consensus on the stable NB and its potential to be utilized to develop new technologies.

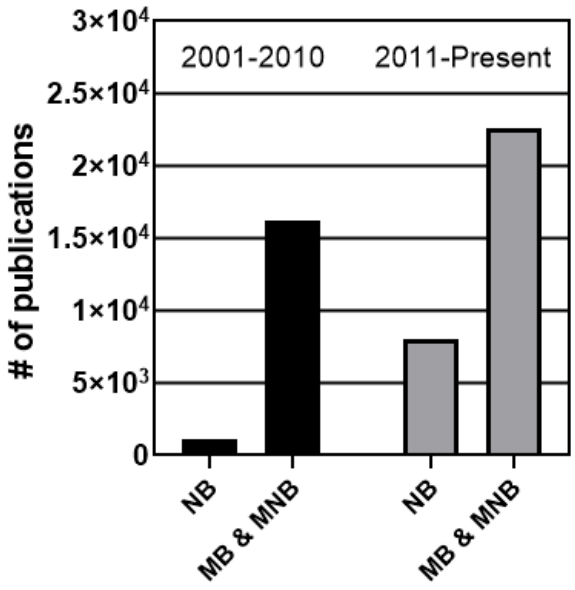

Figure 2.7: Number of publications regarding nanobubble (NB) and microbubble & micro-nano-bubble (MB & MNB).
To be noticed, 'nanobubble' here only includes bulk NB. Data retrieved from Google Scholar on 03/08/2022.

In the field of biological and clinical study, bulk NBs have been utilized as ultrasound contrast agents [48, 49, 50] and drug delivery carriers [50, 51, 52, 53, 54], to take the advantage of their slow decay rate, high intercellular permeability and superior acoustic properties.

But the most studied application of NBs was in the field of water treatment. As gas donors in the water, NB was firstly studied to improve the efficiency of the mass transfer aeration in the water treatment. However, it is still not well established on an industrial scale [55]. In other studies, for example, it was found that air or nitrogen NBs can enhance the activity of aerobic and anaerobic microorganisms in membrane bioreactors in the water treatment plants [56]. Collapsing ozone NBs will lead to the conversion from ozone to OH free radicals, which is beneficial in the degradation of organic pollutants [57]. In surface defouling, NB showed outstanding performance in cleaning and preventing surface contamination on ceramic [58] and stainless steel [59] surfaces. The proposed theory in the former report was based on the generation of free radicals by NB collapsing, while there is no further discussion in the latter one. Jie Zhu et al. found electrolysis-generated NB has a better defouling performance on a

fouled hydrophilic surface than the hydrophobic one [60]. Furthermore, they concluded that NB defouling has a similar mechanism as detergent, which enhances cleaning by preventing the re-deposition of nanoparticles removed from the surface as in Fig.2.8.

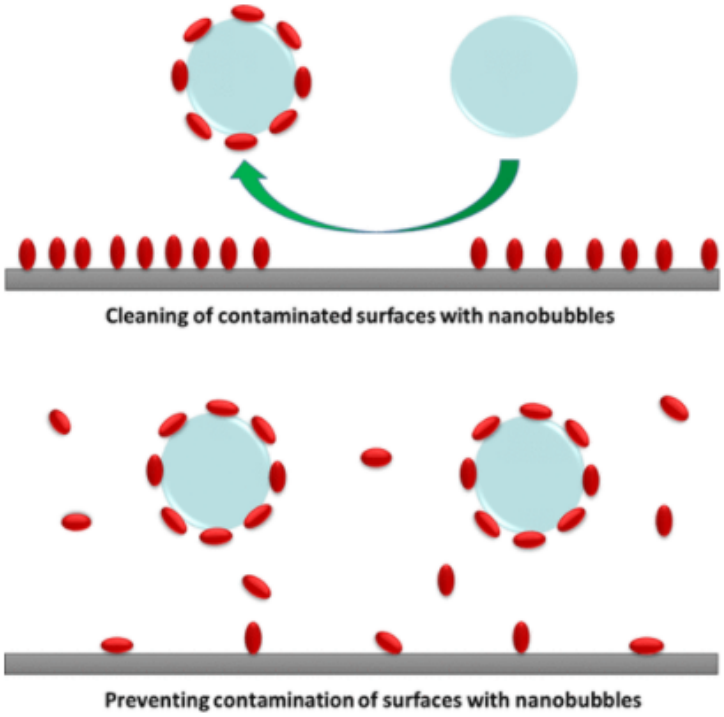

Figure 2.8: Bulk NB defouling and preventing contaminates' re-deposition on surfaces. [60]

Flotation or precipitation in water purification are the other important applications with NB in the field of water treatment. They use NBs to cluster with contaminants, like dust, chemicals, organic matter, metal ions and oils and turn them into colloids or precipitates which are easier to remove [61]. This flotation/precipitation technology for the wastewater treatment utilized NB's attraction to a variety of nanoparticles and it is also superior to normal processes in terms of both cost and performance [62, 63].

2.5 Theoretical Studies in Nanobubbles Binding Nanoparticles

Back in 2011, Oshita Uchida et al. generated O2 NB in polluted wastewater with a commercial Micro-nano-bubble generator [10]. In the TEM images of the freeze-fractured replica of the wastewater sample, a large quantity of small nanoparticles were observed on the NB surface, as in Fig.2.9. In the extended picture in Fig.2.9(a), it shows a distance between the NB and nanoparticles (impurities). Since the freezing rate was as fast as 10^2 to 10^3 *K/min*, the crystallization of ice should have little effect on the distance between the two nano-objects. This observation gave rise to a hypothesis that there are two or more forces involved when a NB binds nanoparticles to form clusters, and these forces are balanced at a certain distance, like DLVO theory, to lower the free energy through the binding interaction. However, in this study, the authors didn't provide detailed information on the composition of the nanoparticles for further study on NB clustering.

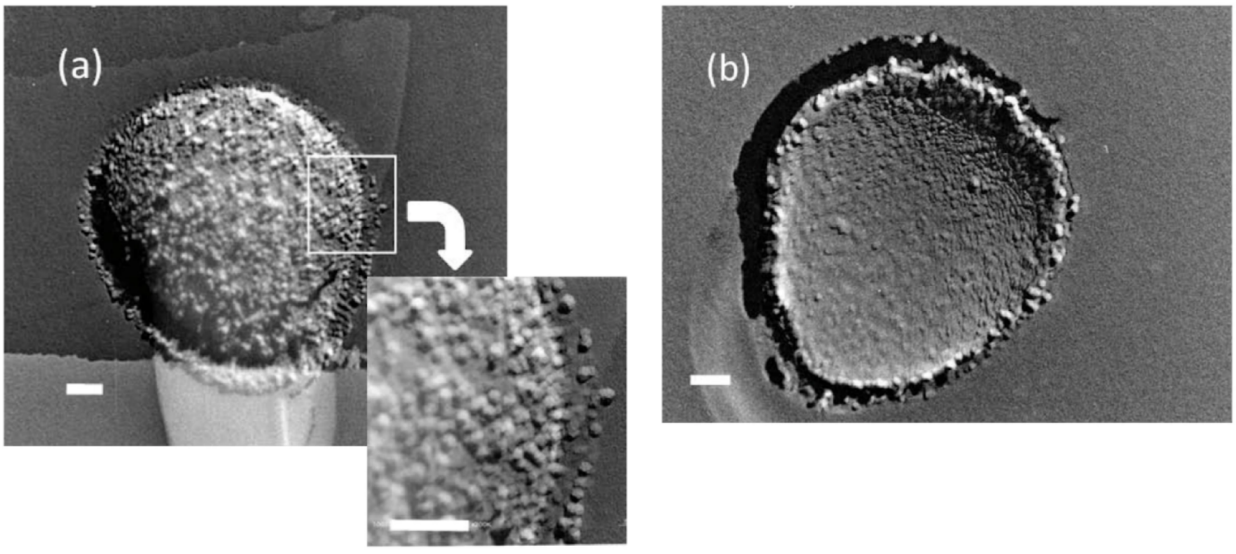

Figure 2.9: TEM images of freeze-fractured replica of the wastewater containing O2 MNBs. Each scale bar indicates 100 nm. (a, b) The MNB (850 nm in diameter) located in the center of each picture adsorbs many fine particles (20 nm in diameter) on its surface.[10]

To study the mechanism of NB clustering, one should start from the possible forces associated with the attraction or repulsion between the NB and the nanoparticles.

The first is electrostatic force. The ζ-potential measurement of the NB revealed their negatively charged surfaces, that give NBs the potential to bind cations or nanoparticles with dipoles in the liquid phase. The electrostatic force potential can be estimated with the calculation of double layer potential. It depends on the charges on both the NB and the nanoparticle, and the separation between them. The direction of the force depends on the charge type so the force could be either attractive or repulsive in different circumstances.

Secondly, van der Waals (vdW) force is an intermolecular force and always used in the mechanical analysis in the nanoscale because it is short-ranged but essential in nanoparticles' interaction. Though the vdW force was limited to be effective in the range up to numbers of nanometers [64], when the Nano-objects are close enough, vdW attraction should play an essential role in compensating the repulsive electrostatic force and the stabilization of the NB-nanoparticle cluster [65].

The third one, that is different from the two DLVO forces, is the hydrophobic interaction between the NB and nanoparticles. The gas-liquid interface of a NB can provide an area with a lower dipole moment for the hydrophobic nanoparticles, to reduce their surface tension and free energy. As a result, NB should be able to bind hydrophobic nanoparticles to form clusters as well. Unfortunately there is no established theory on the hydrophobic force potential of the interaction between suspended nano-objects, the hydrophobic force potential for a NB-binding-nanoparticle system can only be roughly estimated based on related observations and theory in two hydrophobic surfaces. The contribution of hydrophobic interaction in the interaction potential between a NB and a nanoparticle will be further discussed in Chapter 4.

There might be other types of forces that lead to the formation of clusters, such as solvation,

structural and steric [66]. Further studies are needed to have a better understanding in NB binding nanoparticles.

There are also several experimental studies on NB binding nanoparticles. Minmin Zhange et al. studied the interaction between NB generated by electrolysis and gold nanoparticles [67]. They measured the size distribution of Au nanoparticles with different sizes in NB solution with DLS. However, only when the size of Au nanoparticles is bigger than 40nm, a single population can be observed as in Fig.2.10 .

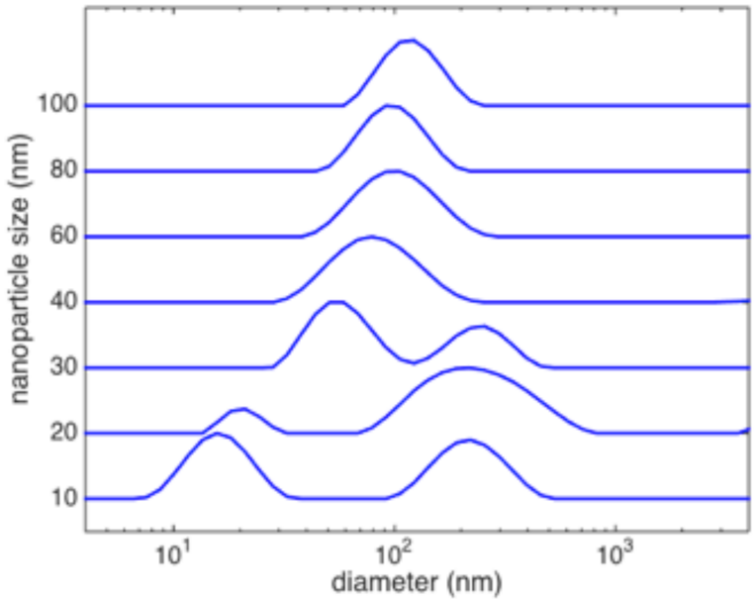

Figure 2.10: DLS size distributions of Au nanoparticles with different sizes in NB solution. [67]

Based on this observation, the authors concluded that only bigger size nanoparticles can interact with NBs and the new peaks were interpreted as the clusters of NBs and nanoparticles. The reason why the clusters have smaller size than a regular NB was explained as the size of the NBs changed during clustering. Furthermore, they proposed a hypothesis that new nucleation of NB on the surface of the Au nanoparticle must involve in the NB-nanoparticle interaction, and this process thermodynamically favors nanoparticles with bigger size or curvature.

With no more experimental evidence, it seems there might be an alternative explanation to this observation. DLS measures the collective diffusion of the bulk liquid and there is an effect of light scattering shadowing, which means the objects with higher light scattering intensity would shadow the ones with lower light scattering intensity. Therefore, in the size distribution measured by DLS, when the size of the Au nanoparticles is higher than 40 nm, the peak for nanoparticles might be merged into the only existing peak, or shadowed by nanoparticles that have higher light scattering intensity when the size difference between a NB and a nanoparticle is minimal, based on Rayleigh Scattering theory. Thus it is possible that one can still observe a similar size distribution with DLS, even if NB didn't attract gold nanoparticles. Furthermore, the gold nanoparticle has a negative ζ potential (ranging from -20 to -45 mV as reported in this work). If there is no new nucleation of NB as proposed by the authors, there must be a strong repulsion between a NB and a gold nanoparticle. As a result, no clustering between the NBs and the gold nanoparticles would be observed.

Besides the above work, George Z. Kyzaz et al. demonstrated the interaction between NB and heavy metal ions Pb^{2+} [11]. This work found a 366% acceleration in the adsorption process with an activated carbon sample with NB and determined that electrostatic force is the driving force in NB binding ions.

There is other research on NB interacting with hydrophobic or amphiphilic chemicals, for example, dodecylamine [12], amidine [13], and other organic compounds [13, 14]. These works provided more evidences of the attraction between NB and hydrophobic substances and surfactant.

Chapter 3

Interaction of Calcium Carbonate with Nanobubbles Produced in an Alternating Magnetic Field

In this chapter, the hypothesis that was made in Chapter 1 was examined, that the alternating magnetic field treatment to water introduces the generation of nanobubbles. The methods of the experimental setups and nanobubble/cluster characterization to study the nanobubble's effect on promoting the dissolution of $CaCO_3$ were described. In the discussion, the NB generation mechanism and NBs' effect on dissolution enhancing were discussed.

3.1 Background

ζ Potential Measurement

In a ζ potential measurement, ζ potential of particles is determined by measuring their velocity while they are moving due to electrophoresis [68]. When an electric field is applied, the particles that have a ζ potential will migrate towards an electrode. The migration speed is proportional to the field strength and their ζ potential. As the applied field is known and controllable in the measurement, what the apparatus does includes measuring the speed under electric field (electrophoretic mobility) and using it to calculate the ζ potential ζ with Henry's equation as Eqn 3.1.

$$U_{\mathrm{e}} = \frac{2\epsilon\zeta f(\kappa a)}{3\eta} \tag{3.1}$$

Where U_{e} is the electrophoretic mobility, ϵ is the dielectric constant, η is the absolute zero-shear viscosity of the medium, $f(\kappa a)$ is the Henry function, and κa is a measure of the ratio of the particle radius to the Debye length.

Nanoparticle Tracking Analysis

Nanoparticle tracking analysis (NTA) was first commercialized in 2006 and used to analyze the concentration and size distribution of the nano-objects in a solution [69]. This technique combines laser light scattering microscopy with a charge-coupled device (CCD) camera that can record the nanoparticles' movement in a solution. The NTA software then identifies and tracks the trajectories of the nanoparticle movement under Brownian motion to calculate

the mean-squared speed of individual nanoparticles. 2-dimensional Stokes-Einstein equation (as Eqn. 3.2) is then used to calculate the hydrodynamic radius r_h.

$$\overline{(x,y)^2} = \frac{2k_BT}{3r_h\pi\eta} \tag{3.2}$$

where k_B is the Boltzmann constant and $\overline{(x,y)^2}$is the mean-squared speed of a particle at a temperature T, in a medium of viscosity η. Besides the measurement of size distribution of the nanoparticles, the NTA data also includes the light scattering intensity of each particle, which allows the differentiation of nanoparticles in the same solution with similar size but different refractive indices according to the theory of Rayleigh scattering [70].

When using NTA to differentiate NBs with nanoparticles, one can take the advantage of the relative light scattering intensity on a third coordinate axis from the NTA data. According to Rayleigh scattering theory for objects smaller than the wavelength of the incident light [70], light scattering intensity, I, in water is positively correlated with the relative index of refraction, n, of the nano-objects as:

$$I \propto (\frac{n^2-1}{n^2+2})^2 \tag{3.3}$$

The relative index is given by:

$$n = \frac{n_o}{n_w} \tag{3.4}$$

Where n_o is the index of refraction of the nano-object and n_w is the refractive index of water. Thus, it should be possible to distinguish nanoscale objects of similar size that have different relative indices of refraction by comparing the scattered light intensity they exhibit.

The index of refraction for water is 1.33. Bunkin and coworkers [71] reported a refractive index for nanobubbles of about 1.26, which is somewhat higher than that for a gas (n_g = 1.0). The resulting value of n for NBs in water is then about 0.95. By comparison, the

index of refraction for calcium carbonate is approximately 1.51 and, therefore, its value of n in water is 1.14. The NBs of similar size should then correspond to a substantially lower light scattering intensity according to Eqn. 3.3. Hence, when analyzing the NTA data, this criteria was used to differentiate NBs from nanoparticles with similar sizes.

3.2 Materials and Methods

Alternating Magnetic Field Treatment

An alternating magnetic field (AMF) closed-loop water test systems have been built with an AMF unit (Aqua-Phyd, CA, US) with the magnets at the core have a magnetic field amplitude of approximately 0.5 T.

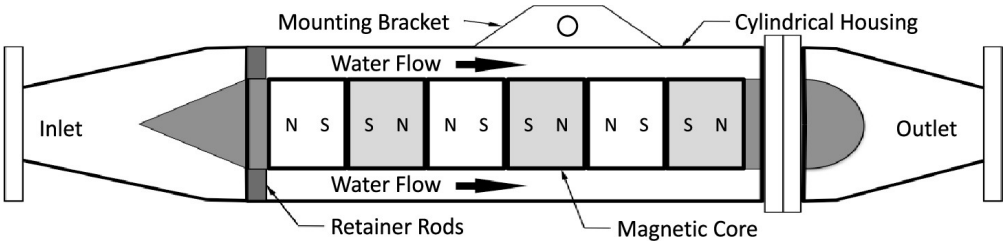

Figure 3.1: Schematic of the alternating magnetic field (AMF) treatment system.

The close-loop test system (CLTS1) as in Fig. 3.2 had a treatment capacity of 20L of water and the flow rate was approximately 15 L/min. The expansion tank was not strictly sealed and was designed to treat the water saturated with air under 1 atm. The treatment time was 3 hours. Accordingly, the total volume of water circulated through the present AMF device well over 100 times, which was determined from earlier work with this system to be sufficient to generate an effective concentration of nanobubbles [1]. This CLTS1 system was primarily designed to study the AMF treatment's effect on promoting the dissolution of

calcium carbonate in the water.

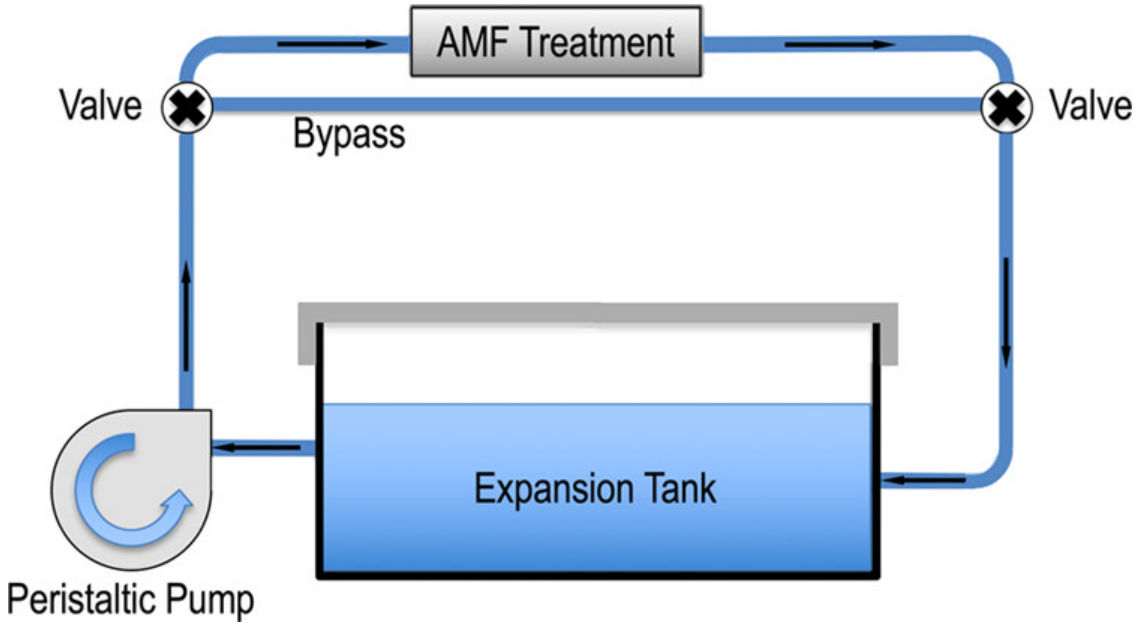

Figure 3.2: Drawing of the closed-loop test system, CLTS1.

The deionized (DI) water used for the treatments was generated from a Millipore water purification system (Thermo Scientific, MA, US) and had a resistance of 18.2 MΩ · cm. Prior to testing, the system was flushed with water several times to remove impurities. The valves in the system were used to control the water flow. Calcium carbonate (Sigma-Aldrich. MO, US.) was added to deionized water and also treated in CLTS1. For these experiments, a control solution that also contained $CaCO_3$ was circulated through an inactive AMF device that did not have the permanent magnets installed in the core tube but was otherwise identical to the active system. This inactive system was used to assure that the control solution experienced the same flow and turbulence conditions compared to the treated solution. The $CaCO_3$ was dispersed gradually into these solutions, starting from well below the solubility limit until the concentration was just below the solubility limit at 5×10^{-4} M. Once the solutions were well mixed, no particles were observed visually anywhere in the control or test solutions. The experiments with control and treated solutions were performed for 3 h corresponding to over 100 cycles, as described above. Temperature and

pH were monitored during these experiments and neither changed significantly (22 °C and pH = 8.0).

Nano-objects Characterization

The water sample collected was checked using the Tyndall method for the presence of nano-objects, that was using a laser beam through both treated and untreated water. Both the control and treated solutions were analyzed by NTA using a NanoSight NS300 (Malvern Panalytical, UK). The NanoSight instrument is equipped with a CCD camera so that the scattered light from many individual nano-objects can be tracked. Accordingly, both size and relative scattering intensity were determined for each nano-object that scattered light in the water samples. ζ Potential Measurements were carried out by a Litesizer 500 (Anton Paar, Austria).

3.3 Results and Discussion

AMF treatment to pure water

The water sample was checked for the existence of Nano-particles using the Tyndall effect shortly after 3 h of AMF treatment. In Fig. 3.3, a photograph of this effect can be seen in a comparison with untreated DI water that was circulated through the present system for 3 h with AMF bypassed. Compared with untreated DI water on the right side of Fig. 3.3, a bright trace in the horizontal direction of the incident light can be clearly seen in the AMF-treated DI water on the left side of this figure. This trace indicates that there are colloid objects in the suspension after the AMF treatment. In this case, the objects were

most likely a population of NBs as steps were taken to avoid introducing impurities during the AMF treatment.

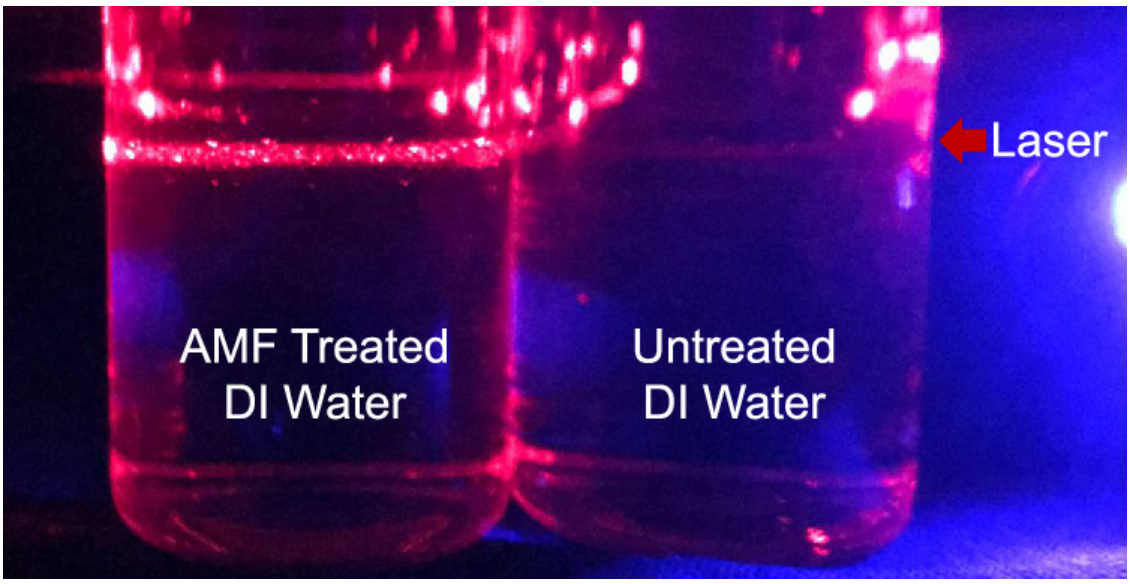

Figure 3.3: Scattering of a laser beam through both AMF-treated and untreated DI water based on the Tyndall effect.
The bright trace manifested in the treated water indicates the presence of an ample nano-object population.

The ζ potential for the AMF-treated DI water determined with a Litesizer 500 shows that the mean ζ potentials (35.5, 35.8, and 39.5 mV) were in the range of ζ potentials measured for NBs at room temperature and neutral pH reported by others (10 to 40 mV [30]). By comparison, attempts to measure a nonneutral ζ potential for untreated DI water were unsuccessful due to the extremely low number of charge carriers in the water. As such, the only plausible explanation for this results is that the present AMF treatment induces the formation of NBs in DI water.

AMF treatment to $CaCO_3$ solution at its solubility limit

The size distributions of nano-objects from the NTA measurement on (a) untreated (control) solution of water containing 5×10^{-4} M $CaCO_3$ and (b) this solution after the AMF treatment were presented in Fig. 3.4. It can be seen that the number concentration was greater after AMF treatment and reached a maximum of 6×10^7 mL^{-1} for a size of about 90 nm. By contrast, the maximum concentration of $CaCO_3$ nanoparticles in the control untreated water was approximately 3.6×10^7 mL–1. The extremely small size of the nano-objects (< 90 nm) in Fig. 3.4(a) suggests that they are unstable embryos that are forming and dissolving, which is consistent with the concentration of $CaCO_3$ being at the solubility limit. The bigger nano-objects (> 90 nm) in this figure can be corresponded to the NBs generated by water pumping, and the proposed mechanism was explained in Chapter 3. We note that the average size of the objects was significantly greater in the treated solutions and that the distributions go out to 330 and 400 nm in Fig. 3.4(b). By comparison, the object size distributions in the control solutions go out to about 200 nm.

Additional insight on the interaction between air NBs generated by AMF and nanoparticles is revealed by including the relative intensity of the scattered light for each solution as shown on three-dimensional (3D) plots in Fig. 3.5. We note that only one peak along the relative intensity scale is observed for the untreated solution. This result was expected as this solution only contained $CaCO_3$ at its solubility limit. However, three distinct peaks along the relative intensity scale can be seen for the AMF-treated solution in Fig. 3.5(b). These peaks indicate that three different types of objects were present with their own distinct indices of refraction. We note that the peak corresponding to the intermediate relative intensity was the largest in terms of both concentration and particle size. This peak primary accounts for the distribution noted in Figure 3.4(b) for the AMF-treated solution. Considering the smaller peaks, we would expect those to correspond to nanoparticles of $CaCO_3$ with a higher index of refraction at the high end of the relative intensity scale and NBs with their lower index of

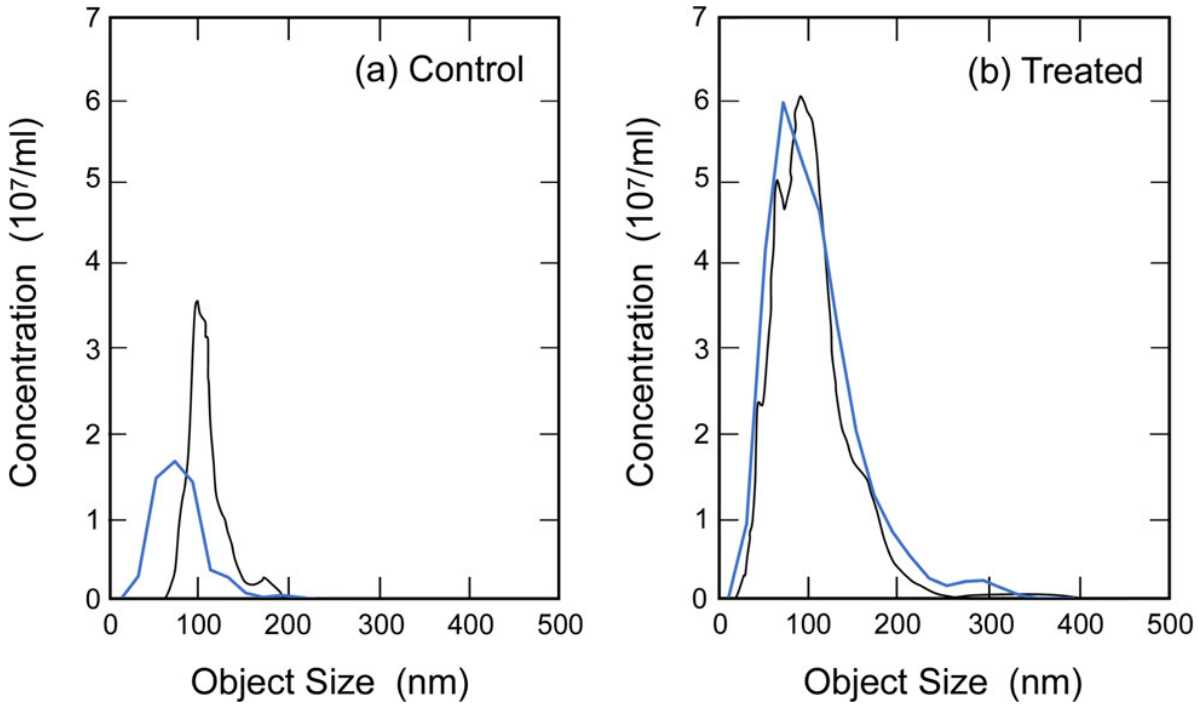

Figure 3.4: Size distributions for (a) control and (b) AMF-treated water containing 5×10^{-4} M calcium carbonate. Replicate sets of measurements are shown for each condition.

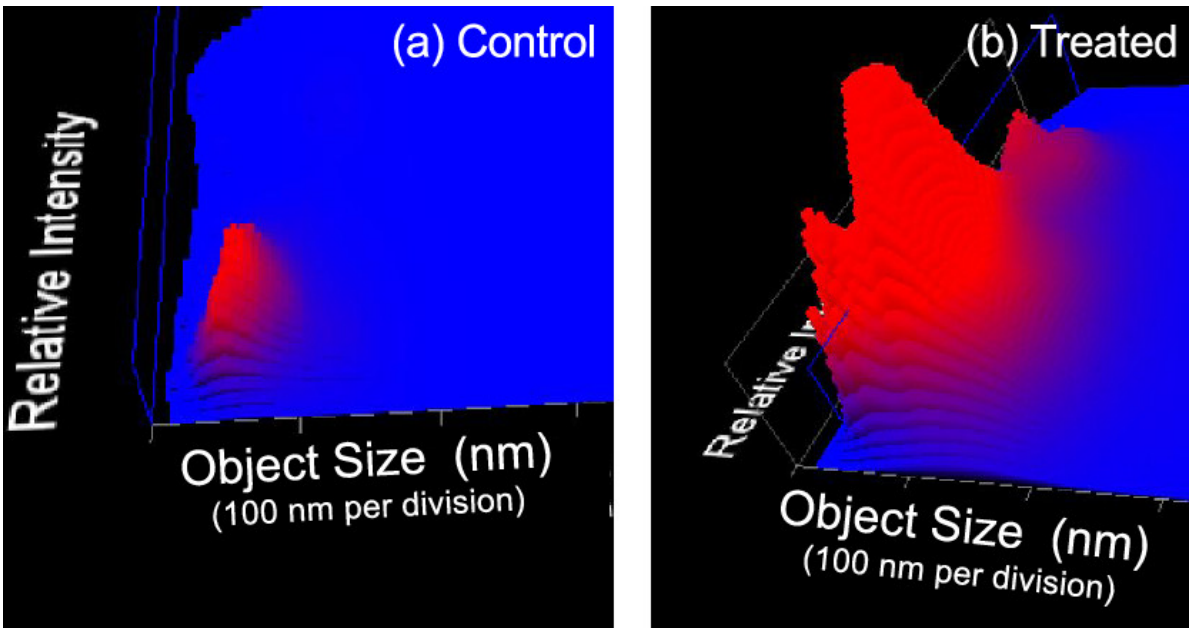

Figure 3.5: NTA results corresponding to data shown in Fig 2 (black lines) revealing both relative scattering intensity and object size for (a) control and (b) AMF-treated water containing 5×10^{-4} M $CaCO_3$.

refraction at the lower end of relative intensity. It follows that the taller intermediate peak that also extends to larger object size compared to the other lower peaks could correspond to clusters of both $CaCO_3$ nanoparticles and NBs bound together.

In a solution containing $CaCO_3$ at its solubility limit, there are Ca^{2+}, $CO_3{}^{2+}$ ions and $CaCO_3$ embryos forming and dissolving with time. In the case of NBs interacting with Ca^{2+}, based on DLVO theory, both the two forces are attractive hence the binding/clustering is bound to happen. The proposed mechanism of the interaction is that the negatively charged NB surface attracts the calcium ions by vdW and electrostatic forces. This aggregation increased the local Ca^{2+} concentration on the NB surface that accelerates the formation of embryos. On the other hand, the concentration of the free Ca^{2+} in the bulk liquid would be lowered to levels well below the solubility limit, which promotes the dissolution of bulk calcium carbonate and embryos. The process is depicted schematically in Fig. 3.6.

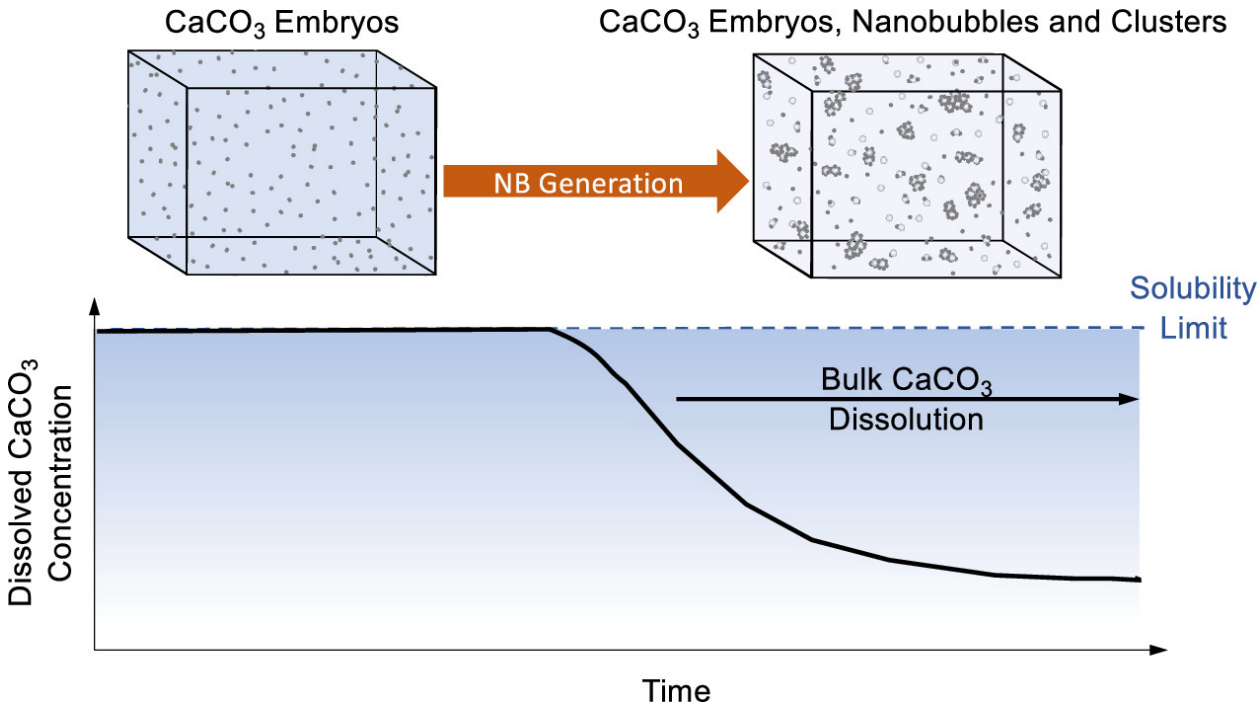

Figure 3.6: Schematic of the effective reduction in the dissolved CaCO3 concentration by the clustering of nanoparticles (embryos) of CaCO3 with NBs that are continuously generated.

Though a $CaCO_3$ embryos is electroneutral, it still has a dipole moment as an ionic compound. The negatively charged end then can be attracted by the electrical double layer of the NBs, where the repulsion from the further positively charged end is weaker due to the exponential decaying profile of electrical double layer potential [72]. Hence the overall interaction is also attractive and it indicated that a NB can also bind the embryos directly.

3.4 Conclusion

A novel water treatment system that induces an alternating magnetic field in flowing water was investigated for its ability to produce nanobubbles. It was found that the potential for deionized water treated with this system was between 30 and 40 mV, which is characteristic of nanobubbles produced in neutral water at room temperature. NTA measurements with water containing 5×10^{-4} M $CaCO_3$ also indicate the production of nanobubbles using AMF as well as a clustering interaction with $CaCO_3$ nanoparticles. It appears that the present alternating magnetic field system may be destabilizing dissolved gas in water that in turn leads to nanobubble formation. The present AMF treatment previously led to the removal of tubercle deposits on the interior walls of pipe samples from a cooling water system at the Three Mile Island Nuclear Power Station as described in Chapter 1. The present results suggest that this removal could have resulted from NB–nanoparticle clustering, which led to the dissolution of compounds, such as $CaCO_3$, that are commonly found in tubercles.

Chapter 4

Study of AMF-generated Nanobubble Promoting *ex vivo* Dissolution of Human Atherosclerosis Plaque in Coronary/Peripheral Arteries

Methods and the experimental setup we developed to treat human atherosclerosis plaque followed by the preliminary experiments with *ex vivo* dissolution of rabbit atherosclerosis plaque with NB are described in this chapter. The methods of investigating nano-objects and characterization of atherosclerosis plaque are presented. Finally, the experimental results and the mechanism in the dissolution of human atherosclerosis promoted by NBs are described.

4.1 Background

Atherosclerosis

Atherosclerosis is a chronic inflammatory disease and it is a build up of plaque in the walls of arteries. The related cardiovascular diseases take approximately 17.9 million people's lives every year and are the root cause of approximately 32% of global mortalities according to the World Health Organization(WHO) [73]. Atherosclerosis plaque causes coronary artery and peripheral artery disease because it can narrow and harden the arteries and causes obstruction of blood flow. Atherosclerosis often has no symptoms before a plaque rupture that can cause myocardial infarctions and strokes, even worse, death.

The structure of a coronary artery with atherosclerosis is as in Fig.4.1. The composition of plaque usually includes: lipids, cellular debris and calcium. The formation of calcified plaque involves complex signaling pathways and bone-like genetic processes [74]. During atherosclerosis, calcification is initiated by vascular smooth muscle cells within the arterial wall that obtain an osteoblast-like phenotype and release hydroxyapatite (HAp), $Ca_5(PO_4)_3OH$. Without a treatment, the accumulation of the insoluble deposit HAp continues to build up the plaque until a deadly disruption occurs.

Thanks to the researchers in the field of cardiovascular disease who put great effort, we now have a better understanding of Atherosclerosis's pathophysiology and more methods of medical intervention or therapies have been proposed [76, 77, 78]. For examples, stent implantation has been widely used and it uses a stainless steel or bio-compatible materials stent platform to expand the narrowed or blocked arteries and maintain the normal cardiovascular functions [79]. However, current stent implantation cost is still very high, in the range of 48,000 to 57,000 USD per patient in the USA [80].

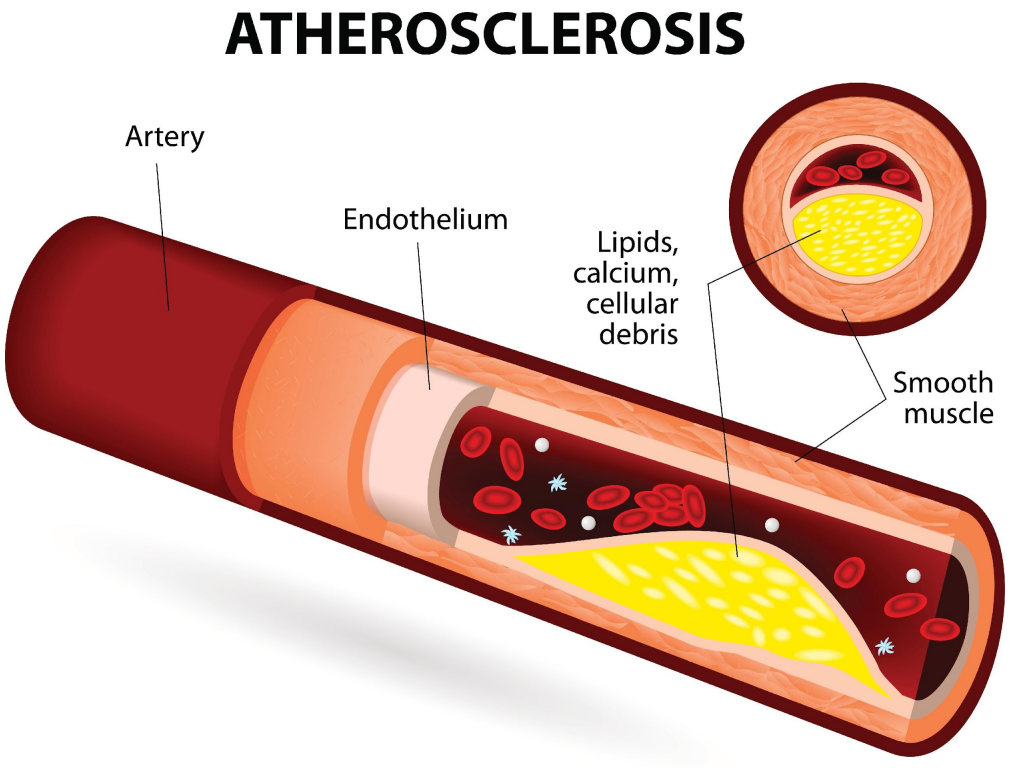

Figure 4.1: Schematic diagram of atherosclerosis plaque in an artery. [75]

Intravascular Optical Coherence Tomography

Various imaging technologies were developed to investigate atherosclerosis plaque, such as Intravascular Optical Coherence Tomography (IVOCT). In the clinic, the IVOCT system is often used for identifying the plaque [81]. As in Fig. 4.2, the light source generates the laser and the laser is divided to the sample and a reference. The backscattered light from the sample interferes with the reflected light from the reference in the fiber coupler and a signal is generated. With the collection, processing and analysis of the signal by the detector and computer, the imaging can be in real time.

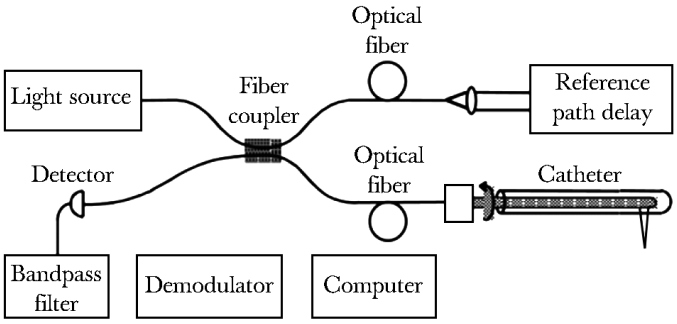

Figure 4.2: Schematic of an IVOCT system.
[82]

A Preliminary Study

There was a preliminary experiment with NB's promotion to atherosclerosis plaque dissolution, and it was carried out by Michael Robert Schutt, a former student researcher in our lab. Calcium phosphate is one of the major components in the atherosclerosis plaque. It follows that this exhibits similar properties in the presence of plaque as the nodule in the pipe of a secondary cooling water system that was mentioned in Chapter 1 and 2. The goal of this research was to determine whether exposing calcified arterial plaque to Ringer's solution treated with AMF can reproducibly cause the plaque to break down or dissolve in *ex vivo* pericardial specimens.

The aorta segments came from a New Zealand White rabbit that was fed a specific diet to promote plaque formation. The measurement of the size of the atherosclerosis plaque was performed before and after the 3 h treatment with Intravascular Optical Coherence Tomography (IVOCT) that was developed by Dr. Zhongping Chen at the Beckman Laser Institute at UC Irvine.

The result in Fig. 4.3 showed the decrease in obstruction in the artery sample after the treatment. Though the percent of the obstruction is relatively small ($< 4\%$), the performance of AMF treated Ringer's solution in dissolving atherosclerosis plaque was still significant.

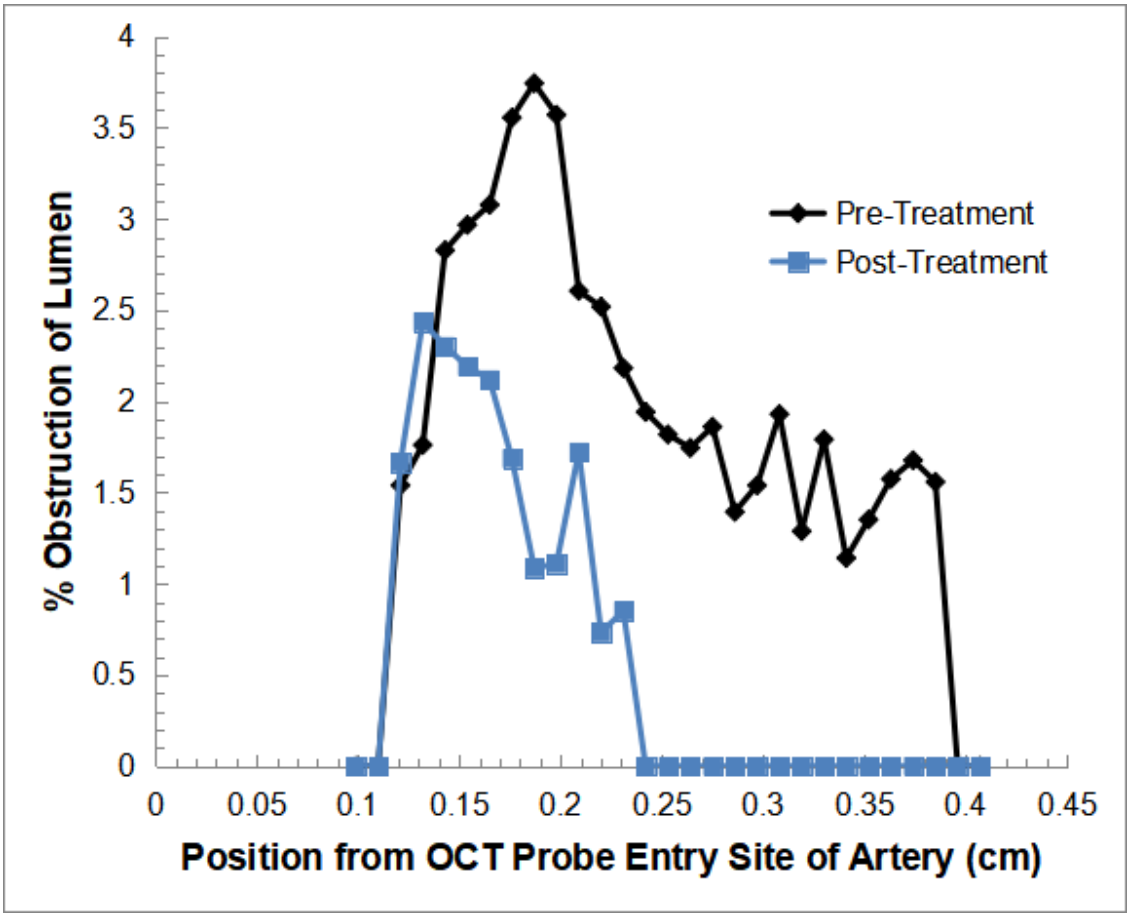

Figure 4.3: Percent obstruction of the lumen caused by the plaque deposit at each position from the OCT probe entry site of Aorta Specimen showing both pre-treatment and post-treatment OCT measurements

4.2 Materials and Methods

Nanobubble generation and Characterization

An alternating magnetic field (AMF) NB generating system was used in the present work [47]. Ringer's solution circulated through the AMF NB generator at a rate of 240 mL/min, pressure of 10 kPa and temperature of 37℃, to simulate the coronary artery environmental condition.

The composition of the Ringer's solution (Fisher Scientific, Fair Lawn, NJ) used in the

present work is given in Table 4.1. It is a saline solution that is isotonic to the body fluids of an animal. Using Ringer's solution rather than pure water in the treatment can minimize the damage to the human tissues that potentially affects the reliability of the experimental results. We note that while some calcium is present in Ringer's solution, this solution used in the present work does not also contain phosphate ions.

Table 4.1: Composition of the Ringer' solution (Unit: g/L)

$NaCl$	$NaHCO_3$	KCl	$CaCl_2$
9.2	1.5	0.4	0.2

Untreated and AMF-treated Ringer's solution samples were analyzed using a NanoSight NS300 (Malvern Panalytical Ltd, Malvern, UK) with Nanoparticle Tracking Analysis (NTA) software for analyzing NB/nanoparticle size distribution and relative scattering intensity. Detailed information is consistent as provided in Chapter 3. Each sample run in this instrument was conducted for 60 seconds and the results were averaged from more than 5 runs.

Experimental System

A circular flow test system (CFTS) was used in the present setup that consists of a pump, three-way valve, AMF system, pressure gauges, flow meters, reservoir with immersion heater, and pinch valve for controlling flow rate. A schematic of the present CFTS is shown in Fig. 4.4.

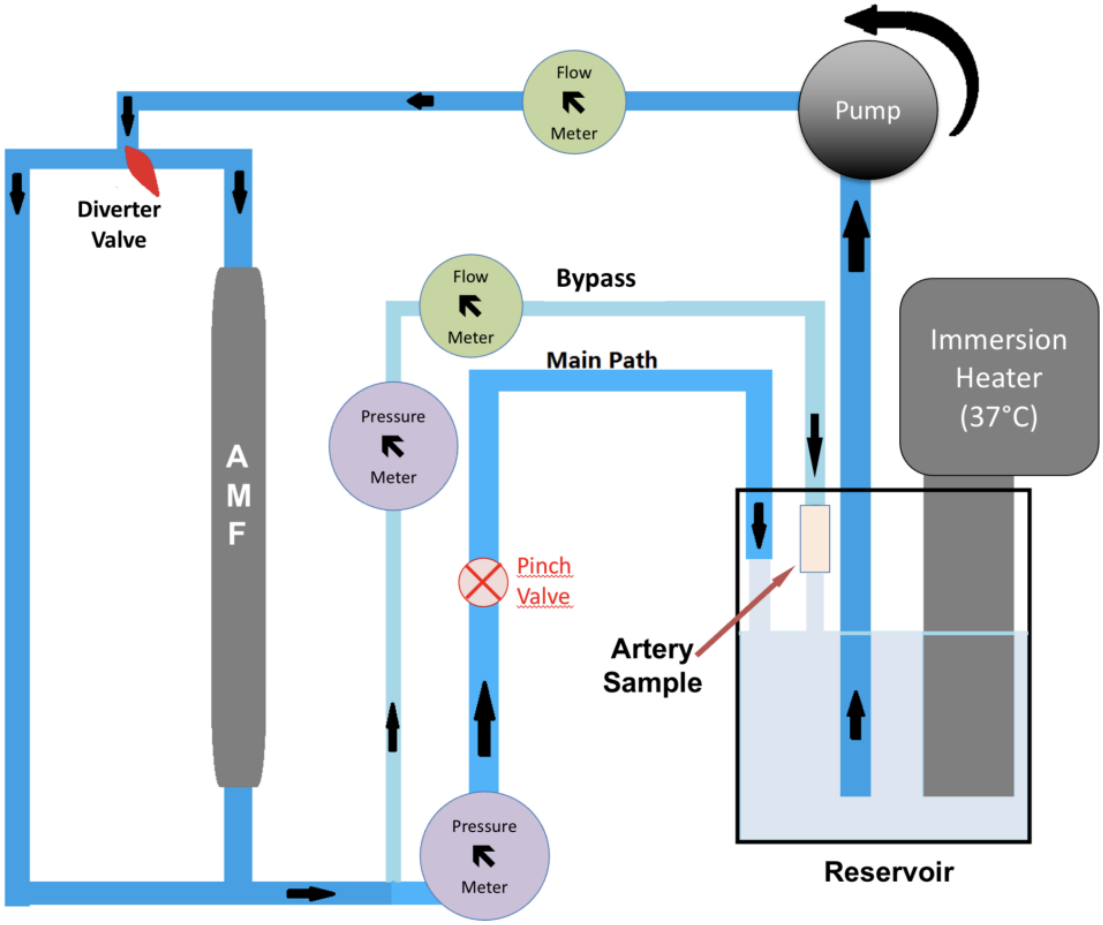

Figure 4.4: Schematic of the present circular flow test system (CFTS)

Tissue Sample Preparation

Before the experiments, fresh coronary arteries and peripheral arteries were obtained from cadavers, rinsed with Ringer's solution and frozen in a -19°C freezer. Coronary artery samples were supplied by Willed Body Program at the University of California, Irvine, while peripheral artery samples were supplied by Medtronic Inc. All methods were carried out in accordance with the University of California, Irvine (UCI) Institutional Review Board (IRB) and the Institutional Biosafety Committee (IBC). All experimental protocols were approved by the UCI IBC under protocol #2016–1570.

The coronary artery samples were numbered with a prefix as CAS, and the peripheral artery

samples were with a prefix as PAS.

Nanobubble exposure experiments

The Ringer's solution was pumped through the CFTS in bypass mode (no NBs) until its temperature reached 37°C. Each artery sample was mounted at the side stream outlet to the reservoir (see Fig. 4.4). A side stream was used to reduce the flow rate through the artery sample to be consistent with physiological flow rates. For test conditions, nanobubbles were added to the system by switching the diverter valve shown in Fig. 4.4. Another valve in main flow path was used to adjust the flow pressure from 10.0 kPa to 10.7 kPa with a fixed flow rate of 240 mL/min. Exposure to flowing Ringer's solution for most samples was performed for 4 hours. Exceptions were samples CAS 5 and CAS 6 that were treated for 6 hours in total, and plaque scanning was performed every 2 hours during interruptions of the experiments.

Intravascular optical coherence tomography

The Intravascular optical coherence tomography (IVOCT) system with a 1.7 μm swept-source laser was developed in Prof. Zhongping Chen's lab at the Beckman Laser Institute, at University of California, Irvine [81]. The IVOCT was performed with the help of Yan Li and Saijun Qiu at Chen Lab. This system uses a laser with a 1310 nm wavelength and has an axial resolution of 12 m and a transverse resolution of 30 μm. The speed of the probe was set to 3 mm/s, allowing for an acquisition rate of 50 frames per second and the corresponding distance between two frames is 60 μm. This method is ideal for arterial samples since the probe can image plaque over the entire surrounding artery wall at each frame position. IVOCT images of the entire arterial tissue sample were obtained before

and after exposure to the Ringer's solution in the CFTS for three hours. Once all of the IVOCT images for a given sample were acquired, plaques in the images were located and tracked in all of the frames in which each plaque was observed, neighboring plaques and other morphological features.

Though there are three types of atherosclerotic plaques: fibrous, lipid and calcified types, IVOCT can easily distinguish calcified plaque from the normal tissue and the other plaque types because the calcified type of plaque has the lowest backscattered light coefficient ($\mu b_{Calcium}$ = 4.9±1.5 mm^{-1}, compared to $\mu b_{Fibrous}$ = 18.6±6.4 mm^{-1}, μb_{Lipid} = 28.1±8.9 mm^{-1}) in IVOCT scanning [83].

Backscattering is positively correlated to the grayscale on the IVOCT images. The lowest backscattering results for calcium containing plaques, as in Fig. 4.5. Since other surrounding soft tissues in the arterial wall give rise to relatively high levels of backscattering, the calcified plaques tend to give rise to more contrast with the surrounding tissues compared to the other plaque types. If not stated in the results, the default plaque type measured using IVOCT in the present work was calcified plaque.

Six heart coronary artery samples (CAS) and two peripheral superficial femoral artery samples (PAS) were treated in the CFTS with Ringer's solution, with or without NBs. One plaque was identified using IVOCT in each sample. The volume of each plaque was measured over multiple frames before and after the treatment using ImageJ image analysis software (National Institutes of Health, Bethesda, Maryland, USA).

Test specimens CAS 1, CAS 3, CAS 5, and PAS 1 were exposed to Ringer's solution containing nanobubbles (NBs), while control samples CAS 2, CAS 4, CAS 6 and PAS 2 were exposed to unaltered Ringer's solution.

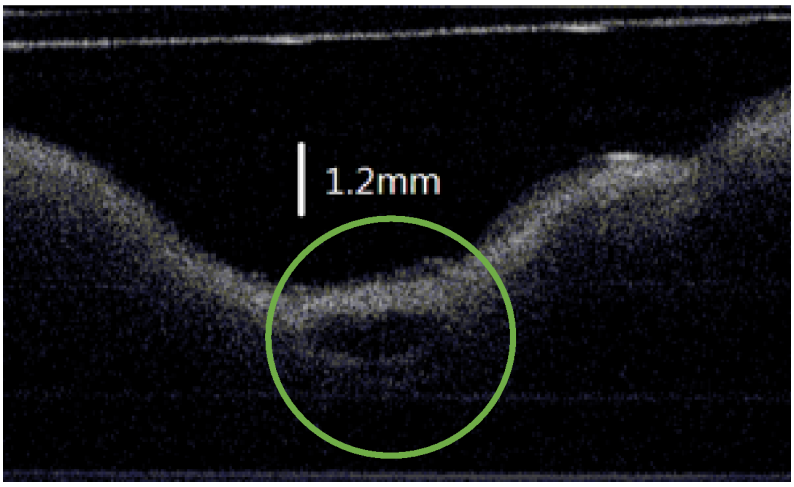

Figure 4.5: IVOCT image of coronary with calcified plaque within the green circle

4.3 Results and Discussion

Nanobubble/nanoparticle Measurements

Fig.4.6 shows NTA data for Ringer's solution treated in the present CFTS both with and without the addition of NB, as 3D plots of nanoscale object concentration as a function of size and light scattering intensity. In the test groups (NB Treated), two distinct peaks with comparable object concentration and size but different light scattering intensity were observed. For the control replicates, there is only one prominent peak shown in the figures.

There are both calcium ions and bicarbonate ions in the present Ringer's solution (Table 4.1). For the present conditions of 37℃, 1 bar of air pressure and pH of 7.3, the solubility of calcium carbonate is approximately 2 mmol/L. This concentration is close to that for calcium ions in Ringer's solution. Thus, it follows that calcium carbonate embryo NPs were forming and dissolving in the liquid phase during the present experiments. The peaks in Fig. 4.6 with higher light scattering intensity for the test groups could be produced by nanoparticle clusters assuming that the embryo nanoparticle becomes stable once it binds to a NB, which reduces its surface energy. The peaks at lower light scattering intensity in the test replicates

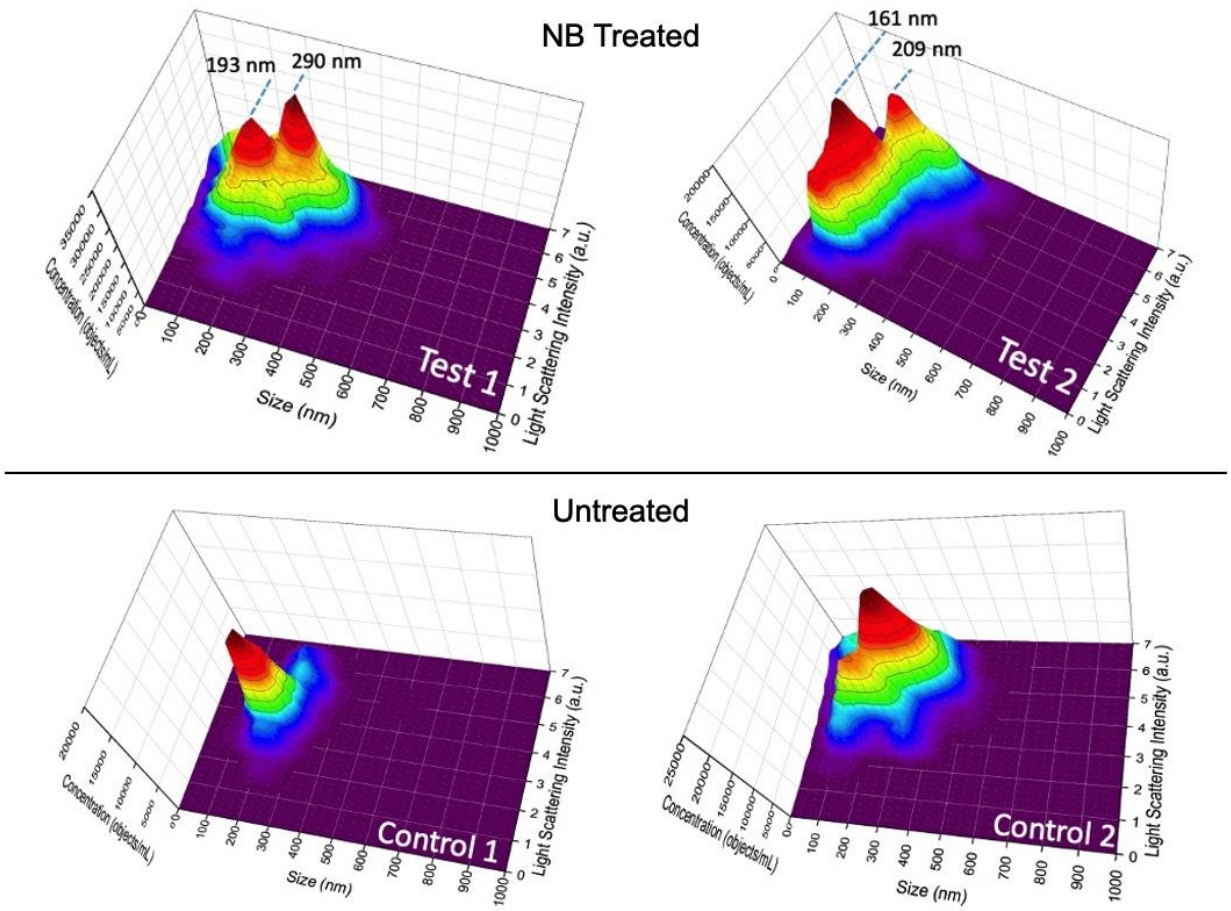

Figure 4.6: Replicate sets of NTA data plotted as size and relative light intensity (arbitrary units) plotted as a function of object concentration for Ringer's solution treated with NBs (Test 1 and 2), and that without NB addition (Control 1 and 2).
The results were obtained from four separate solution samples that were circulated through the present CFTS system for 3 hours. Each replicate was run five times in the NanoSight NS300 and the results were averaged from the five runs.

have smaller average size compared to the peaks at higher light intensity. It follows that the lower intensity peaks should correspond to light scattering by NBs, that have significantly lower index of refraction compared to calcium carbonate nanoparticles. These results are consistent with the assertion that NBs can be generated using an alternating magnetic field [47].

NanoSight NTA has also been applied to the Ringer's solution samples collected after testing *ex vivo* tissue samples CAS 1 (Test) and CAS 3 (Control) in the present CFTS. Three dimensional plots of concentration versus size and relative intensity are shown in Fig. 4.7. For these plots, each sample was run 10 times in the NanoSight NS300 and the results were averaged. Corresponding plots of concentration versus size only are illustrated in Fig. 4.8. Compared to those in Fig. 4.7, data for all intensities are integrated to a single much larger concentration for a given size in these plots. Fig. 4.7 and Fig. 4.8 indicate that the overall concentration of nanoscale objects in the solution for CAS 1 is less than 50% of the concentration in the control (CAS 3). This lower overall concentration with the addition of nanobubbles can be explained by the formation of NB-nanoparticle clusters that can substantially reduce the total number of both individual NBs and nanoparticles in solution.

Ex vivo tissue sample CAS 1 exhibited two concentration peaks for two different relative intensities for sizes below about 340 nm as shown in Fig. 4.7. The concentration peak at higher scattering intensity should correspond to nanoparticles while the concentration peak at lower scattering intensity should correspond to NBs. For CAS 3, the control without the exposure to NBs, a single peak for the nanoparticles present is present at a size of about 370 nm. The peaks corresponding to NBs in test samples 1 and 2 shown in Figure 4.6 were observed at object sizes of 193 nm and 161 nm, respectively. We then take the average of these measurements (177 nm) as an estimate of mean diameter for the NBs.

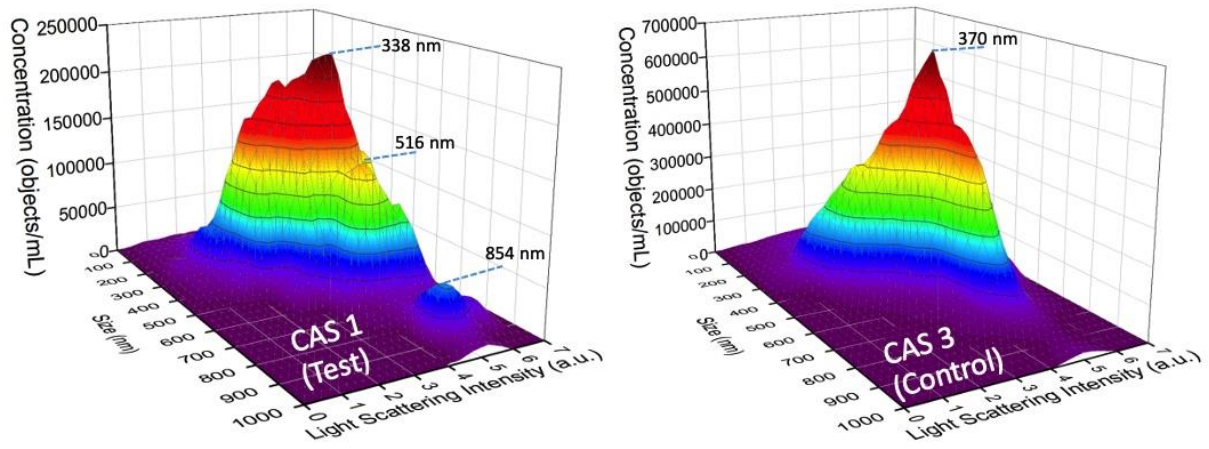

Figure 4.7: NTA data plotted as size versus relative light intensity and object concentration for Ringer's solution after treatment in the presence of *ex vivo* coronary artery samples CAS 1 (Test with NB addition) and CAS 3 (Control without NB addition).
Each sample was run 10 times in the NanoSight NS300 and the results were averaged from the 10 runs.

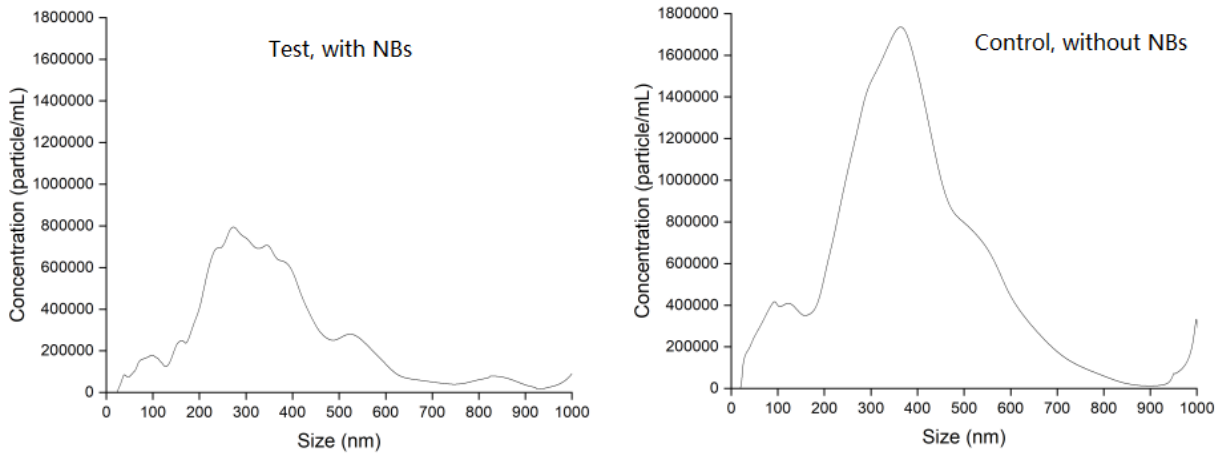

Figure 4.8: 2D size distribution of CAS 1 (Test with NB addition) and CAS 3 (Control without NB addition) from NTA data plotted as in Fig.4.7.

The minimum diameters of a single NB–single nanoparticle cluster and, based on the apparent higher concentration of nanoparticles than NBs, a cluster of multiple nanoparticles bound to a single NB can be approximated by the following:

$$d_{minimum-cluster} = d_{NB} + d_{Nanoparticle} = 177nm + 370nm = 547nm \tag{4.1}$$

$$d_{cluster-with-multiple-nanoparticles} = d_{NB} + 2d_{Nanoparticle} = 177nm + 2 \times 370nm = 917nm \quad (4.2)$$

where d is the diameter. These clusters are illustrated in Fig. 4.9.

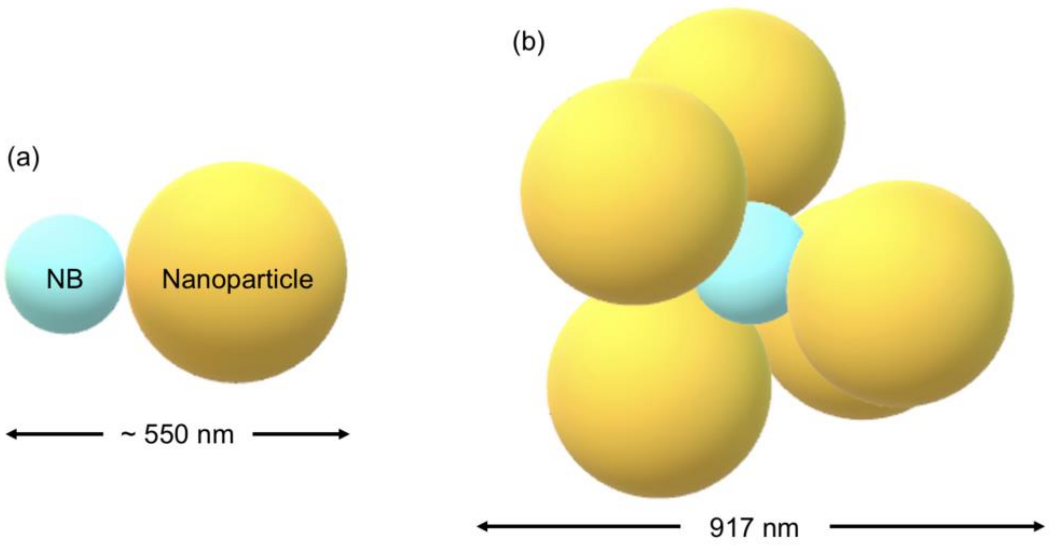

Figure 4.9: Models of a NB binding to nanoparticles.
Yellow spheres represent nanoparticles, and the blue sphere corresponds to the NB. (a) A NB binds to one nanoparticle, and the size corresponds to Eqn. 4.1. (b) A NB binds to multiple nanoparticles and the nanoparticles randomly disperse on the NB surface, and the size corresponds to Eqn. 6.2.

The assumptions made here are that the shape of nanoparticles, as well as that for the NBs, are roughly spherical and clusters form between one NB and either one or multiple nanoparticles. We note that the size of 516 nm corresponding to a concentration peak for CAS 1 is only slightly smaller than the estimate for a small dual object cluster structure predicted by Eqn. 4.1 and illustrated in Fig. 4.9(a). Further, the peak corresponding to a size of 854 nm agrees reasonably well with the estimate of 917 nm given by Eqn. 6.2.

We note that Eqns. 4.1 and 6.2 (illustrated in Fig. 4.9) predict an upper limit for the measured hydrodynamic diameter of these clusters due to asymmetry and spaces between nanoparticles. By comparison, there are no peaks larger than the single peak at about 370 nm in the plots for the untreated control (CAS 3) in Fig. 4.7 and 4.8. In sum, the

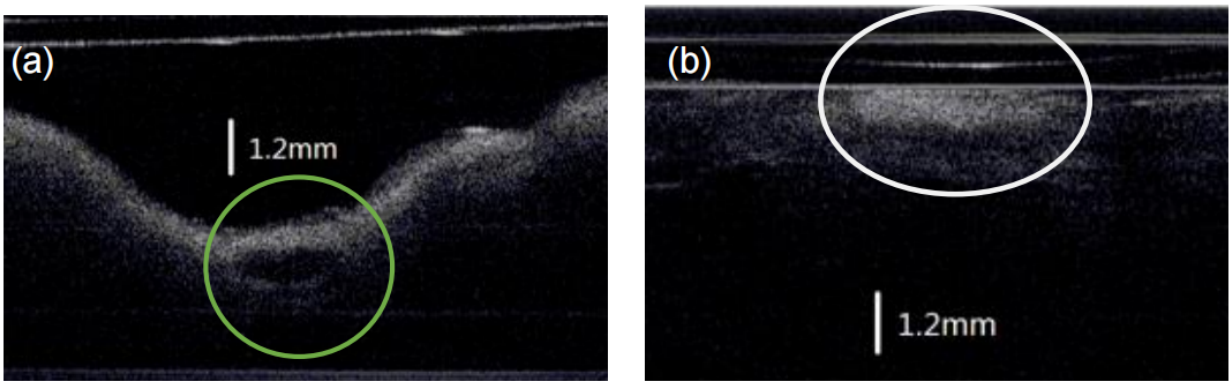

Figure 4.10: Representative IVOCT images of (a) calcified plaque and (b) lipid type plaque.

NTA evidence in these figures clearly supports the formation of clusters by NB/nanoparticle binding.

Atherosclerosis Plaque Measurements

IVOCT images are shown in Fig. 4.10 of a calcified plaque (a), and a lipid plaque (b) that were discovered in specimens CAS 1 and CAS 2, respectively. Both plaques are discernible because the calcified plaque corresponds to a lower (darker) grayscale value compared to the surrounding tissue while that for the lipid type plaque corresponds to a higher (lighter) grayscale value compared to the surrounding tissue.

The IVOCT results plotted in Fig. 4.11 indicate that plaque volume decreased by about 20% with the NB treatment (CAS 1 and CAS 2), while control groups CAS 3 and CAS 4 exhibited a plaque reduction of approximately 5%. We note that a small reduction in plaque volume in control experiments was expected since Ringer's solution does not contain phosphate which is typically a component of calcified plaque. Thus, some dissolution of $CaPO_4$ in each specimen would occur until the solubility limit of $CaPO_4$ reached in the surrounding liquid, which is very low for about 9×10^{-8} mol/L.

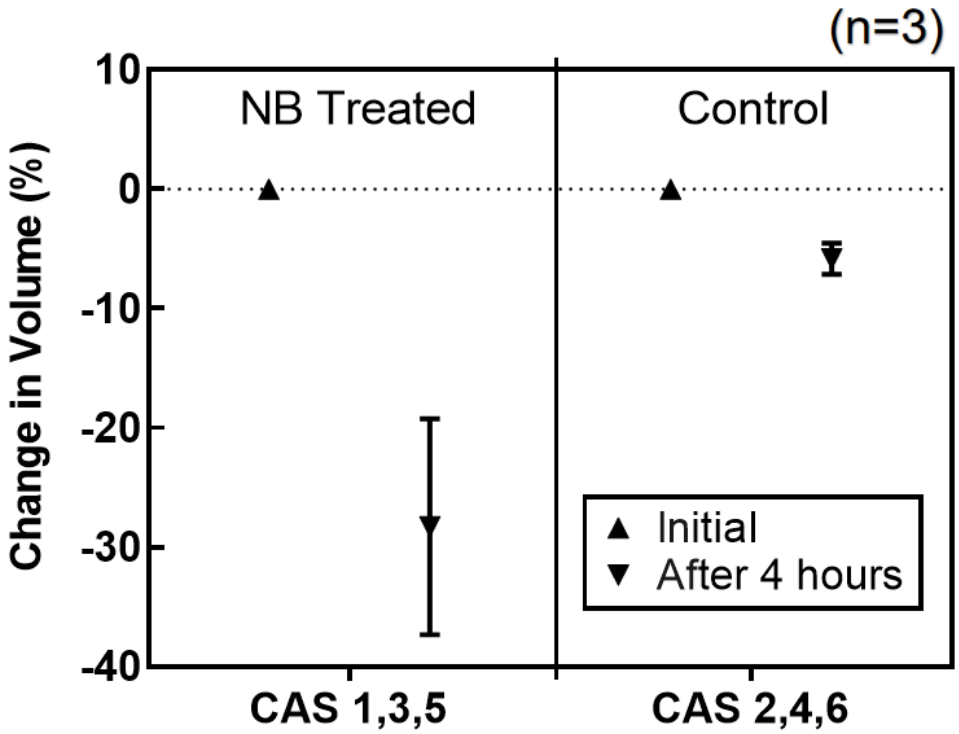

Figure 4.11: Change in volume results for CAS 1-6 determined from IVOCT images for a 4 hour treatment.

IVOCT results for two superficial femoral arteries, PAS 1 exposed to Ringer's solution containing NBs and PAS 2 exposed only to control solution, are illustrated in Fig. 4.12. The plaque size measurement before and after these experiments indicated that both plaques had much higher volume deduction than observed for the coronary artery samples, though the NB treatment with PAS 1 gave rise to a volume deduction that was 50% more than that for the control PAS 2.

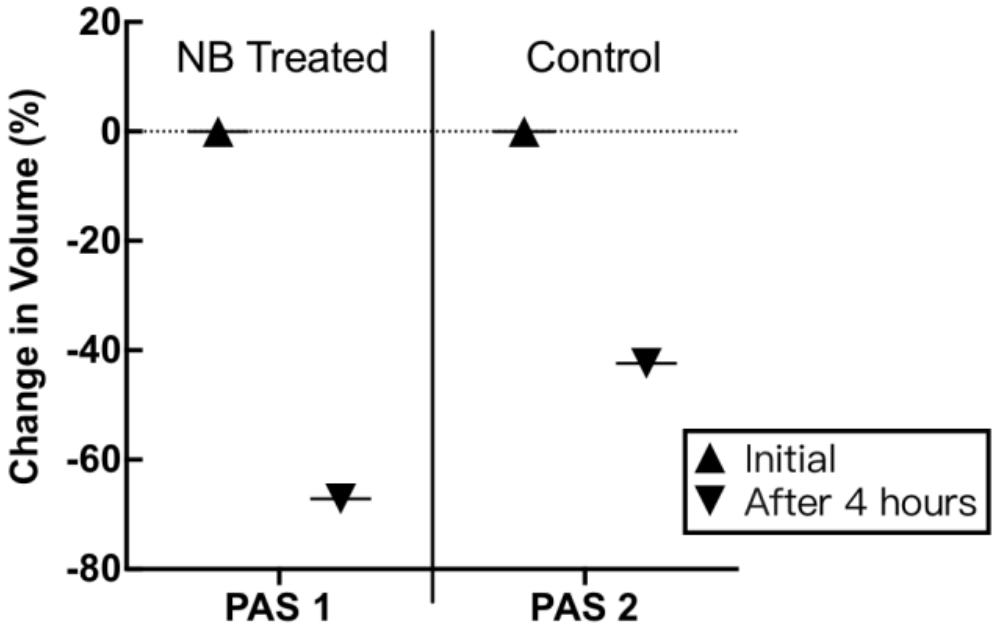

Figure 4.12: IVOCT measurements for PAS 1, which was exposed to Ringer's solution containing NBs, and PAS 2 which was a control sample exposed to unaltered Ringer's solution.

Change in volume results for CAS 5 (NB Treated) and CAS 6 (Control) determined using IVOCT are plotted in Fig. 4.13. These experiments were interrupted at three time points (2, 4, and 6 hours) for plaque measurement. The measured plaque volumes indicate that the present NB treatment consistently reduced a greater volume of plaque for a given time period compared to that for the control solution without NBs.

The present findings indicate that the present AMF NB treatment uniformly led to a greater reduction of plaque volume in *ex vivo* artery specimens. This finding is consistent with NB induced dissolution of $CaCO_3$ [47]. By comparison, the primary mineral component found in arterial plaque is typically Hydroxypatite, $Ca_10(PO_4)_6(OH)_2$ [74]. Given the reductions in concentration that resulted from the addition of nanobubbles indicated in Fig. 4.7 and 4.8, it appears that AMF generated nanobubbles may also bind to other nanoparticles that form in Ringer's solution and in the presence of *ex vivo* tissues. This assertion is consistent with the freeze fracture TEM observations of Uchida and coworkers who showed that nanobubbles can bind to nanoparticles in both saline and wastewater [10]. Although the chemical compositions

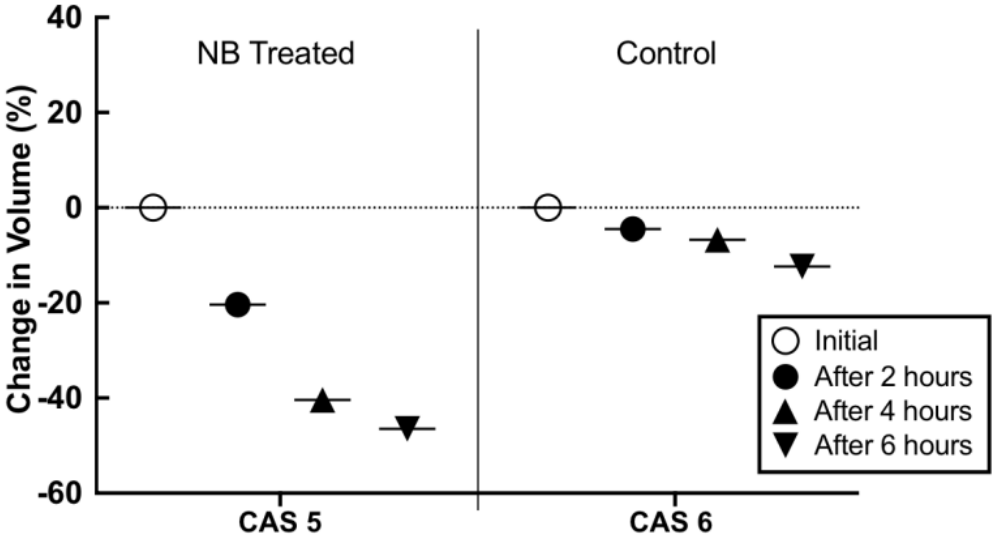

Figure 4.13: IVOCT results for CAS 5 (NB treated) and CAS 6 (control).

of nanoparticles in the Ringer's solution were not analyzed, it is reasonable to assume that some of them contained calcium, a constituent of Ringer's solution as shown in Table 4.1. It is also rational to assume that nanobubbles can bind to unstable Ca-containing embryos in this solution before they have time to completely dissolve back into solution [47].

The apparent presence of NB/nanoparticle clusters out to about 850 nm in size (Fig. 4.7 and 4.8) for the test solutions supports this assertion. We note that any clusters that reach a size larger than 1 µm would not be detected by using NTA. Therefore, larger clusters may have been produced in the present work that were not detected. It is also not known how NBs or the clusters produced may affect various parts of the human anatomy. *In vivo* animal studies are needed to determine how NBs might be safely administered as well as how to optimize and improve the performance of NBs for reducing plaque in pericardial tissues.

4.4 Conclusion

Several experiments were performed in which *ex vivo* human coronary artery tissues containing plaque were exposed to Ringer's solution with and without NBs. *Ex vivo* measurements using IVOCT consistently indicated that plaque volume was significantly reduced in the presence of NBs. The observed NB effect for reducing plaque appeared to be more distinct for coronary artery samples while the greatest reduction in plaque size was observed for the peripheral superficial femoral artery specimens. Overall, the present results indicate that there is potential for the use of nanobubbles to treat atherosclerosis.

Meanwhile, NTA measurements for Ringer's solution containing NBs were found to be consistent with the assertion that NBs bind to nanoparticles to form clusters in this solution and in the presence of *ex vivo* arterial tissues. Accordingly, we assert nanoparticles binding to nanobubbles can induce the dissolution of in plaques, which consist of the calcium compound that is in the embryo nanoparticles clustered with NBs.

Overall, though with no extra involvement of chemicals or medications, more clinical researches are needed to test the safety. Nevertheless, as a chemical-free technology to treat calcified plaque in the coronary artery, NB treatment to atherosclerosis is promising due to its low cost and extraordinary performance.

Chapter 5

Study of AMF-generated Nanobubble Promoting *ex vivo* Dissolution of Plaque in Human Aortic Valve Tissue

This chapter is a follow-up study to that in Chapter 4, with the object changed from the plaque in the coronary/peripheral arteries to the one in the human aortic valve tissue. The treatment is consistent with previous work, but the plaque reconstruction technology has been changed to micro computed tomography (Micro-CT) to accommodate the larger size of both the tissue and the plaque. The result of this study will be discussed and compared with the previous study in coronary arterial atherosclerosis.

5.1 Background

Calcific Aortic Valve Disease

Similar to atherosclerosis, calcific aortic valve disease (CAVD) is also a chronic inflammatory condition which starts from progressive fibrotic remodeling and leads to micro-/macro-calcifications in the aortic valve leaflets. The calcification, that is also called plaque, can cause aortic sclerosis and aortic stenosis. The correlation of increasing frequency of CAVD with age makes it a major geriatric problem. According to a report that investigated the data from 1990 to 2017, globally, the mortality rates haven't changed significantly since 1990 and CAVD caused approximately 102,700 deaths in 2017 [84].

Micro Computed Tomography

Computed Tomography (CT) is an imaging procedure that uses a combination of X-rays and computer technology to reconstruct the 3D structure inside an object. Similar to a regular CT used for diagnosis imaging in clinical, micro computed tomography (micro-CT) or nano computed tomography (nano-CT) were developed to visualize the inner structure with a resolution in the scale of micrometers or even nanometers. The micro-CT is with a rotating stage that allows the X-ray detector to collect the 2D image data from many different angles, and the computed tomography can be used to reconstruct the 2D section images and furthermore, the 3D structure (Fig. 5.1).

Because X-ray micro-CT is positive for calcium mineral deposition, it is suitable to scan the calcified plaque in a valve tissue sample [86]. However, in order to improve the resolution in the scale of tens of micrometers, the scanning process can take up to a few hours for each

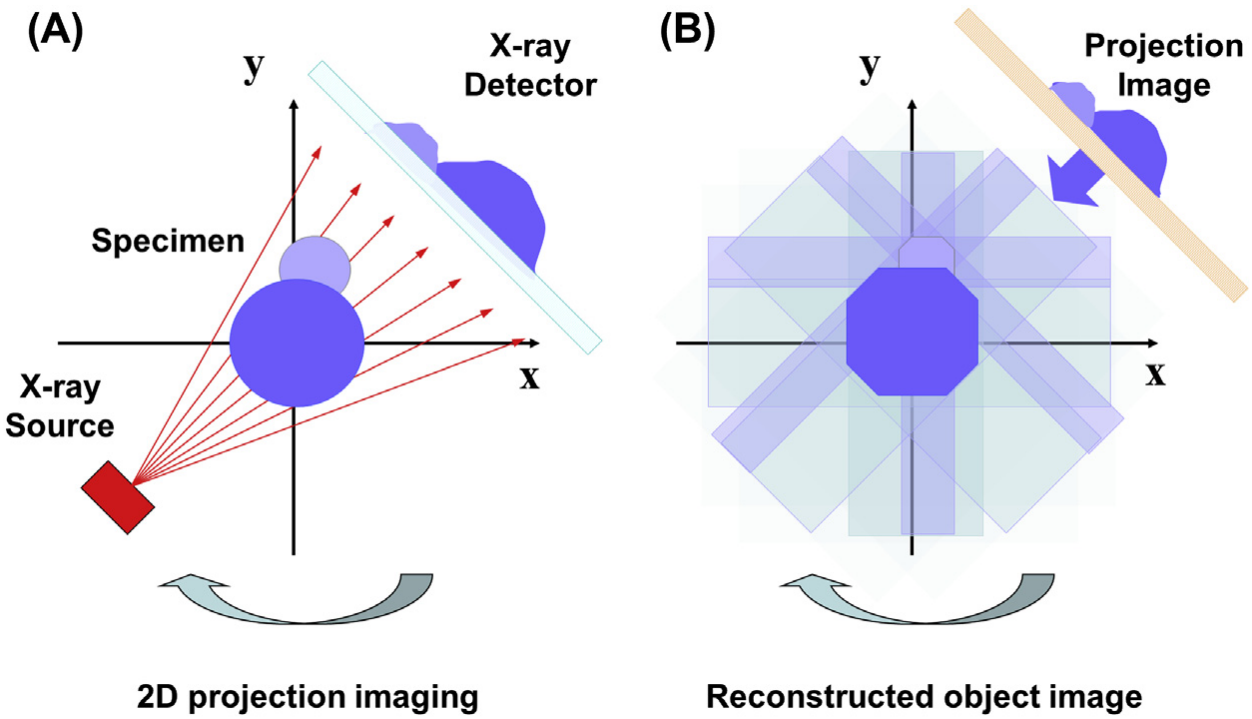

Figure 5.1: Illustration of the principle of (A) X-ray projection imaging and (B) computed tomography reconstruction.
[85]

sample. With the vibration of the rotating sample holder inside of the scanning chamber, a soft tissue sample can not be scanned directly and a sample fixing method is needed.

5.2 Materials and Methods

NB Generation and Experimental System

The CFTS used for generating NBs in Ringer's solution and treating human aortic valve samples is identical as described in Chapter 5. The sample mounting position was changed to the exit of the reservoir, to accommodate the shape of the aortic valve tissue sample as in Fig. 5.2. The pressure, flow rate and temperature were adjusted to 14.1 to 15.5 kPa, 3.6L/min and 37°C, to match with the fluidic condition in a human heart.

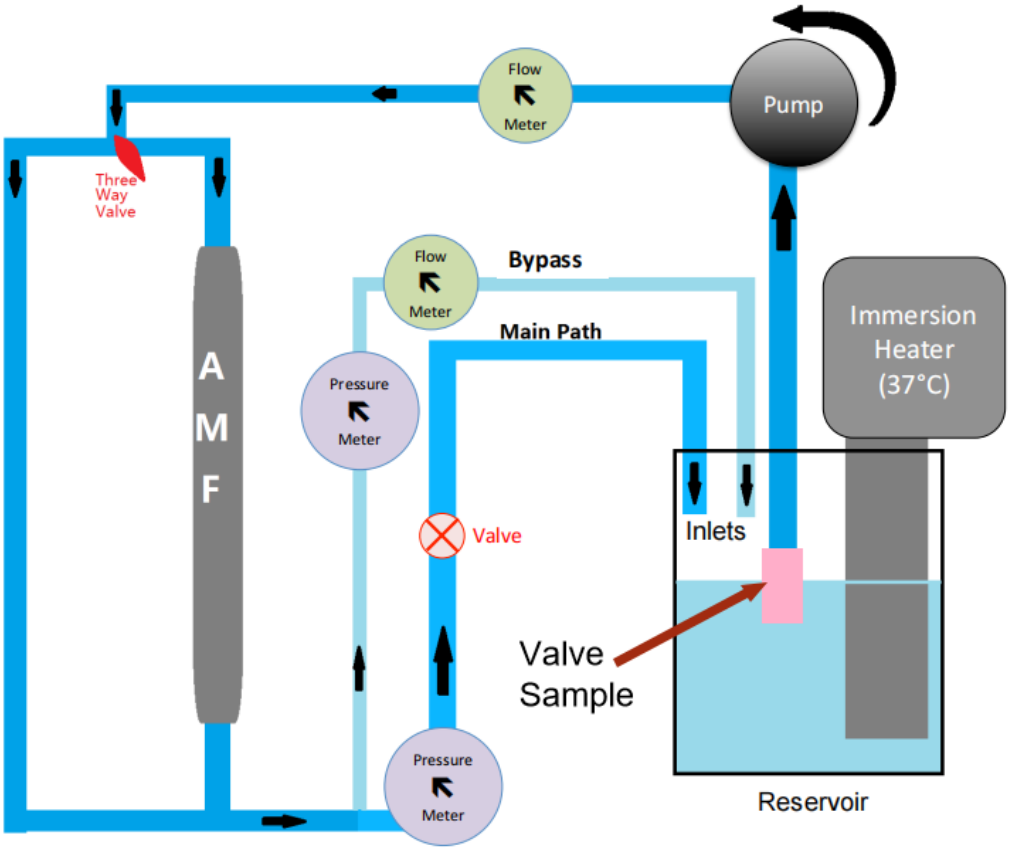

Figure 5.2: Updated schematic of the present circular flow test system (CFTS) for aortic valve tissue.

Tissue Sample Preparation

Fresh aortic valve tissue samples were obtained from cadavers, rinsed with Ringer's solution and frozen in a $-19°C$ freezer. Valve tissue samples were supplied by Willed Body Program at the University of California, Irvine. All methods were carried out in accordance with the University of California, Irvine (UCI) Institutional Review Board (IRB) and the Institutional Biosafety Committee (IBC). All experimental protocols were approved by the UCI IBC under protocol 2016–1570.

Nanobubble Exposure Experiments

The Ringer's solution was pumped through the CFTS in bypass mode (without NBs) until its temperature reached 37°C. Each aortic valve sample was mounted at the exit of the reservoir (as in Fig. 5.2). For test conditions, nanobubbles were added to the system by switching the diverter valve. Another valve in the main flow path was used to adjust the flow pressure. Exposure to flowing Ringer's solution for each sample was performed for 4 hours. Due to the limitation of available human tissues, only two aortic valve tissue samples that have plaque were tested, with one for the test with NBs, and the other one is the control without NB.

Micro-CT Scanning and 3D Reconstruction

An Xradia VersaXRM™ 410 Micro-CT (Carl Zeiss AG, German) was provided by Prof. Lizhi Sun in the department of Civil and Environmental Engineering at UC Irvine and was used to perform three-dimensional (3-D) X-ray microscopy (XRM) of the calcified plaque in valve tissue and bone samples exposed to Ringer's solution with and without NBs.

To avoid the unwanted vibration during sample rotation, each valve tissue sample was placed in a glass container containing 0.5% agarose gel during the X-ray scanning. Agarose has a gelling temperature of 34-38°C. The mixture of agarose powder and water was heated to agarose's melting temperature of 90-95°C. A room temperature water bath was used to cool down the mixture until the temperature reached 37 °C, which is the human body temperature and is safe for human tissue. Then the liquid agarose was transferred to the glass container where the valve tissue sample has been placed in. Once the gelation is completed, the sample is ready for Micro-CT scanning.

The Micro-CT image's spatial resolution for valve tissue samples is 57µm. Similar to the

procedures with IVOCT, 3D NanoCT images of the valve tissue samples were obtained before and after exposure to the Ringer's solution in the CFTS regardless of whether they were tested without (control) or with NBs. For the present NanoCT images, the volumes of CAVD plaque were determined using Simpleware ScanIP software (Synopsys, Mountain View, California, US). In the 3D structure, calcium-containing compounds correspond to voxels that have a higher grayscale value than that for other tissue or supporting materials such as glass and agarose gel. The 3D reconstruction also matches with visual observation of the plaque as in Fig. 5.3.

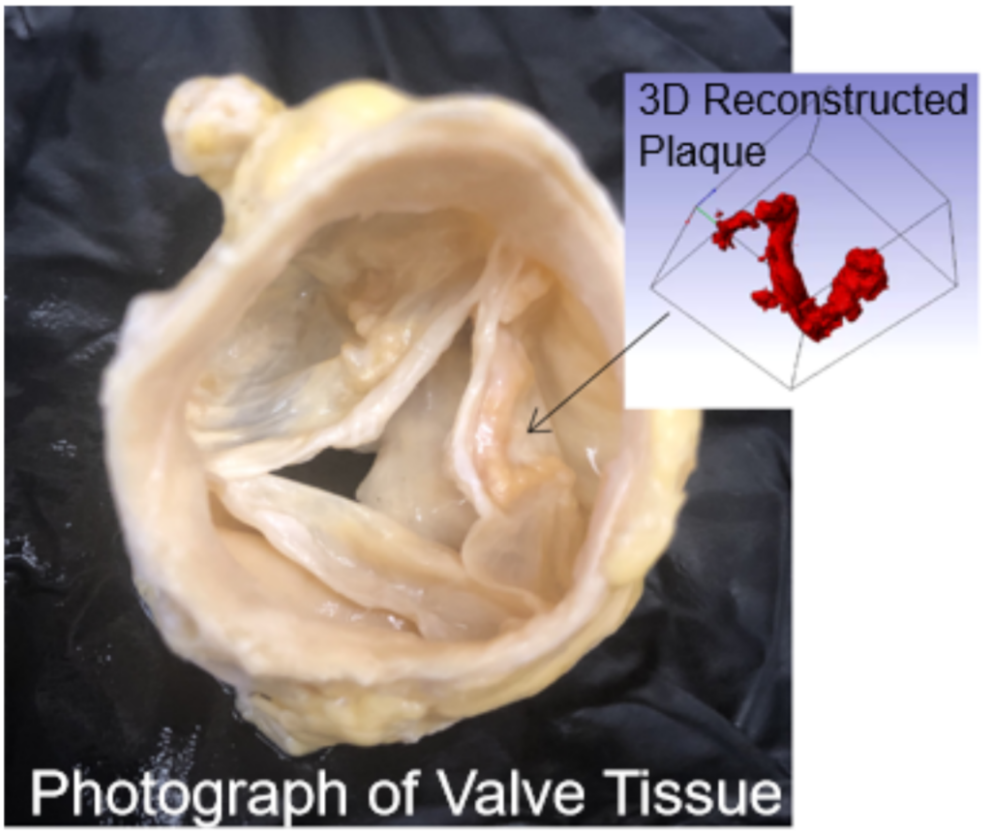

Figure 5.3: Photograph of the valve tissue sample with the 3D reconstruction of the plaque on one of its leaflets.

5.3 Results and Discussion

Micro-CT scannings were performed before and after the treatments. As in Fig.5.4 in the Test sample that has been exposed to Ringer's solution with NB for 4 hours, there is a volume decrease of about 6% while in the control sample that was only exposed to Ringer's solution without NB for 4 hours, the plaque volume deduction rate is less than 2%.

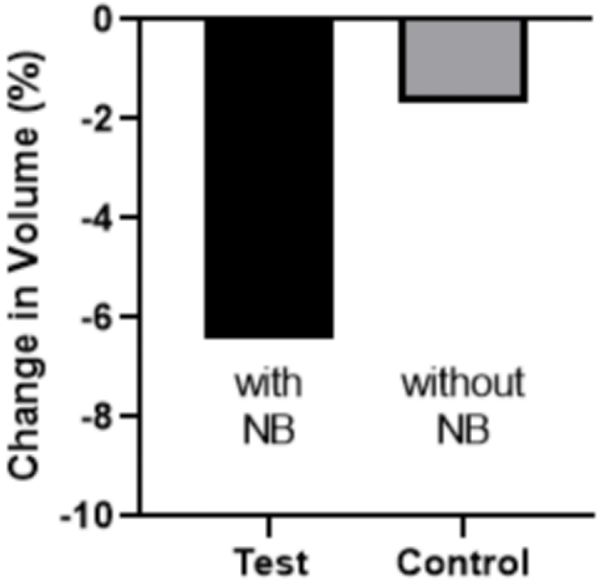

Figure 5.4: Micro-CT measurements for the plaque in the two aortic valve samples. The test sample has been exposed to Ringer's solution with NB for 4 hours, while the treatment to control sample was identical but without NB.

This result indicates that the NBs can also promote the dissolution of calcified plaque in aortic valve tissue. By comparing the change in volume rate of the plaque in aortic valve tissue and in the coronary artery samples as in Chapter 5, the performance of NBs for promoting in plaque dissolution is much better in the coronary artery samples, as the change in plaque volume in the coronary artery can go up to approximately 20% with a 4-hour exposure to NB. One explanation is that the structure of the aortic valve tissue limits plaque's exposure to NB because the plaque always occurs at the backside of the leaflets as in Fig. 5.4. When Ringer's solution with NB flowed through the valve, the leaflets opened and

pushed the plaque to the inner wall of the aorta. With less circulation of Ringer's solution with NB at the narrowed space during the 4-hour treatment, the deduction in plaque volume was also limited. A potential method to increase the plaque volume reduction is by raising the concentration of NB, and it requires further studies in the development of AMF NB technology. Another one is using a test system that is capable to generate pulse liquid flow that can rapidly open and close the valve leaflets on the valve tissue sample to simulate the heart pumping.

5.4 Conclusion

The micro-CT scanning with 3D reconstruction indicated the presence of NBs in Ringer's solution promoted the *ex vivo* dissolution of the plaque in aortic valve tissues, that corresponds to CAVD. However, the plaque volume deduction rate was only 30% as in the coronary arteries for a 4-hour exposure to NB.

But in the natural cardiac structure, coronary arteries are directly connected to the Aorta. Moreover, with similar pathogenesis as atherosclerosis, plaque's formation in CAVD always occurs simultaneously with the plaque in the coronary artery. Thus the present study showed that a treatment to atherosclerosis calcified plaque can also reduce the volume of the plaque in the aortic valve leaflets.

In this study, a pulse liquid flow was not applied to simulate the properties of the blood flow from the real heart pumping. It led to an always-open valve position that may limit the NB at the backside of the valve leaflets. Further studies of using NB to treat CAVD are needed to improve the NB circulation at the overall aortic valve leaflets.

Chapter 6

Extended DLVO theory in the interaction between Nanobubbles and Hydrophobic Nanoparticles

6.1 Background

DLVO Theory

In the middle of the 20th century, Derjaguin, Landau, Vervey and Overbeek (DLVO) developed a theory to study the interaction between colloidal particles and their clustering behavior. This theory provided a better understanding of colloidal stability [87, 88, 89]. DLVO theory assumes that the interaction potential can be well approximated by two contributions from van der Waals (vdW) and electrostatic (ES) interaction as follows:

$$W_{total}(D) = W_{vdW}(D) + W_{ES}(D) \tag{6.1}$$

where W(D) is the interaction potential and D is the separation distance between the particles. This approximation was proved to be accurate for larger surface separations and low surface charge densities [90]. Nirmalkar and coworkers, Jadhav and Barigou [65, 9] both used DLVO theory to study the stability of NBs with different NB generation methods. In their studies, the potential barrier was found that prevented NBs from coalescence from both of the two works and Fig 6.1 shows the W(r) curves presented in Jadhav's report.

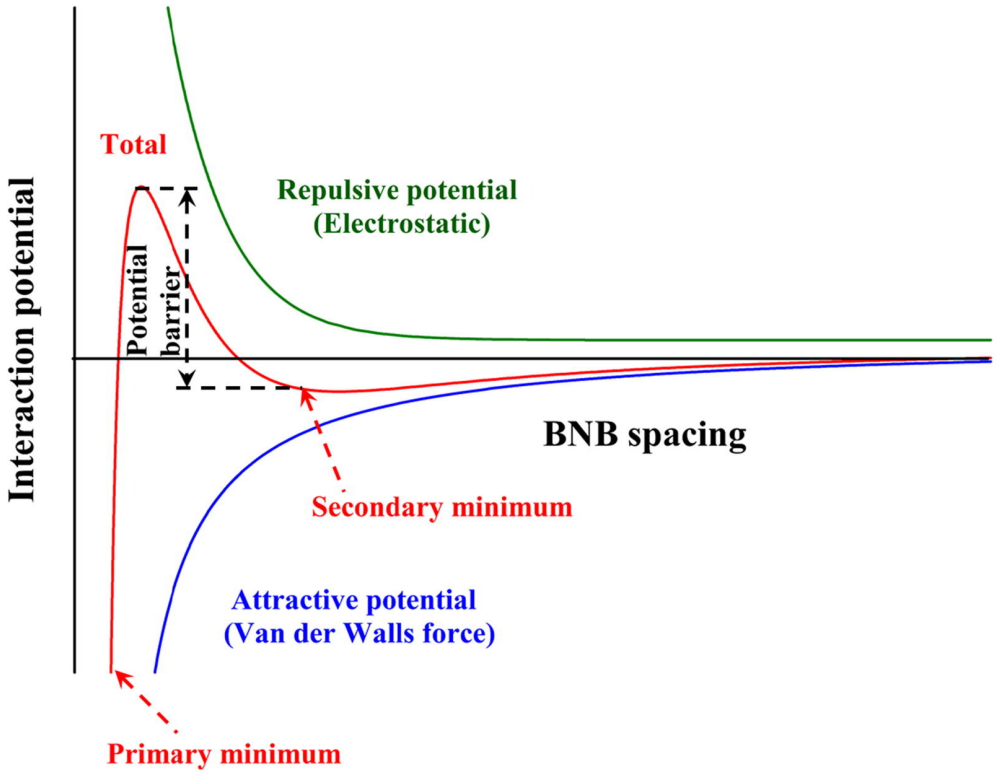

Figure 6.1: Combination of vdW attractive forces and electrostatic repulsive forces governs interaction of bulk NBs (BNBs).
[9]

6.2 Materials and Methods

A Nikuni pump NB Generator KTM MBG20N07CE (Nikuni Co., Ltd. Japan) was used to generate NBs in this study. A Nikuni pump was applies strong shear forces to pressurize a

mixture of water and air that leads to the nucleation of NBs. The gas used to generate NBs with the Nikuni pump was air and the generation time was 5 min. Nanoparticle tracking analysis (NTA) and ζ potential measurement were identical as introduced in Chapter 4, 5 and 6.

The nanoparticle interacting with NBs is Polystyrene Latex Bead (PSLB) without surface modification and a size of 100 nm. PSLB were selected as the nanoparticle for building the interaction potential model for three reasons: (i) Unlike salt nanoparticles that the size varies a lot due to dissolution and recrystallization, PSLB suspension is well monodispersed and this property is beneficial to a more accurate estimation; (ii) The ζ potential of a PSLB suspension was measured slightly negatively charged in the range of -5 to 0 mV. Therefore, the electrostatic force between a NB and a PSLB is repulsive and it allows the use of DLVO theory; (iii) Polystyrene has a hydrophobic surface and it allows the study of the contribution of hydrophobic force.

The 100 nm PSLB suspension was provided by Hyperion Analytical (CA, US) and the medium for keeping the nanoparticles stabilized was KCl solution. Before testing, the PSLB suspension was examined with NTA to confirm the monodispersity in size. Furthermore, the suspension was dried out on a 400M copper grid coated with carbon (Ted Pella, Inc. CA, US). The drying was completed in a glove box with air at room temperature for 2 hours. The loaded grid was then tested with transmission electron microscopy (TEM) carried out using a JEOL JEM-2100 CryoTEM (JEOL Ltd. Japan) to further confirm the size and shape.

The NBs generated with a Nikuni pump were collected after cycling 500 mL Millipore water with a resistance of 18.2 M$\Omega \cdot$ cm. The gas inlet was open to air therefore the gas type of the generated NBs is air. After the generation, the NB suspension were mixed with PSLB suspensions rather than adding the PSLBs in the generation system, in order to avoid the effect of water pumping on the nanoparticles and the contamination. After the NTA concentration measurement of the generated NBs, the NB suspensions were then mixed

with the 100 nm PSLB suspension. A TEM scanning has been performed with a dried air NBs-PSLB mixture sample with the same method mentioned above.

6.3 Results

The 100 nm PSLB suspension was first examined by TEM with the dried sample and NTA with a diluted suspension sample, as in Fig. 6.2. Both of the two measurements showed a good monodispersity of the PSLB sample and the spherical shape was confirmed by TEM. Specifically, the main peak in the NTA results at the size of 100 nm has a area fraction over 94% and a polydispersity index of 0.016, where the self-clusters with a size greater than 300 nm only has an area fraction of 0.59%. The ζ potential of the diluted PSLB suspension was measured at -2.4 mV.

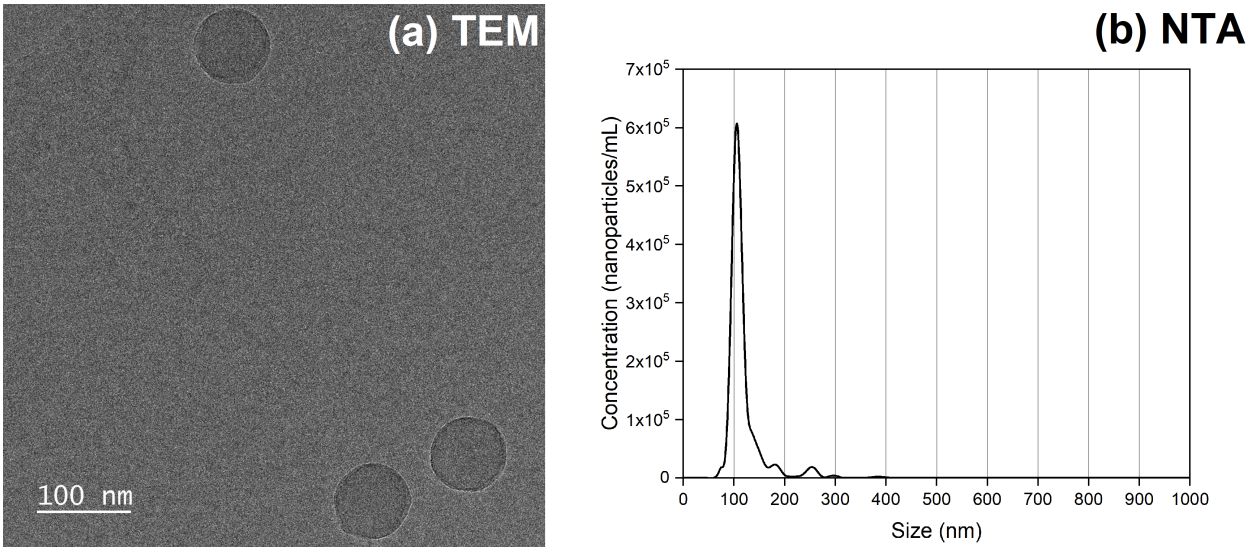

Figure 6.2: (a) TEM image of the dried PSLB loaded on a 400M copper grid; (b) Size distribution of a diluted PSLB suspension measured by NTA.

An air NB suspension was then generated by a Nikuni pump for 5 min. The measured ζ potential of the Air NB suspension was found to be -20.0 mV. The NB suspension was

mixed with the PSLB suspension. The mixing ratio of NB:PSLB=3:2 was found with NTA measurement. 3D plots of size, concentration and relative light scattering intensity for the NB sample and the NB-PSLB mixture sample that were acquired by NTA are presented in Fig. 6.3. The generated air NBs exhibited a mode size of 129 nm. For the NB-PSLB mixture shown in Fig.6.3(b), there are two peaks at around the size of 100 nm. We would expect the peak to correspond to PSLBs with a higher refractive index and NBs with their lower refractive index to correspond to the peak at the lower end of relative intensity.

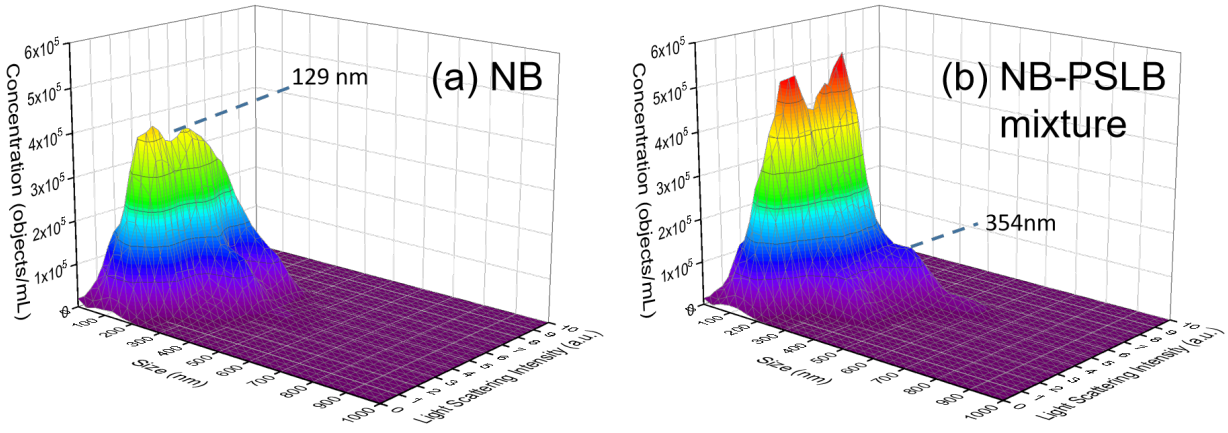

Figure 6.3: NTA data plotted as size and relative light intensity (arbitrary units) plotted as a function of object concentration for the air NB sample and the NB-PSLB mixture sample.

Moreover, a peak with lower concentration at the size of 354 nm was also observed and marked on Fig. 6.3. Though the NTA measurement with PSLB suspension showed some minimal peaks of self-clustered PSLBs (Fig. 6.2), all of these peaks correspond to a size smaller than 300 nm. Hence the peak at a size of 354 nm must correspond to the clusters formed from the binding between NBs and PLSBs. The model of the clusters from multiple nanoparticles bound to a single NB is illustrated as Fig. 6.4.

And the size of this type of cluster can be approximated by the following:

$$d_{cluste} = d_{NB} + 2d_{PSLB} = 129nm + 2 \times 100nm = 329nm \tag{6.2}$$

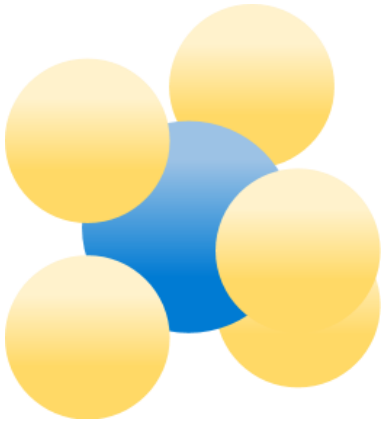

Figure 6.4: Models of a NB binding multiple PSLBs.
Yellow spheres represent PSLBs, and the blue sphere corresponds to a NB.

The peak at d = 354 nm is very close to this estimated cluster size and therefore supports the concept of NB binding the PSLBs and the formation of NB-PSLB clusters. Another possibility of the cluster model is that multiple NBs bound to one PSLB. However this model is impossible due to the energy barrier is too high between the NBs at the separation distance of approximately 100 nm. It will be discussed later. The mixture sample was also dried and examined using TEM. A cluster with an empty core was observed as in Fig. 6.5. The size and the structure of this cluster agreed with the estimation and further confirmed the binding interaction between NBs and PSLBs.

6.4 Theory

The finding above proved the clustering between NBs and PSLBs. Based on DLVO theory, vdW and electrostatic forces contribute to the interaction potential between a NB and a nanoparticle. The NBs are negatively charged that was revealed by the observed negative ζ potential in the present work as well as by others [65, 9]. When interacting with PSLBs which have slightly negatively charged surfaces, the contribution of the electrostatic force to the interaction potential is always repulsive.

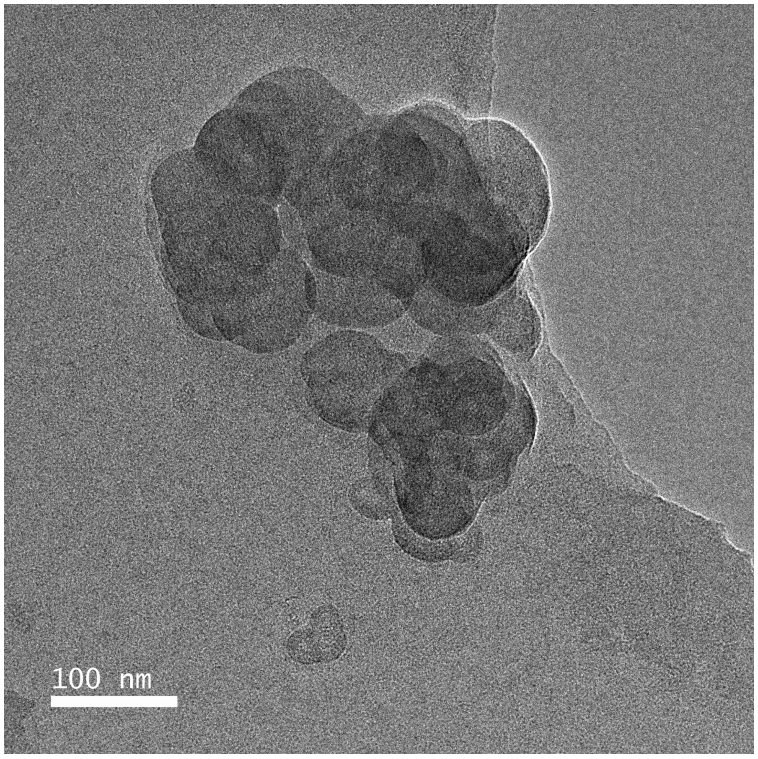

Figure 6.5: TEM image of a dried NB-PSLB cluster with an empty core on a 400M copper grid.

It was noticed that, in the application of DLVO theory, other non-DLVO forces such as hydration, structural, steric and solvation were always neglected [65]. However, when reviewing the reports by others, NBs can also interact with hydrophobic or amphiphilic substances [12, 13, 14, 60]. Moreover, within the gas-liquid interface of a NB is a region with lower dipole moment due to the existence of concentrated nonpolar gas molecules. Hence, hydrophobic nanoparticles tend to situate within this region to reduce their free energy. This tendency or attraction can be described as hydrophobic interaction, or hydrophobic force. Hydrophobic force was found to be exponentially correlated to the separation distance between the hydrophobic particles [91]. Therefore, the hydrophobic force should also implement in the study of the interaction potential between a NB and a nanoparticle as an extended DLVO (XDLVO) model.

Then the total interaction potential $W_{total}(D)$ from the XDLVO model can then be written

as:

$$W_{total}(D) = W_{vdW}(D) + W_{ES}(D) + W_{HI}(D) \tag{6.3}$$

where $W_{HI}(D)$ is the contribution of hydrophobic interaction force.

The contribution of van der Waals force $W_{vdW}(D)$ between a NB and a PSLB can be written as [66]:

$$W_{vdW}(D) = -\frac{AR_{NB}R_{PSLB}}{6D(R_{NB} + R_{PSLB})} \tag{6.4}$$

where R is the corresponding radius of the nano-object, and A is the Hamaker constant. The Hamaker constant for a system that consists of a NB with a dielectric constant or permittivity ε_1, a PSLB with ε_2 and the medium of water with ε_3 can be estimated based on Lifshitz theory which is given by:

$$A = \frac{3}{4}k_BT(\frac{\varepsilon_1 - \varepsilon_3}{\varepsilon_1 + \varepsilon_3})(\frac{\varepsilon_2 - \varepsilon_3}{\varepsilon_2 + \varepsilon_3}) + \frac{3h}{4\pi}\int_{v_1}^{\infty}(\frac{\varepsilon_1(iv) - \varepsilon_3(iv)}{\varepsilon_1(iv) + \varepsilon_3(iv)})(\frac{\varepsilon_2(iv) - \varepsilon_3(iv)}{\varepsilon_2(iv) + \varepsilon_3(iv)})\,dv \tag{6.5}$$

where $\varepsilon(iv)$ are the values of ε at imaginary frequencies, v_1=3.9×10^{13} s^{-1} at 298 K [92], k_B is the Boltzmann constant, h is the Planck constant and T is absolute temperature. The dielectric constant $\varepsilon(iv)$ is expressed by:

$$\varepsilon(iv) = 1 + \frac{n^2 - 1}{1 + \frac{v^2}{{v_0}^2}} \tag{6.6}$$

where n represents the refractive index of the medium; v_0 is the main absorption frequency of the medium. The parameters used for the calculations are listed in Table 6.1.

Table 6.1: Parameters used in Eqns. 6.5 and 6.6, T=298 K [71, 92, 93]

	NB	PSLB	water
ε	1.0006	2.52	80.4
n	1.26	1.59	1.33
$v_0(s^{-1})$	6×10^{14}	1.5×10^{15}	3×10^{15}

The Hamaker constant A for the system of one air NB and one PSLB in water was then calculated as 1.6×10^{-21}J.

The contribution of electrostatic force $W_{ES}(D)$ from the electric double layer can be estimated as [72]:

$$W_{ES}(D) = \frac{R_1 R_2}{(R_1 + R_2 + D)} Z\exp(-\frac{D}{\lambda_D}) \tag{6.7}$$

The interaction constant Z and Debye length λ_D are given by the following expressions:

$$Z = 64\pi\varepsilon\varepsilon_0(\frac{k_B T}{e})^2 \cdot tanh(\frac{ze\psi_{NB}}{4k_B T}) \cdot tanh(\frac{ze\psi_{PSLB}}{4k_B T}) \tag{6.8}$$

$$\lambda_D = \sqrt{\frac{\varepsilon\varepsilon_0 k_B T}{2ne^2}} \tag{6.9}$$

where ε is the dielectric constant of water, ε_0 is the permittivity of vacuum, e is electron charge, z is the charge number, n is ion concentration (ionic strength) and ψ is the surface potential of a NB or a PSLB, that was estimated with the measured ζ potential. The ion concentration n= 2.1×10^{22} m^{-3} was determined by the conversion of electrical conductivity measured in the ZetaSizer Nano ZS, as well as the measured ζ potentials of -20.0 mV and -2.4 mV for the NB and PSLB suspensions, respectively. In a system with pure water, the Debye length is approximately 980 nm [36]. However in this given system, a small amount of KCl in the original PSLB suspension that was used to maintain the colloidal stability increased the ion concentration and reduced the Debye length to 52.2 nm in the final NB-PSLB mixture suspension according to Eqn. 6.9.

The concept of hydrophobic force law was proposed by Israelachvili in 1982 after discovering that the attractive force between two hydrophobic objects in water is suprisingly long ranged, can go up to around 100 nm, and decays exponentially with separation distance [91]. Based on a further study by Donaldson, who was a researcher in Israelachvili's group, the energy potential contributed by hydrophobic interaction between two spherical nano-objects can be

expressed by [91, 94]:

$$W_{HI}(D) = -2\pi(\frac{R_1 R_2}{R_1 + R_2}) \cdot D_H \cdot (\frac{\gamma_1 + \gamma_2}{2}) \cdot H_y \cdot e^{-\frac{D}{D_H}} \tag{6.10}$$

Where γ is the surface tension, D_H is the decay length of hydrophobic force, and the Hydra parameter $H_y \equiv 1 - \frac{a_0}{a}$,where a_0 is the hydrophilic area and a is the hydrophobic area at a given interface. In the present model, γ_{NB} is 72 mJ/m^2 and γ_{PSLB} is 34 mJ/m^2 [92]. Because a NB is naturally super hydrophobic and polystyrene also has a contact angle over 90 ° [95], the hydra parameter was set as 1 to represent that the surfaces of NBs and PSLBs are completely hydrophobic. The decay length of hydrophobic force in this system is unkown and needs to be fitted. It has also been noticed that in the model made by Donaldson and Israelachvili [94], the authors mentioned a range of 0.3 - 1.7 nm of the decay length for two hydrophobic flat surfaces. However, there are also works showed a long-range attraction decaying with the power law over 100 nm that must have a decay length well beyond this range [96, 97, 98]. Rabinovich and Derjaguin found the interaction force of hydrophobized filaments decays with a D_H=12.2 ± 1 nm [96]. And in a recent report, a numerical work showed that a decay length can even go up to 25 nm in the hydrophobic interaction between an air macrobubble and coal particles [99]. Therefore, in the calculation of the energy barrier in $W_{total}(D)$, the contribution of hydrophobic interaction was calculated with D_H from 1 - 20 nm.

First we applied the traditional DLVO theory that only counts the contributions of vdW and electrostatic forces to our system, the interaction potential of this system is as in Fig. 6.6, an energy barrier of more than 2 k_BT can be seen. This energy barrier in the interaction potential predicted that a NB is not able to bind with a PSLB, however it contradicts with the experimental observation with the use of NTA and TEM. As a result, the contribution of hydrophobic interaction must be involved.

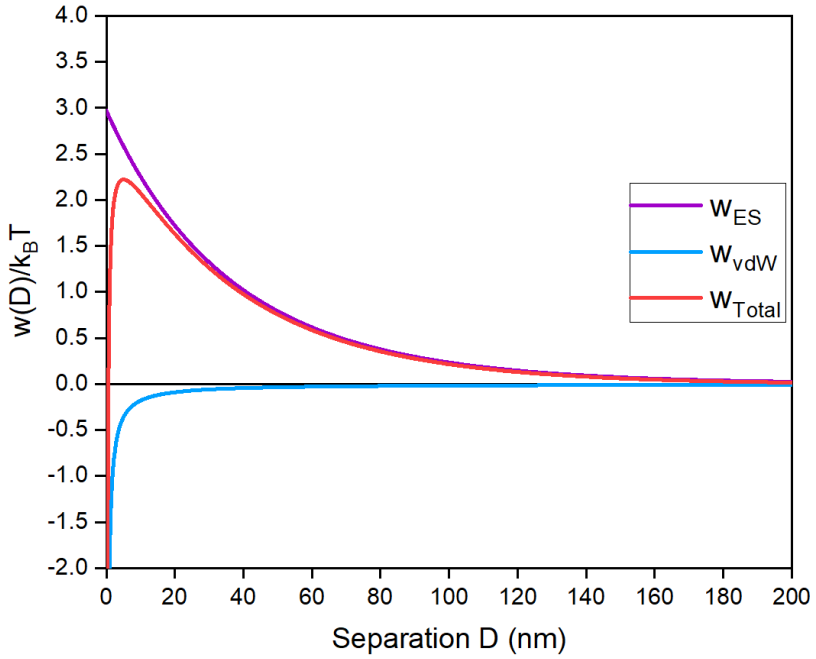

Figure 6.6: The interaction potential profile between a NB and a PSLB with traditional DLVO theory that only counts the contributions from vdW and electrostatic force.

The energy barrier of the total energy potential with different decay length in the hydrophobic interaction are presented in Fig. 6.7. Because the average thermal kinetic energy of nano-objects is on the order of 1 k_BT, the predicted energy barrier lower than 0.1 k_BT is negligible. Also in Li's report [92], an energy barrier of about 0.1 k_BT is able to completely prohibit the binding interaction between nano-objects hence we used this threshold as the criteria to find the fitting D_H. In 6.7 (A), only when $D_H \geq 9$ nm, the energy barrier is lower than 0.1 k_BT and when $D_H \geq 13$ nm, the energy barrier doesn't exist. The tendency of the decay in energy barrier decays with increasing D_H revealed that the D_H in this given system must be equal to or greater than 9 nm and only under this condition, the interaction potential agrees with the experimental observations and we used $D_H = 9$ nm in the following calculations to avoid overestimation. In 6.7 (B), the total interaction potential as well as the three components were plotted. One can see that in a NB-PSLB system, the hydrophobic attraction is much stronger than the vdW force and can compensate the repulsion from the electrostatic force. The effective range at around 120 nm also matches with the observations made by others

[96, 97, 98, 99].

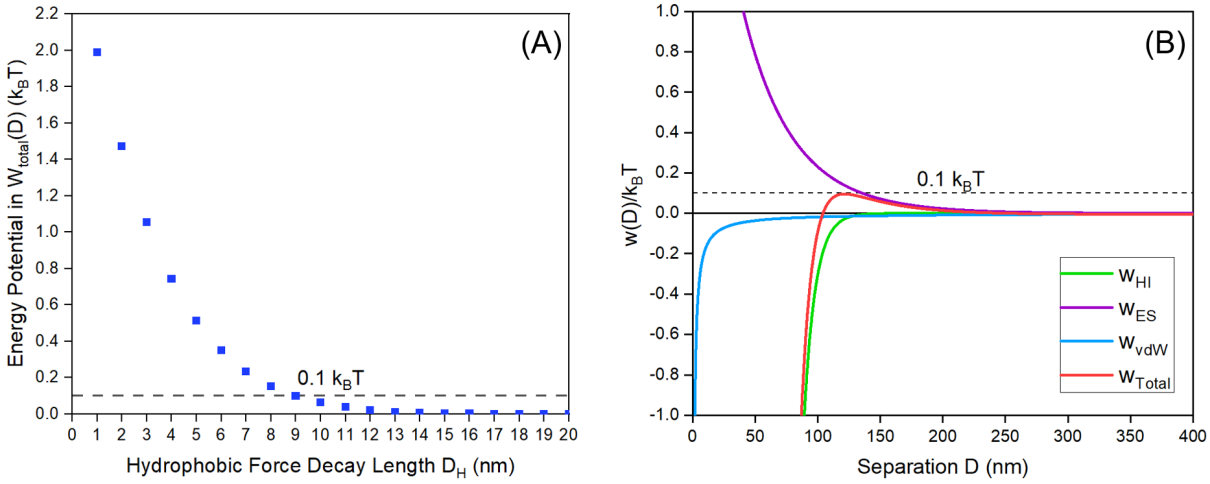

Figure 6.7: (A) The energy barrier's dependence on the fitted D_H in $W_{total}(D)$; (B) Interaction potential between a NB and a PSLB when $D_H = 9$ nm.
The horizontal dash line at 0.1 k_BT corresponds to the binding threshold reported in [92].

Moreover, similar to the decay length in electric double layer interaction, as known as Debye length, which indicated the screening effect in the electrostatic force in liquid system, the decay length in hydrophobic interaction also corresponds to a similar screening effect caused by the fact that the water molecules' polarization offsets the influence of the gas-liquid interface. It was also reported that dissolved air increased the effective range of hydrophobic force [100]. Considering that the nonpolar gas molecules inside and surrounding the NBs may lead to an even longer ranged hydrophobic interaction than solids due to a gas molecule's high mobility, the screening effect from the surrounding area of a NB should be weaker than around a solid surface. Hence, the fitting of a decay length D_H higher than 9 nm in the model is therefore reasonable, plausibly, it can go up to 20 nm.

The interaction potential between two NBs and two PSLBs in this given solution condition were plotted in Fig. 6.8 with the NB-PSLB interaction with a D_H= 9 nm for reference. The decay length of the hydrophobic interaction potential between two NBs is 9 nm which is the same as the fitting for a NB-PSLB system. The D_H used for the two PSLBs is 0.75 nm

[101] which indicates a shorter-ranged hydrophobic interaction between PSLBs. The energy barriers in the NB-NB and PSLB-PSLB interactions are 1.03 and 0.04 k_BT, respectively. With an energy barrier higher than the threshold at 0.1 k_BT, the total interaction between two NBs can prevent them from getting closer than approximately 150 nm therefore in this given system they are stable from coalescence. This high energy barrier also prohibit the formation of clusters comprised of one PLSB binding multiple NBs. Because the size of the PSLB is 100 nm, after a NB bound a PSLB, the NB would repulse the other NBs which were getting closer. The energy barrier between two PSLBs is much lower than the threshold which indicates that a self clustering can occur spontaneously. Nevertheless, the effective range of the interaction between two PSLBs is lower than 20 nm which is much lower than the effective range in the NB-PSLB interaction of around 120 nm. The extremely small effective region implies that the probability of two PSLBs interacting with each other is much lower than a NB binds a PSLB, which can also occur spontaneously. Moreover, in the NTA result, the size of the measured clusters of 358 nm also fits better with the model in Fig. 6.4 rather than the clusters with a similar configuration but only made up by PSLBs, which should have a diameter of around 300 nm. Meanwhile, the dried shell-with-an-empty-core structure observed in the TEM image (Fig. 6.5) also matches with the model. Because it indicates that after the capture by a NB, the nearby PSLBs can bind each other due to a low energy barrier and form a shell-like structure. This cluster morphology is extraordinary stable and can even survive after the solution drying.

According to the NTA result, one can see that not all the NBs and PSLBs clustered with each other as the concentration of NBs and PSLBs is still much higher than that for the clusters in Fig. 6.3. This result can be explained by the fact that the total concentration in the suspension is about 5×10^7 mL^{-1}, which gives to a mean separation between the nano-objects of approximately 27 μm. And as indicated in Fig. 6.7(B), only when the two nanoparticles reach to each other with a distance of about 120 nm, the attractive interaction between them becomes effective and leads to a binding. However, the movement of the nano-

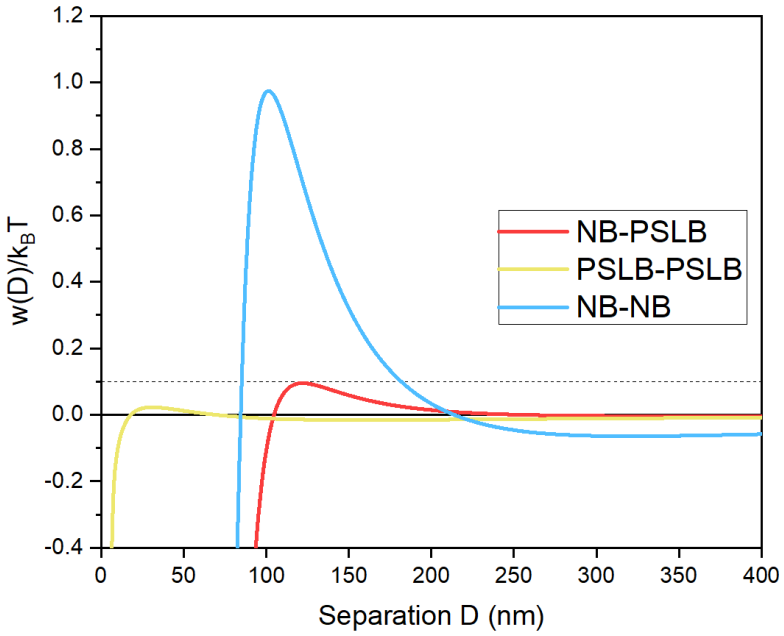

Figure 6.8: $W_{total}(D)$ between (Red) a NB and a PSLB; (Yellow) two PSLBs; (Blue) two NBs.

objects is defined by Brownian motion and it is random with the absence of external force, which means a complete NB-PSLB clustering in the bulk suspension needs a very dense suspension which means an extremely high NB concentration, on the order of about 10^{13} to 10^{14} mL^{-1}, that was rarely reported except in [33]. Meanwhile, the large distance between the nano-objects in this given system further confirmed that the PSLB's self clustering is even more rare with an effective range of only 20 nm.

The present model has also been used with a generated NB suspension in pure water to investigate their stability. The calculated Hamaker constant A=$2.39\times10^{-20}J$ which is lower than $3.68\times10^{-20}J$ reported by Nirmalkar that is [65] because a NB refractive index of 1.26 that was observed by Bunkin [71] instead, rather tha 1.00 for air. The decay length of 9 nm in the hydrophobic force was used in this model. The interaction potential profile is presented in Fig. 6.9 with and without the hydrophobic force contribution for DLVO and XDLVO model, respectively.

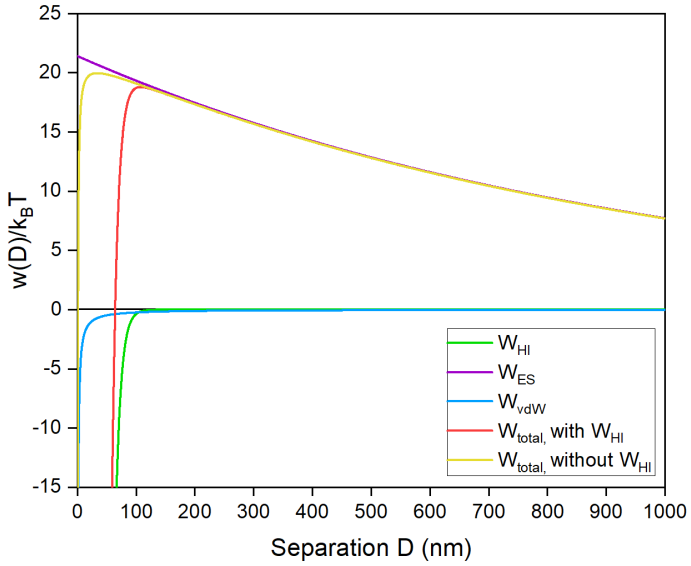

Figure 6.9: The interaction potentials between two NBs including the energy barriers predicted by traditional DLVO and XDLVO theories.

In this plot, a high energy barrier at around 19 k_BT was observed in the total interaction potential curve with the contribution of hydrophobic attraction. The calculated energy potential is lower than the one predicted by Nirmalkar and colleagues who used the traditional DLVO theory and different parameters such as Hamaker constant[65]. But both indicated that two NBs repel each other in the suspension and will not bind or coalesce. Owing to the negatively charged surface of NBs, the strong electrostatic repulsion governs in the interaction between NBs and strengthened their stability. This repulsion could be partially responsible for their extraordinary size stability and observed longevity. When applying traditional DLVO in the case of NBs, compared to the electrostatic, the hydrophobic attraction is too weak to be effective. Hence the traditional DLVO theory can also predict a high energy barrier, at around 20 k_BT which also indicated an outstanding stability of NBs, though the barrier was overestimated by about 5%.

6.5 Conclusion

The present NTA measurements of the NB-PSLB mixture suggested cluster formation as a result of NB binding nanoparticles. Moreover, the TEM image of a dried PSLB cluster with an empty core further confirmed that a NB is able to capture a nearly electroneutral or slightly negatively charged nanoparticle. By applying the traditional DLVO theory to this given NB-PSLB system, however, the theoretical estimation contradicted the experimental results. Hence, another non-DLVO force, the hydrophobic force potential, must be implemented to extend DLVO theory, as the XDLVO theory. Referring to the experimental results, it was also found that the hydrophobic force must involve in the process of NB binding nanoparticles and a decay length of at least 9 nm for the hydrophobic force in given system was revealed. This XDLVO model doesn't only confirmed the role of hydrophobic force in the interaction between nano-objects, but also provides a better method to predict the binding/clustering interaction between NBs and other nanoparticles.

Applying the present XDLVO theory with NBs in pure water with the hydrophobic force leads to a high energy barrier of 19 k_BT consistent with the repulsion between the NBs which prevents the coalescence of NBs. Due to a low electrical screening effect in the pure water, this electrostatic repulsion governs the interaction potential and strengthens the NB size stability in the present system.

Chapter 7

Nanobubble Generation by an Alternating Magnetic Field with Different Gas Species

This chapter further studies the AMF NB generation by pretreating the water with different different gas species. To have a better understanding of the NB generation mechanism, experiments were conducted to study the gas solubility's effect on the NB generation efficiency and the generated NB's properties.

7.1 Materials and Method

A close-loop test system (CLTS2) as in Fig.7.1, had a treatment capacity of 1.4L of water and the flow rate was approximately 5.3 L/min. The overall size of CLTS2 is smaller than CLTS1 as described in Chapter 3 to achieve a better gas tightness. The glass flask used as the water reservoir can be sealed with a rubber stopper with drilled holes that allows the

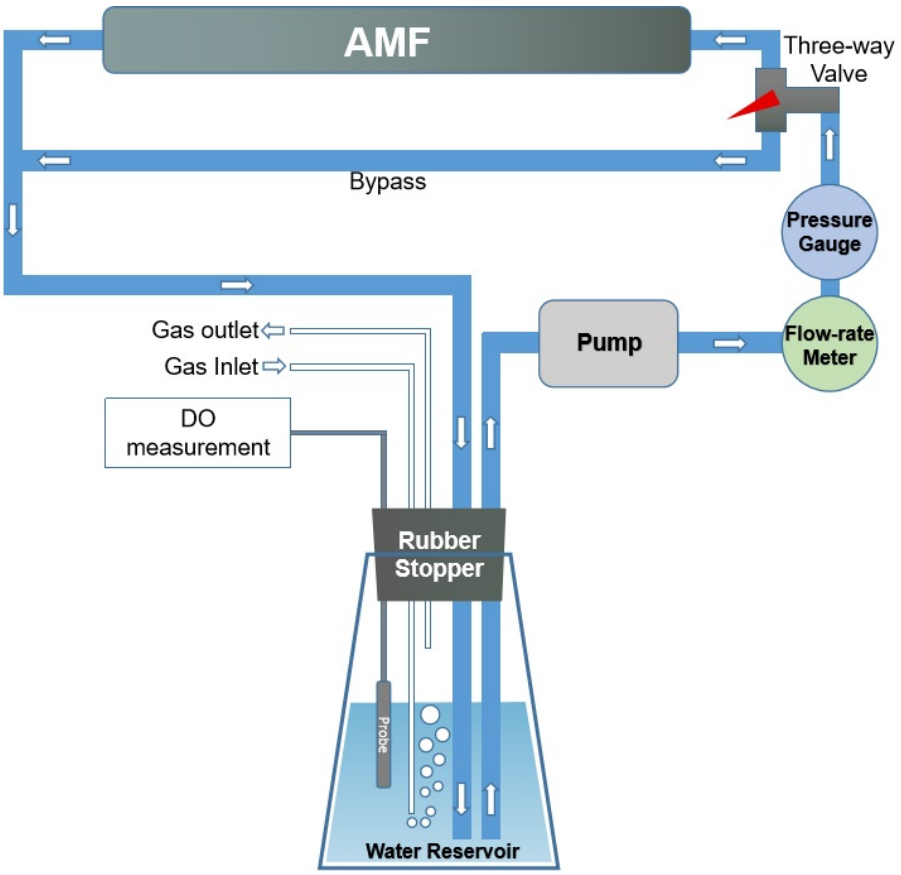

Figure 7.1: Schematic of the smaller closed-loop test system, CLTS2.

connection of tubings and dissolved oxygen (DO) probe. During a treatment, the system was sealed but with a gas outlet connected to a flask with an anti-backflow-of-gas design as in Fig. 7.2. The gas pressure difference between the CLTS2 reservoir and the atmosphere came from the water above the gas inlet in the connected flask to stop the backflow of the gas as shown in Fig. 7.2. The estimated pressure difference is 0.02 atm with an underwater depth of 2 cm and it is negligible hence the gas pressure over the water in the water reservoir during the treatment was close to 1 atm with this present setup.

Three types of gas, oxygen (Praxair, Inc. US), nitrogen and helium (Airgas, Inc. US), that were with the purity over 99.99% and supplied through the gas inlet were used to pretreat the water to reach a 100% gas partial pressure at 1 atm by gas bubbling. Gas bubbling is an efficient method to purge the air already dissolved in the water and the bubbling has a larger

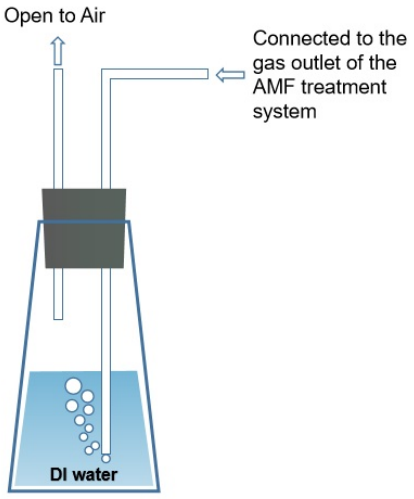

Figure 7.2: Schematic of the flask connected to the gas outlet of CLTS2 with an anti-backflow-of-gas design.

contact area that allows a higher diffusion and exchange rate. The gas inlet has a nozzle with a diameter of nearly 2 mm. When bubbling, the bubbles' diameter was in the range of several millimeters and won't lead to the formation of NBs [36]. The dissolved oxygen (DO) was measured by a DO meter (Shenzhen Yage Technology, Ltd. China) and the electrodes of the probe were placed underneath the water level in the CLTS2 reservoir.

The pretreatment with oxygen bubbling led to a DO over 40 mg/L at room temperature which indicated the saturation as in table 7.1. The saturation of nitrogen and helium gas were also determined by the DO meter as the pretreatments were recognized as completed with a DO read of 0 mg/L of because only when the partial pressure of the nitrogen or helium is at 1 atm, there is no dissolved oxygen in the water. During the pretreatment, the gas flow rate was not precisely controlled but the saturation can always be achieved within 15 minutes for all the three gas species. The water sample after the pretreatment with the three gasses were examined with NTA and the results showed no existence of nano-objects. During the water treatment, the gas flow rate was controlled at 20 SCCM.

Table 7.1: Gas solubility with the partial pressure at 1 atm above the water at 20 °C [102, 103]

Gas Type	O_2	N_2	He
Solubility (mg/L)	43	19	1.5

7.2 Results and Discussion

The size distribution and integrated concentration measured by NTA with a NanoSight NS300 of the water samples collected right after the treatments in CLTS2 under the conditions of 1 atm of Nitrogen, Oxygen and Helium, with and without the exposure to AMF, were presented in Fig. 7.3 and 7.4.

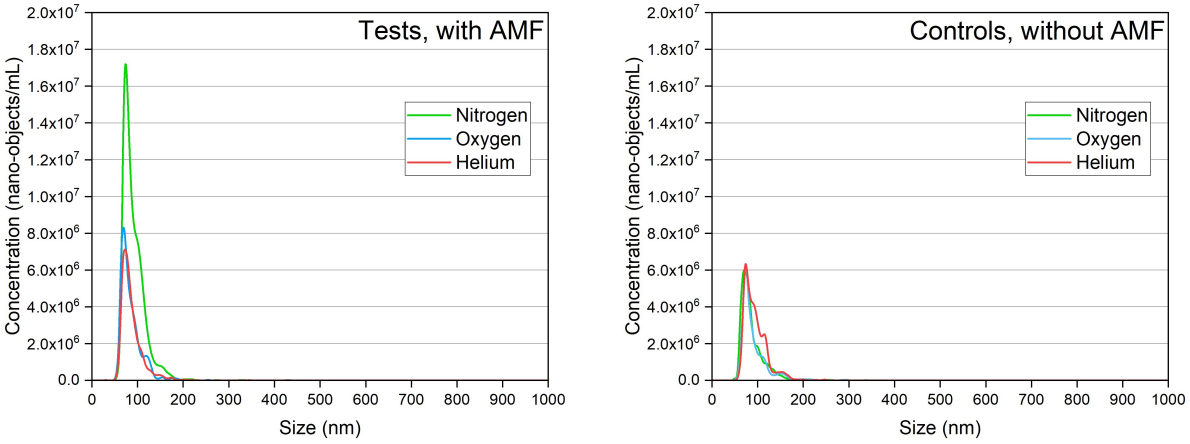

Figure 7.3: Size distribution of Nano-objects in the treated water samples in CLTS2.

In the results, the existence of nano-objects can also be seen in the controls, however the concentrations are lower than in the treatments under 1 atm of nitrogen and oxygen. In Fig. 7.3, the controls that weren't exposed to AMF showed similar size distribution. And in

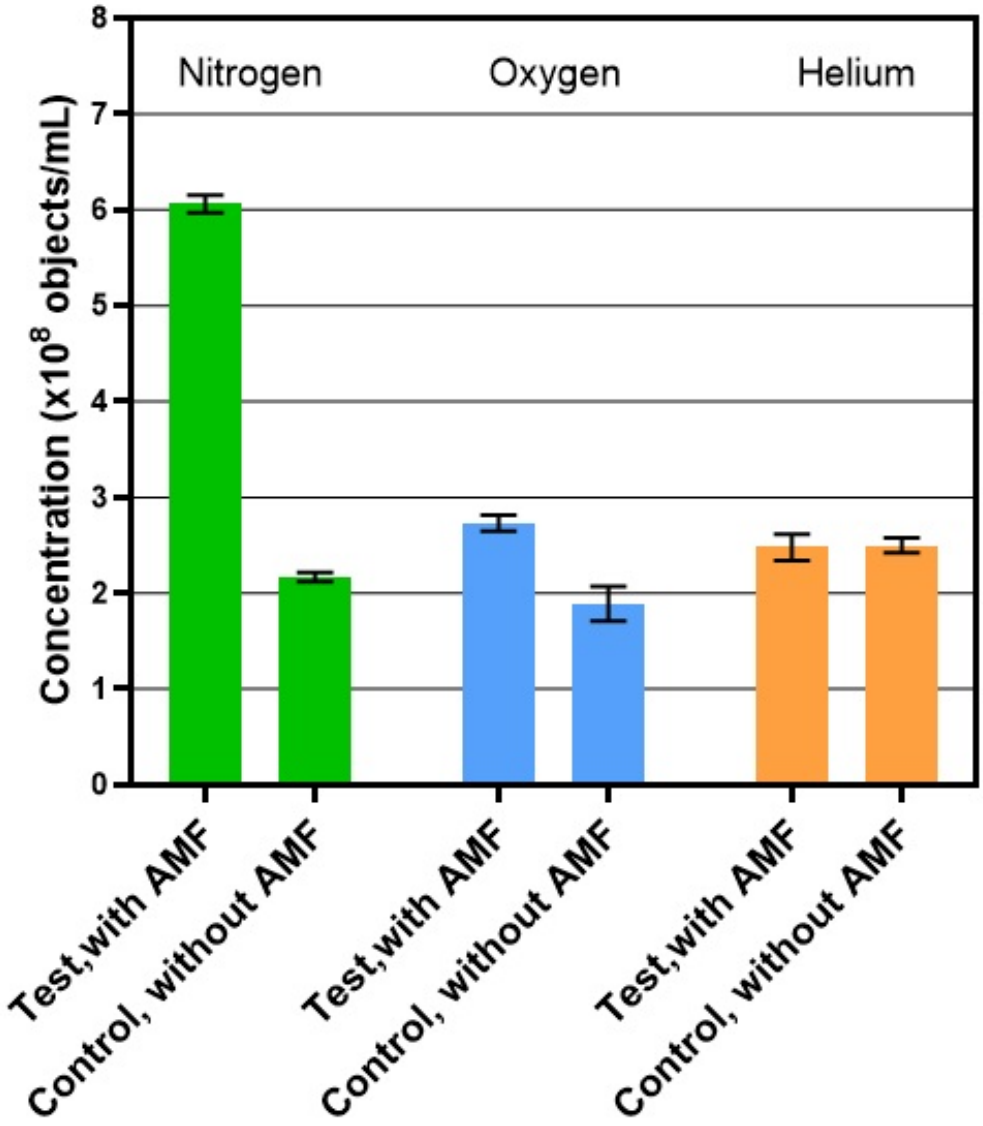

Figure 7.4: Integrated concentration of Nano-objects in the treated water samples in CLTS2.

Fig. 7.4 from the observed nano-objects concentrations with the 1 atm of helium condition, there was no significant difference between the test and the control. It can be concluded that pumping water can also generate NBs, especially when the partial pressure is high for a single gas. This assertion is reasonable as the pump in the water circulation system applies strong shear force and leads to a turbulent flow condition with high local pressure within the pumping area. During the treatment, this pressure forced the dissolution of gas in the water.

Once the pressure was alleviated after the pumping area (e.g. near the AMF unit or in the water reservoir that has a gas pressure at 1 atm), the gas precipitated out from the water and a portion of the gas was stabilized in the form of NB. This mechanism is also the proposed principle for the NB generation methods of mixing gas&liquid and pressure changes. [9, 39, 40, 41, 45]. According to Henry's law, the pressurization's effect as described is more sensitive when the partial pressure of a gas is as high as 100%. By comparing the three controls, one can see that the order of NB concentrations in the three AMF treated water sample is He $>N_2 >O_2$ and it is in the reserve order of the solubility of the three gas species as in table 7.1. Because with lower solubility, the effect of pressurization on gas dissolution is also more significant, hence it also agrees with that the pumping pressurization with the same power input can generate more NBs with the gas that has lower solubility. Though the overall concentration differences between the three samples are small, it implied the dependence of gas solubility in NB generation method of water-gas mixing with pressurization and supersaturation.

Moreover, because Helium has extremely low solubility in water as in table. 7.1, no difference in the observed concentration from the water sample treated under 1 atm of helium indicated that the AMF only affects the dissolved gas molecules rather than the ones in the gas phase. And it is consistent with the hypothesis that AMF disturbs the interaction between gas and water molecules in a gas solution, and leads to the generation of NBs.

Based on this conjecture, the nano-objects observed in the controls from the three gas types and part of the tests were NBs generated by the water pumping and the exceeding portion in the samples treated with 1 atm of nitrogen and oxygen was generated by AMF. It is further confirmed by the difference of the concentration difference between the water samples treated with 1 atm of nitrogen and oxygen. Because nitrogen has lower solubility than oxygen, it indicates that the intermolecular force between nitrogen and water molecules is weaker than the one between oxygen and water. With the same AMF condition, the interaction between

nitrogen and water molecules is easier to be disrupted and results in the higher concentration of generated NB. By comparing the three tests, one can conclude that AMF has a better NB generation performance on the gas species with a moderate solubility and the influence of gas solubility has been described diagrammatically in Fig. 7.5.

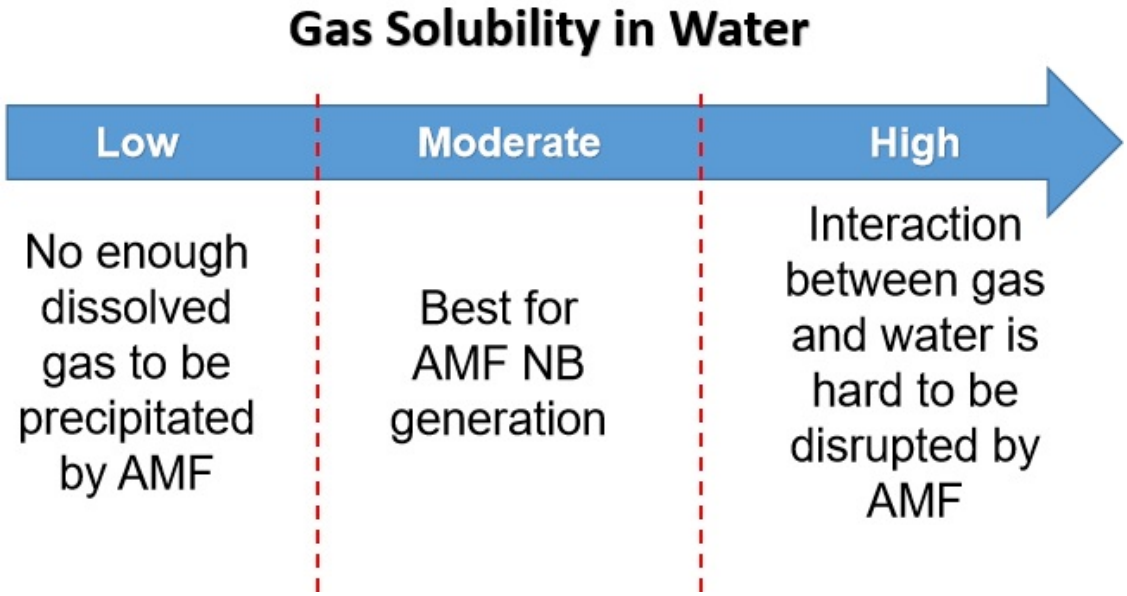

Figure 7.5: Effect of gas solubility on AMF NB generation summarized from the experimental results.

The freezing-thawing experiments with the three test samples that were exposed to AMF were performed and the NTA results were presented in Fig. 7.6. The concentration of the nano-objects in the fresh samples was also included for comparison. The results are consistent with the results from Jadhav and Barigou, Nirmalkar and coworkers [9, 65] that applied the same process to the NB suspension and only few nano-objects can be observed by NTA after the freezing and thawing. Hence, the nano-objects that were no longer present must have been NBs rather than solid particles or droplets. However, whether the NBs vanished during freezing or thawing is unknown. The crystallization of water may lead to the rupture of the nanobubble due to the expansion of ice formation [9]. This experimental result further confirmed that the AMF treatment generates NBs in DI water.

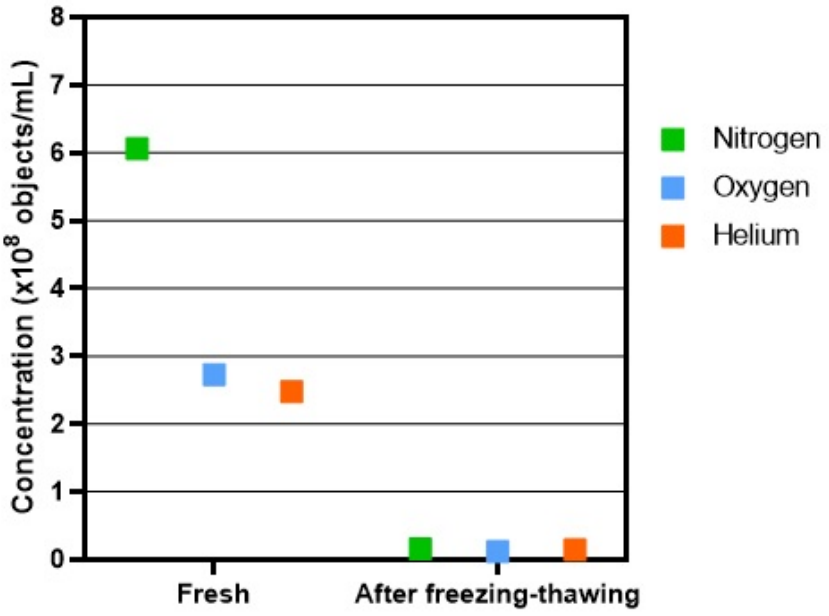

Figure 7.6: Integrated concentration of NB suspensions generated under 1 atm of nitrogen, oxygen and helium before (fresh) and after freezing-thawing.

From the above experimental results, it can be concluded that the NBs generated by AMF under 1 atm of nitrogen, oxygen and helium are made up of the corresponding gas because the gas supplied via bubbling is the only gas available to generate NBs.

NTA and ζ potential measurement have also been performed on the water samples with the AMF generated NBs of different gas species after several days. The collected NB suspension samples were kept in a glass vial at room temperature and the gas above the water level was air. These results are presented in Fig. 7.7 and 7.8. One can see a gradual drop in concentration of all the three types of NBs with time in the NTA result of the NB concentration. This observation matches with the report from others that the NBs are stable for several days [65]. This gradual reduction indicated the metastable property of the NB stability. With similar initial concentration, helium NBs dissipated faster than the oxygen NBs. It can be explained by the low solubility of helium and low partial pressure of helium in the air that lead to the faster disappearance of the helium NBs.

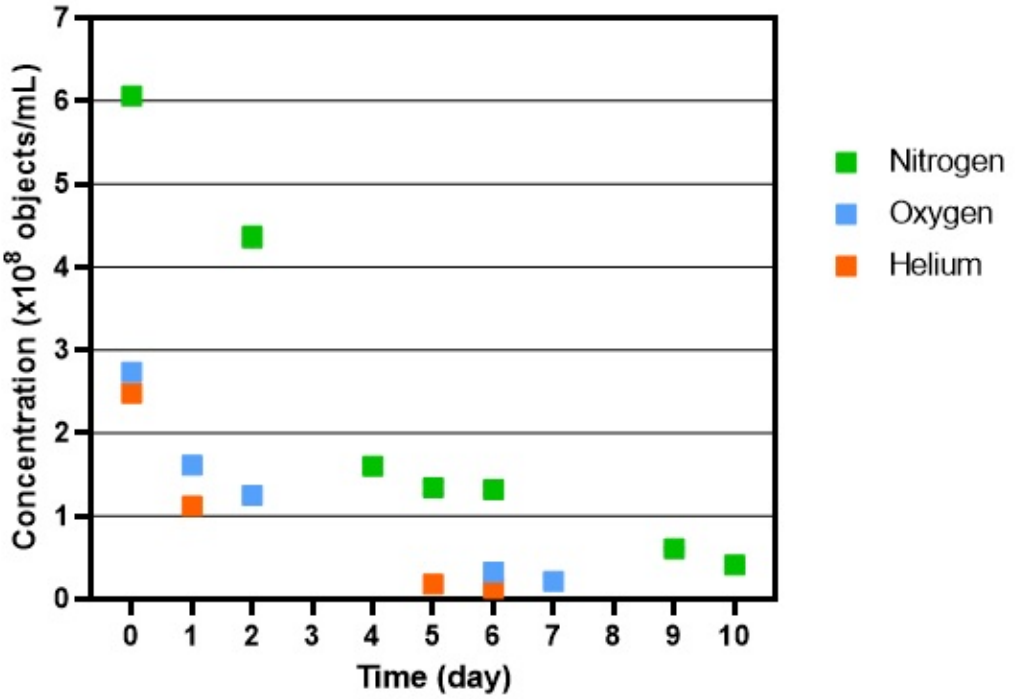

Figure 7.7: Integrated concentration of the water samples measured by NTA, after the generation of nitrogen, oxygen and helium NBs.

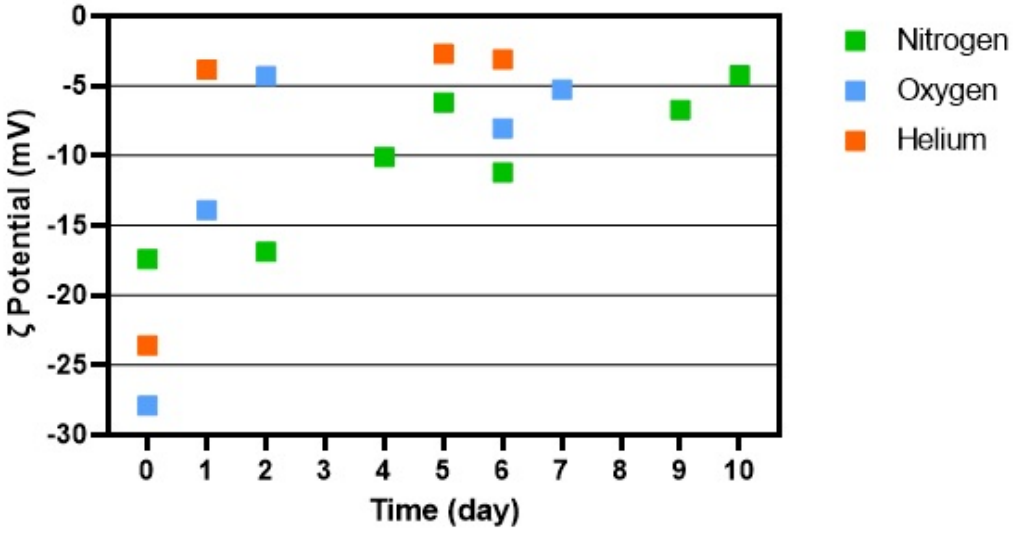

Figure 7.8: ζ potential of the water samples after the generation of nitrogen, oxygen and helium NBs.

The ζ potential has a negative correlation with the concentration of NBs. In the theory of NB stabilization, hydroxide ions are needed to compensate for the extremely strong surface tension on the gas-liquid interface [36] and this is also the cause of negative ζ potential. As the NBs in the solution became less stable over the time that was indicated by the lowering concentration, the charge carriers were also lessened and in pure water, the only anion is hydroxide ion. The lower negative ζ potential after several days of storage implied that the NBs' stability was compromised. The possible cause can be that the gas diffused back to the liquid phase with a weakened diffusive shielding effect with time [38].

It was also noticed that in Ushikubo's report [30], the freshly made O_2 and N_2 NBs have the ζ potential at approximately -40 mV and -30 mV, respectively, whereas the measured O_2 and N_2 NBs generated in CLTS2 have the ζ potential at -27.9 mV and -17.4 mV, respectively. Though the authors didn't provide the parameters used for ζ potential measurement and the NB concentration for further comparison, the difference between the ζ potential of the two gas types showed a same difference of 10 mV. To some degree, it supported the assertion that the AMF did generate NBs with dissolved gas.

The XDLVO interaction potentials calculated using the NTA and ζ potential measurements and the equations in Chapter 6 are plotted in Fig. 7.9. The initial potential barrier ranged from 6 to 15 k_BT is high enough to inhibit the coalescence of NBs. The gradual decrease of potential barriers from the three types of NBs indicates that the repulsion between NBs decays with time and when the barrier drops to a low level ($< 0.1\ k_BT$), the coalescence between NBs occurs and leads to the instability of NBs.

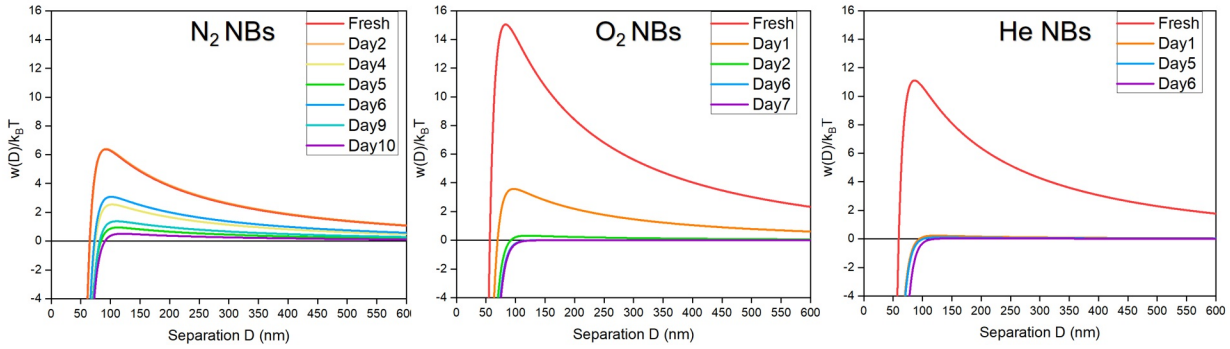

Figure 7.9: XDLVO interaction potentials between NBs, after the generation of nitrogen, oxygen and helium NBs.

7.3 Conclusion

The experiments of using AMF to generate NBs with different gas species further confirmed that a AMF water treatment introduced NBs in the water. The concentration and size distribution of NBs in the control solutions that were pretreated with the three gas species but not exposed to the AMF unit were numerically close to each other. Those NBs must be from the pump pressurization processing that introduced the oversaturation of gas in water. The difference between the AMF treated and control solutions also indicated that the AMF NB generation has a better performance in the gas species with a higher solubility in water than the gas-water-mixing and oversaturation methods mentioned in Chapter 2.

It was found that AMF had little effect on helium by comparing the results with AMF NB generation under 1 atm of nitrogen, oxygen and helium. This result is likely because helium's solubility in water is extremely low and there is little dissolved He molecules. The difference of the generated NBs' concentration with N_2 and O_2 indicated the gas solubility on AMF NB generation. These findings support the assumption that AMF generates NBs by disturbing the interaction between the dissolved gas molecules and water molecules. In addition, the freezing-thawing test to the solution agrees with that the nano-objects observed in the AMF treated water must be NBs, rather than nanoparticles or droplets. And the negative correlation between NB concentration and ζ potential/XDLVO potential barriers

supports the contribution of hydroxide ions to the stability of NBs.

Chapter 8

Conclusion

This work was started with an observation that the service water treated by an alternating magnetic field (AMF) can dissolve much more mineral deposit than the regular water. Then we made a hypothesis that this promotion to the dissolution of insoluble compounds, e.g. $CaCO_3$, is because AMF can generate bulk nanobubbles (NBs) in the circulating water with dissolved gas, and the generated NBs promotes the dissolution.

In order to investigate the hypothesis, close-loop water test systems equipped with the AMF unit were built. In the test system CLTS1 with higher water capacity and flow rate, the water sample was circulated for 3 hours that counts more than 100 cycles. The measurement in the treated water showed a high negative ζ potential indicating the existence of negatively charged nano-objects in the water, which agrees with the NB's measured ζ potential generated with other methods. However, in the control sample that was also treated in the test system but without the exposure to the AMF unit showed no existence of charged nano-objects. The clustering effect of NBs with $CaCO_3$ was also investigated, specifically, the enhanced dissolution of $CaCO_3$ induced by NBs. the mechanism was proved that the NBs can bind nanoparticles to form clusters, and the decrease of the concentration of the

free suspending nanoparticles leads to the dissolution of insoluble compounds.

Experiments with the Ringer's solution containing AMF-generated NBs were performed, to study NBs' effect on the dissolution of *ex vivo* human plaque in coronary artery, peripheral artery and aortic valve tissue. By comparing the NTA results in the solution exposed to the human tissue for four hours, with and without the NBs, existence of two types of clusters was found in the sample with NBs, whereas there were none in the control sample without AMF NB generation. Intravascular optical coherence tomography (IVOCT) performed with *ex vivo* artery samples before and after the NB treatment showed a plaque volume reduction of 18%-40% for coronary artery and 68% for peripheral artery within four hours, while in the control test without NBs, the reduction rate was much lower. Micro computed tomography (Micro-CT) was applied in scanning the plaque in the *ex vivo* aortic valve tissue before and after the NB treatment. The plaque volume reduction rate in the sample treated with NBs is 6%. While in the control that was without NBs in the solution, the deduction rate was lower than 2%. Overall, all the experiments showed that the plaque dissolution was accelerated with the existence of NBs. Moreover, based on the experimental results and theory, the NB technology and AMF NB generation method was proved to have a great potential in developing new medical devices and a benefit to health and welfare.

The hydrophobic interaction between NBs and hydrophobic nanoparticles was investigated. The studied nanoparcticles are polystyrene latex beads (PSLBs) with a size of 100 nm. NTA measurement showed the existence of NB-PSLB clusters and the size agreed with the model of one NB bound several PSLBs onto its surface. A PSLB cluster with an empty core was also observed in the dried sample loaded on a copper grid by using transmission electron microscopy (TEM). The cluster size also matched the model. The DLVO theory was extended to be the XDLVO theory which counts the contribution of hydrophobic force, especially For a system with hydrophobic/electroneutral nanoparticles, because with a traditional DLVO theory that only counts vdW and electrostatic forces, a NB is not able to bind a 100 nm

PSLB. With the XDLVO theory, it was found that there must be a contribution from hydrophobic force which is decaying with the power law which has a decay length of more than 9 nm. It was also found that in the given system, the potential barrier between PSLBs is even lower but with a very small effective range. It is consistent with the observation from the TEM that the dried NB-PSLB cluster has a shield-like structure which was from the PSLB self-binding after clustered by a NB which has a longer effective range. This XDLVO theory can also be used to better predict the binding interaction or the stability in the colloidal systems, especially when the colloids are hydrophobic. By applying this model to the interaction potential between NBs, a high energy potential of 19 k_BT was observed and it predicts a stable colloidal system for NBs in pure water. This could be a further reason behind their extraordinary stability.

Lastly, the mechanism of the AMF NB generation was further studied. With the results in the AMF treatment with three different gas types, it was found that AMF had little effect on the water sample pretreated with helium by comparing the treated water with and without the exposure to an AMF unit during a 3 hour treatment. However, the performance of NB generation with water pretreated with nitrogen and oxygen showed a significant difference, while the treatment with nitrogen generated more NBs. Because dissolution of gas in water depends on the strength of the interaction between gas and water molecules, and a magnetic field was found to be able to affect this interaction, it was then concluded that AMF generates NBs by disrupting this interaction and leading to the precipitation of gas molecules. The nucleation of the gas phase in the water followed by the stabilization of hydroxide ions on the gas-liquid interface gave rise to the formation of stable NBs. AMF had little effect with water pretreated with He. Since He has extremely low solubility in water, it apears that AMF is only effective with significant amounts of dissolved gas. By comparing the NTA results from the test with N_2 and O_2, the observation of higher NB concentration with water pretreated by N_2 seems to be due to the lower solubility of N_2 which is easier to be affected by AMF as it has weaker interaction with water molecules. Furthermore, in the AMF treatment with

the smaller test system CLTS2, the water sample was pretreated with three types of pure gas, N_2, O_2 and He, under a partial pressure of 1 atm for each pretreatment. After the AMF treatment, the first test was freezing the water sample at -18 degreeC for more than 12 hours and thawing the frozen sample at room temperature. The nanoparticle tracking analysis (NTA) performed before and after the freezing-thawing process showed a significant concentration drop in the nano-objects. In the NB suspension generated by other methods, similar results were obtained. This observation strongly supported that the nano-objects suspended in the water must be NBs rather than solid nanoparticles or droplets, because only the NBs are defined by the gas-liquid interface and this interface is not able to survive from freezing and thawing of the water. By measuring the overall nano-objects number concentration decaying with time, the gradual disappearing of the nano-objects in the AMF treated water also indicated the existence of NBs, as they are in a metastable state. The above results proved that the AMF treatment introduced the generation of NBs.

Chapter 9

Future Work

Future work is suggested in the following:

1. There are still a lot of unknown aspects with respect to AMF NB generation, such as the parameters affecting the NB generation and a more detailed mechanism behind it. So far, we only know that, with dissolved air, higher flow rate leads to a higher NB concentration in the water and AMF has a higher NB generating efficiency with the gas type having a moderate solubility in water, e.g. N_2. However, the other water conditions for the generation system, the magnetic field, size and arrangement of the magnetic core may also affect NB generation. A simulation work in studying AMF's effect on the interaction between gas and water molecules is also suggested.

2. Develop a better method to use liquid phase transmission electron microscope (LP-TEM) to observe the NBs directly in liquid phase. Until now, there is still no direct observation of stable nanobubbles with a lifetime over several minutes, even though a lot of indirect evidence has indicated the existence of them. Several experiments in using LP-TEM with a silicon nitride liquid cell were performed with NB suspension by the authors. However, there is still no plausible conclusion to be drawn, as the acquired TEM images of NB suspensions showed

either spherical nanoparticles with high contrast or just nothing. The possible reasons for these observations could be: 1. The NBs' surface has an unexplained condensation effect, which drastically increases the mass density that leads to the abnormally high contrast in TEM; 2. The thickness of the liquid cell for around 2 μm is too large, and the water above and below the NBs screened the electron beam and made the NBs invisible. To better design the method, one can try to use graphene to build a liquid cell with relatively small height. But the height should not be too small because it will compress the NBs that may lead to NB coalescence or change bulk NBs to surface NBs. Similar work would be done with NB-nanoparticle clusters.

3. In the present work of studying NB's effect on the *ex vivo* dissolution of human plaque, only a limited quantity of available human samples were tested. For future work, one can test with more samples and further confirm the NBs' performance in promoting the dissolution of human plaque. More conditions like the NB concentration and treatment time can also be adjusted to compare.

4. The safety of applying NB treatment in clinical was not studied and needs more investigation. The present work only showed that NB can promote or accelerate the dissolution of plaque in *ex vivo* human tissues, whereas the cardiac system in a living human body is much more complicated. Though the NB treatment was proved to be a chemical free approach to treat atherosclerosis in coronary and peripheral arteries and calcific aortic valve disease, NB's ability to bind nanoparticles and the nature of NBs that are made of gas may lead to some unknown side effects. These potential side effects must be carefully investigated.

5. In the approach of estimating the hydrophobic force potential between a NB and a PSLB, we only found a lower limit of the decay length that is around 9 nm. Though the upper limit should be around 20 nm hence the range is not wide, a more exact decay length should be beneficial for a better prediction in some certain circumstances. Numerical methods such as simulations on the polarization surrounding a NB are recommended to find a more accurate

decay length and better understand the mechanism behind the NB-nanoparticle interaction and NB stability.

Bibliography

[1] James C. Earthman and William Dang. Alternating magnetic field treatment of service water to control pitting induced by sulphate reducing bacteria. *Corrosion Management*, 96:11–14, 2010.

[2] Emil Chibowski and Aleksandra Szcześ. Magnetic water treatment–a review of the latest approaches. *Chemosphere*, 203, 2018.

[3] H. E.Lundager Madsen. Influence of magnetic field on the precipitation of some inorganic salts. *Journal of Crystal Growth*, 152, 1995.

[4] A. D. Kney and S. A. Parsons. A spectrophotometer-based study of magnetic water treatment: Assessment of ionic vs. surface mechanisms. *Water Research*, 40, 2006.

[5] Jun Nakagawa, Noriyuki Hirota, Koichi Kitazawa, and Makoto Shoda. Magnetic field enhancement of water vaporization. *Journal of Applied Physics*, 86, 1999.

[6] Lucyna Holysz, Aleksandra Szczes, and Emil Chibowski. Effects of a static magnetic field on water and electrolyte solutions. *Journal of Colloid and Interface Science*, 316, 2007.

[7] Yun Zhu Guo, Da Chuan Yin, Hui Ling Cao, Jian Yu Shi, Chen Yan Zhang, Yong Ming Liu, Huan Huan Huang, Yue Liu, Yan Wang, Wei Hong Guo, Ai Rong Qian, and Peng Shang. Evaporation rate of water as a function of a magnetic field and field gradient. *International Journal of Molecular Sciences*, 13, 2012.

[8] Shaini Aluthgun Hewage, Jitendra Kewalramani, and Jay N. Meegoda. Stability of nanobubbles in different salts solutions. *Colloids and Surfaces A: Physicochemical and Engineering Aspects*, 609, 2021.

[9] Ananda J. Jadhav and Mostafa Barigou. Bulk nanobubbles or not nanobubbles: That is the question. *Langmuir*, 36, 2020.

[10] Tsutomu Uchida, Seiichi Oshita, Masayuki Ohmori, Takuo Tsuno, Koichi Soejima, Satoshi Shinozaki, Yasuhisa Take, and Koichi Mitsuda. Transmission electron microscopic observations of nanobubbles and their capture of impurities in wastewater. *Nanoscale Research Letters*, 6, 2011.

[11] George Z. Kyzas, George Bomis, Ramonna I. Kosheleva, Eleni K. Efthimiadou, Evangelos P. Favvas, Margaritis Kostoglou, and Athanasios C. Mitropoulos. Nanobubbles effect on heavy metal ions adsorption by activated carbon. *Chemical Engineering Journal*, 356, 2019.

[12] Weiguang Zhou, Jiaojiao Niu, Wei Xiao, and Leming Ou. Adsorption of bulk nanobubbles on the chemically surface-modified muscovite minerals. *Ultrasonics Sonochemistry*, 51, 2019.

[13] Minmin Zhang, James R.T. Seddon, and Serge G. Lemay. Nanoparticle–nanobubble interactions: Charge inversion and re-entrant condensation of amidine latex nanoparticles driven by bulk nanobubbles. *Journal of Colloid and Interface Science*, 538, 2019.

[14] Wanting Xiao, Guoren Xu, and Guibai Li. Effect of nanobubble application on performance and structural characteristics of microbial aggregates. *Science of the Total Environment*, 765, 2021.

[15] James W.G. Tyrrell and Phil Attard. Images of nanobubbles on hydrophobic surfaces and their interactions. *Physical Review Letters*, 87, 2001.

[16] Phil Attard. The stability of nanobubbles. *The European Physical Journal Special Topics*, 223:893–914, 4 2014.

[17] James R.T. Seddon, Detlef Lohse, William A. Ducker, and Vincent S.J. Craig. A deliberation on nanobubbles at surfaces and in bulk. *ChemPhysChem*, 13, 2012.

[18] Bram M. Borkent, Stephan M. Dammer, Holger Schönherr, G. Julius Vancso, and Detlef Lohse. Superstability of surface nanobubbles. *Physical Review Letters*, 98, 2007.

[19] Joost H. Weijs and Detlef Lohse. Why surface nanobubbles live for hours. *Physical Review Letters*, 110, 2013.

[20] Detlef Lohse and Xuehua Zhang. Surface nanobubbles and nanodroplets. *Reviews of Modern Physics*, 87, 2015.

[21] Shantanu Maheshwari, Martin Van Der Hoef, Xuehua Zhang, and Detlef Lohse. Stability of surface nanobubbles: A molecular dynamics study. *Langmuir*, 32, 2016.

[22] Lei Wang, Xingya Wang, Liansheng Wang, Jun Hu, Chun Lei Wang, Binyu Zhao, Xuehua Zhang, Renzhong Tai, Mengdong He, Liqun Chen, and Lijuan Zhang. Formation of surface nanobubbles on nanostructured substrates. *Nanoscale*, 9, 2017.

[23] Beng Hau Tan, Hongjie An, and Claus Dieter Ohl. Surface nanobubbles are stabilized by hydrophobic attraction. *Physical Review Letters*, 120, 2018.

[24] James R.T. Seddon, Harold J.W. Zandvliet, and Detlef Lohse. Knudsen gas provides nanobubble stability. *Physical Review Letters*, 107, 2011.

[25] Dongjin Seo, Sean R. German, Tony L. Mega, and William A. Ducker. Phase state of interfacial nanobubbles. *Journal of Physical Chemistry C*, 119, 2015.

[26] Muidh Alheshibri and Vincent S.J. Craig. Differentiating between nanoparticles and nanobubbles by evaluation of the compressibility and density of nanoparticles. *Journal of Physical Chemistry C*, 122, 2018.

[27] Ahmed Barhoum, M. Luisa García-Betancourt, Hubert Rahier, and Guy Van Assche. Physicochemical characterization of nanomaterials: Polymorph, composition, wettability, and thermal stability, 2018.

[28] Jingkun Jiang, Günter Oberdörster, and Pratim Biswas. Characterization of size, surface charge, and agglomeration state of nanoparticle dispersions for toxicological studies. *Journal of Nanoparticle Research*, 11, 2009.

[29] Fernanda Yumi Ushikubo, Takuro Furukawa, Ryou Nakagawa, Masatoshi Enari, Yoshio Makino, Yoshinori Kawagoe, Takeo Shiina, and Seiichi Oshita. Evidence of the existence and the stability of nano-bubbles in water. *Colloids and Surfaces A: Physicochemical and Engineering Aspects*, 361, 2010.

[30] Fernanda Yumi Ushikubo, Masatoshi Enari, Takuro Furukawa, Ryo Nakagawa, Yoshio Makino, Yoshinori Kawagoe, and Seiichi Oshita. Zeta-potential of micro- and/or nanobubbles in water produced by some kinds of gases. volume 3, 2010.

[31] Masayoshi Takahashi. ζ potential of microbubbles in aqueous solutions: Electrical properties of the gas - water interface. *Journal of Physical Chemistry B*, 109, 2005.

[32] Martina Roeselová, John Vieceli, Liem X. Dang, Bruce C. Garrett, and Douglas J. Tobias. Hydroxyl radical at the air-water interface. *Journal of the American Chemical Society*, 126, 2004.

[33] Kazunari Ohgaki, Nguyen Quoc Khanh, Yasuhiro Joden, Atsushi Tsuji, and Takaharu Nakagawa. Physicochemical approach to nanobubble solutions. *Chemical Engineering Science*, 65, 2010.

[34] Mitsuhiro MATSUMOTO. Surface tension and stability of a nanobubble in water: Molecular simulation. *Journal of Fluid Science and Technology*, 3, 2008.

[35] Tsutomu Uchida, Shu Liu, Masatoshi Enari, Seiichi Oshita, Kenji Yamazaki, and Kazutoshi Gohara. Effect of nacl on the lifetime of micro- and nanobubbles. *Nanomaterials*, 6, 2016.

[36] Pratik A. Satpute and James C. Earthman. Hydroxyl ion stabilization of bulk nanobubbles resulting from microbubble shrinkage. *Journal of Colloid and Interface Science*, 584, 2021.

[37] Jay N. Meegoda, Shaini Aluthgun Hewage, and Janitha H. Batagoda. Application of the diffused double layer theory to nanobubbles. *Langmuir*, 35, 2019.

[38] Joost H. Weijs, James R.T. Seddon, and Detlef Lohse. Diffusive shielding stabilizes bulk nanobubble clusters. *ChemPhysChem*, 13, 2012.

[39] William B. Zimmerman, Václav Tesař, and H. C.Hemaka Bandulasena. Towards energy efficient nanobubble generation with fluidic oscillation. *Current Opinion in Colloid and Interface Science*, 16, 2011.

[40] H. Oliveira, A. Azevedo, and J. Rubio. Nanobubbles generation in a high-rate hydrodynamic cavitation tube. *Minerals Engineering*, 116, 2018.

[41] Mengdi Zhang, Liping Qiu, and Guicai Liu. Basic characteristics and application of micro-nano bubbles in water treatment. volume 510, 2020.

[42] Carly Pellow, Carly Pellow, Carly Pellow, Meaghan A. O'Reilly, Meaghan A. O'Reilly, Kullervo Hynynen, Kullervo Hynynen, Gang Zheng, Gang Zheng, David E. Goertz, and David E. Goertz. Simultaneous intravital optical and acoustic monitoring of ultrasound-triggered nanobubble generation and extravasation. *Nano Letters*, 20, 2020.

[43] Vitaly B. Svetovoy, Remko G.P. Sanders, Theo S.J. Lammerink, and Miko C. Elwenspoek. Combustion of hydrogen-oxygen mixture in electrochemically generated nanobubbles. *Physical Review E - Statistical, Nonlinear, and Soft Matter Physics*, 84, 2011.

[44] Min Guan, Wen Guo, Lianhua Gao, Yuzhao Tang, Jun Hu, and Yaming Dong. Investigation on the temperature difference method for producing nanobubbles and their physical properties. *ChemPhysChem*, 13, 2012.

[45] Gianluca Ferraro, Ananda J. Jadhav, and Mostafa Barigou. A henry's law method for generating bulk nanobubbles. *Nanoscale*, 12, 2020.

[46] Michael John Klopfer. Micro and nanobubbles for wound healing applications, 2015.

[47] Nhi Vu Y. Quach, Ao Li, and James Calvin Earthman. Interaction of calcium carbonate with nanobubbles produced in an alternating magnetic field. *ACS Applied Materials and Interfaces*, 12, 2020.

[48] Hanping Wu, Nicolas G. Rognin, Tianyi M. Krupka, Luis Solorio, Hiroki Yoshiara, Gilles Guenette, Christopher Sanders, Naohisa Kamiyama, and Agata A. Exner. Acoustic characterization and pharmacokinetic analyses of new nanobubble ultrasound contrast agents. *Ultrasound in Medicine and Biology*, 39, 2013.

[49] Tinghui Yin, Ping Wang, Rongqin Zheng, Bowen Zheng, Du Cheng, Xinling Zhang, and Xintao Shuai. Nanobubbles for enhanced ultrasound imaging of tumors. *International Journal of Nanomedicine*, 7, 2012.

[50] Ye Wang, Xiang Li, Yan Zhou, Pengyu Huang, and Yuhong Xu. Preparation of nanobubbles for ultrasound imaging and intracelluar drug delivery. *International Journal of Pharmaceutics*, 384, 2010.

[51] Wen Lin, Xiangyang Xie, Jianping Deng, Hui Liu, Ying Chen, Xudong Fu, Hong Liu, and Yang Yang. Cell-penetrating peptide-doxorubicin conjugate loaded ngr-modified nanobubbles for ultrasound triggered drug delivery. *Journal of Drug Targeting*, 24, 2016.

[52] Xiangyang Xie, Yanfang Yang, Wen Lin, Hui Liu, Hong Liu, Yang Yang, Ying Chen, Xudong Fu, and Jianping Deng. Cell-penetrating peptide-sirna conjugate loaded ysa-modified nanobubbles for ultrasound triggered sirna delivery. *Colloids and Surfaces B: Biointerfaces*, 136, 2015.

[53] Hai Peng Tong, Luo Fu Wang, Yan Li Guo, Lang Li, Xiao Zhou Fan, Jun Ding, and Hai Yun Huang. Preparation of protamine cationic nanobubbles and experimental study of their physical properties and invivo contrast enhancement. *Ultrasound in Medicine and Biology*, 39, 2013.

[54] Hsin Yang Huang, Shang Hsiu Hu, Shih Ya Hung, Chih Sheng Chiang, Hao Li Liu, Tsung Lang Chiu, Hsin Yi Lai, You Yin Chen, and San Yuan Chen. Spio nanoparticle-stabilized paa-f127 thermosensitive nanobubbles with mr/us dual-modality imaging and hifu-triggered drug release for magnetically guided in vivo tumor therapy. *Journal of Controlled Release*, 172, 2013.

[55] Palwasha Khan, Wenjing Zhu, Feng Huang, Wanlin Gao, and Nasir Abbas Khan. Micro-nanobubble technology and water-related application. *Water Science and Technology: Water Supply*, 20, 2020.

[56] Kazuyuki Sakata. Water treatment method and water treatment system. *United States Patent*, 7,662,288, 2010.

[57] Ashutosh Agarwal, Wun Jern Ng, and Yu Liu. Principle and applications of microbubble and nanobubble technology for water treatment. *Chemosphere*, 84, 2011.

[58] Aliasghar Ghadimkhani, Wen Zhang, and Taha Marhaba. Ceramic membrane defouling (cleaning) by air nano bubbles. *Chemosphere*, 146, 2016.

[59] Hongbing Chen, Huiling Mao, Liping Wu, Jun Zhang, Yaming Dong, Zhihua Wu, and Jun Hu. Defouling and cleaning using nanobubbles on stainless steel. *Biofouling*, 25, 2009.

[60] Jie Zhu, Hongjie An, Muidh Alheshibri, Lvdan Liu, Paul M.J. Terpstra, Guangming Liu, and Vincent S.J. Craig. Cleaning with bulk nanobubbles. *Langmuir*, 32, 2016.

[61] J. Rubio, M. L. Souza, and R. W. Smith. Overview of flotation as a wastewater treatment technique. *Minerals Engineering*, 15, 2002.

[62] J. Haarhoff and J. K. Edzwald. Modelling of floc-bubble aggregate rise rates in dissolved air flotation. volume 43, 2001.

[63] M. Y. Han, M. K. Kim, and M. S. Shin. Generation of a positively charged bubble and its possible mechanism of formation. *Journal of Water Supply: Research and Technology - AQUA*, 55, 2006.

[64] Vassilios Yannopapas and Nikolay V. Vitanov. First-principles theory of van der waals forces between macroscopic bodies. *Physical Review Letters*, 99, 2007.

[65] N. Nirmalkar, A. W. Pacek, and M. Barigou. Interpreting the interfacial and colloidal stability of bulk nanobubbles. *Soft Matter*, 14, 2018.

[66] Jacob Israelachvili. *Intermolecular and Surface Forces*. 2011.

[67] Minmin Zhang and James R.T. Seddon. Nanobubble-nanoparticle interactions in bulk solutions. *Langmuir*, 32, 2016.

[68] Jeffrey D. Clogston and Anil K. Patri. *Characterization of Nanoparticles Intended for Drug Delivery: Zeta Potential Measurement*, volume 697. 2011.

[69] Vasco Filipe, Andrea Hawe, and Wim Jiskoot. Critical evaluation of nanoparticle tracking analysis (nta) by nanosight for the measurement of nanoparticles and protein aggregates. *Pharmaceutical Research*, 27, 2010.

[70] Jeffrey I. Steinfeld. Atmospheric chemistry and physics: From air pollution to climate change. *Environment: Science and Policy for Sustainable Development*, 40, 1998.

[71] Nikolai F. Bunkin, Alexey V. Shkirin, Nikolay V. Suyazov, Vladimir A. Babenko, Andrey A. Sychev, Nikita V. Penkov, Konstantin N. Belosludtsev, and Sergey V. Gudkov. Formation and dynamics of ion-stabilized gas nanobubble phase in the bulk of aqueous nacl solutions. *Journal of Physical Chemistry B*, 120, 2016.

[72] John Gregory. Interaction of unequal double layers at constant charge. *Journal of Colloid And Interface Science*, 51:44–51, 1975.

[73] World Health Organization. Cardiovascular diseases (cvds). retrieved april 14, 2022, from https://www.who.int/en/news-room/fact-sheets/detail/cardiovascular-diseases-(cvds), 6 2021.

[74] Grant Bailey, Judith Meadows, and Alan R. Morrison. Imaging atherosclerotic plaque calcification: Translating biology. *Current Atherosclerosis Reports*, 18, 2016.

[75] Sam Robbins. Scary facts about smoking and clogged arteries. retrieved march 16, 2022, from https://www.drsamrobbins.com/blood-flow/scary-facts-about-smoking-and-clogged-arteries, 5 2018.

[76] William Insull. The pathology of atherosclerosis: Plaque development and plaque responses to medical treatment. *American Journal of Medicine*, 122, 2009.

[77] Israel F. Charo and Rebecca Taub. Anti-inflammatory therapeutics for the treatment of atherosclerosis. *Nature Reviews Drug Discovery*, 10, 2011.

[78] S. C. Bergheanu, M. C. Bodde, and J. W. Jukema. Pathophysiology and treatment of atherosclerosis: Current view and future perspective on lipoprotein modification treatment. *Netherlands Heart Journal*, 25, 2017.

[79] Marta Brancati, Francesco Burzotta, Carlo Trani, Ornella Leonzi, Claudio Cuccia, and Filippo Crea. Coronary stents and vascular response to implantation: literature review. *Pragmatic and Observational Research*, Volume 8, 2017.

[80] Shefali Sood. Implanting trabecular meshwork bypass stents during cataract surgery cost effective in the usa. *PharmacoEconomics Outcomes News*, 888, 2021.

[81] Yan Li, Joseph Jing, Emon Heidari, Jiang Zhu, Yueqiao Qu, and Zhongping Chen. Intravascular optical coherence tomography for characterization of atherosclerosis with a 1.7 micron swept-source laser. *Scientific Reports*, 7, 2017.

[82] Yao yang Qiu, Jia hui Gui, Lin Huang, Xue qiang Hu, and Qin Li. Application of intravascular optical coherence tomography in detection of coronary atherosclerotic plaque. *Basic Clinical Medicine*, 42:360–365, 2022.

[83] Chenyang Xu, Joseph M. Schmitt, Stephane G. Carlier, and Renu Virmani. Characterization of atherosclerosis plaques by measuring both backscattering and attenuation coefficients in optical coherence tomography. *Journal of Biomedical Optics*, 13, 2008.

[84] Simon Yadgir, Catherine Owens Johnson, Victor Aboyans, Oladimeji M. Adebayo, Rufus Adesoji Adedoyin, Mohsen Afarideh, Fares Alahdab, Alaa Alashi, Vahid Alipour, Jalal Arabloo, Samad Azari, Celine M. Barthelemy, Catherine P. Benziger, Adam E. Berman, Ali Bijani, Juan J. Carrero, Félix Carvalho, Ahmad Daryani, Andre R. Durães, Alireza Esteghamati, Talha A. Farid, Farshad Farzadfar, Eduarda Fernandes, Irina Filip, Mohamed M. Gad, Samer Hamidi, Simon I. Hay, Olayinka Stephen Ilesanmi, Seyed Sina Naghibi Irvani, Mikk Jürisson, Amir Kasaeian, Andre Pascal Kengne, Abdur Rahman Khan, Adnan Kisa, Sezer Kisa, Dhaval Kolte, Navid Manafi, Amir Manafi, George A. Mensah, Erkin M. Mirrakhimov, Yousef Mohammad, Ali H. Mokdad, Ruxandra Irina Negoi, Huong Lan Thi Nguyen, Trang Huyen Nguyen, Molly R. Nixon, Catherine M. Otto, Shanti Patel, Thomas Pilgrim, Amir Radfar, David Laith Rawaf, Salman Rawaf, Wasiq Faraz Rawasia, Aziz Rezapour, Leonardo Roever, Anas M. Saad, Seyedmohammad Saadatagah, Subramanian Senthilkumaran, Karen Sliwa, Berhe Etsay Tesfay, Bach Xuan Tran, Irfan Ullah, Muthiah Vaduganathan, Tommi Juhani Vasankari, Charles D.A. Wolfe, Naohiro Yonemoto, and Gregory A. Roth. Global, regional, and national burden of calcific aortic valve and degenerative mitral valve diseases, 1990-2017. *Circulation*, 2020.

[85] Xiaoyou Ying, Norman J. Barlow, and Maureen H. Feuston. Micro-computed tomography and volumetric imaging in developmental toxicology, 2017.

[86] M. Kampschulte, A. C. Langheinirch, J. Sender, H. D. Litzlbauer, U. Althöhn, J. D. Schwab, E. Alejandre-Lafont, G. Martels, and G. A. Krombach. Nano-computed tomography: Technique and applications. *RoFo Fortschritte auf dem Gebiet der Rontgenstrahlen und der Bildgebenden Verfahren*, 188, 2016.

[87] B. Derjaguin. A theory of interaction of particles in presence of electric double layers and the stability of lyophobe colloids and disperse systems. *Progress in Surface Science*, 43, 1993.

[88] B. Derjaguin and L. Landau. Theory of the stability of strongly charged lyophobic sols and of the adhesion of strongly charged particles in solutions of electrolytes. *Progress in Surface Science*, 43, 1993.

[89] E. J.W. Verwey and J. Th G. Overbeek. Theory of the stability of lyophobic colloids. *Journal of Colloid Science*, 10, 1955.

[90] Gregor Trefalt and Michal Borkovec. Overview of dlvo theory. *Laboratory of Colloid and Surface Chemistry, University of Geneva*, 2014.

[91] Jacob Israelachvili and Richard Pashley. The hydrophobic interaction is long range, decaying exponentially with distance. *Nature*, 300, 1982.

[92] Kungang Li, Xiaonan Zhao, Brian K. Hammer, Songyan Du, and Yongsheng Chen. Nanoparticles inhibit dna replication by binding to dna: Modeling and experimental validation. *ACS Nano*, 7, 2013.

[93] Ahmed El. Trends and challenges in cmos design for emerging 60 ghz wpan applications, 2011.

[94] Stephen H. Donaldson, Anja Røyne, Kai Kristiansen, Michael V. Rapp, Saurabh Das, Matthew A. Gebbie, Dong Woog Lee, Philipp Stock, Markus Valtiner, and Jacob Israelachvili. Developing a general interaction potential for hydrophobic and hydrophilic interactions. *Langmuir*, 31, 2015.

[95] Evgeniya Lock, Scott Walton, and Richard Fernsler. Preparation of ultra thin polystyrene, polypropylene and polyethylene films on si substrate using spin coating technology. *NAVAL RESEARCH LAB WASHINGTON DC PLASMA PHYSICS DIV*, 2008.

[96] Ya.I. Rabinovich and B.V. Derjaguin. Interaction of hydrophobized filaments in aqueous electrolyte solutions. *Colloids and Surfaces*, 30:243–251, 1 1988.

[97] Emily E. Meyer, Kenneth J. Rosenberg, and Jacob Israelachvili. Recent progress in understanding hydrophobic interactions. *Proceedings of the National Academy of Sciences of the United States of America*, 103, 2006.

[98] Jiří Škvarla. Does the hydrophobic attraction contribute to the interaction between colloidal silica spheres coagulated by an adsorbing cationic surfactant? *Colloids and Surfaces A: Physicochemical and Engineering Aspects*, 397:33–41, 3 2012.

[99] Songjiang Chen, Zhen Li, Ningning Zhang, Lijun Liu, Jinzhou Qu, Yuexian Yu, Jing Chang, Zhanglei Zhu, and Xiuxiang Tao. A novel method for evaluating the hydrophobic interaction between coal particles and air bubbles and its role in flotation. *Advanced Powder Technology*, 33:103484, 3 2022.

[100] William A. Ducker and Dean Mastropietro. Forces between extended hydrophobic solids: Is there a long-range hydrophobic force? *Current Opinion in Colloid and Interface Science*, 22, 2016.

[101] Hugo K. Christenson and Per M. Claesson. Direct measurements of the force between hydrophobic surfaces in water. *Advances in Colloid and Interface Science*, 91, 2001.

[102] G. W.C. Kaye and T. H. Laby. Tables of physical and chemical constants. *Zeitschrift fur Kristallographie - New Crystal Structures*, 212, 1997.

[103] Engineering ToolBox. Helium-thermophysical properties. retrieved march 16, 2022, from https://www.engineeringtoolbox.com/helium-d_1418.html, 2008.